# Viability of UAV-based Antenna Pattern Measurements

by

Scott Graham Hilton Kriel


*Thesis presented in fulfilment of the requirements for the degree Master of Engineering at Stellenbosch University*

*Supervisor: Prof. D.I.L de Villiers*

March 2020

# Acknowledgements

While I'd love nothing more than to take all the credit, in truth this work is only partially due to my efforts and there a number of individuals I would like to thank:

- The South African Radio Observatory (SARAO) for funding this research

- My supervisor, Prof. Dirk de Villiers, thank you for your guidance over the last two years. Your passion for this field is infectious and served to motivate me through the tougher times.

- To Anneke Bester for suffering through some painful chamber measurements with me.

- To Wessel and Gift in the lab for their craftsmanship and expertise.

- To my flat-mates who have put up with me through all this.

- To Mom, Dad, Josh and the rest of my family. Coming back home to you is what makes it all worth it.

- To Zeni - doing this without you by my side was the hardest part.

# Declaration

Plagiarism is the use of ideas, material and other intellectual property of another's work and to present is as my own.

I agree that plagiarism is a punishable offence because it constitutes theft.

I also understand that direct translations are plagiarism.

Accordingly all quotations and contributions from any source whatsoever (including the internet) have been cited fully. I understand that the reproduction of text without quotation marks (even when the source is cited) is plagiarism.

I, the undersigned, declare that the work contained in this assignment is my original work and that I have not previously (in its entirety or in part) submitted it for grading in this module/assignment or another module/assignment.

Date: March 2020

# ABSTRACT

Unmanned aerial vehicle (UAV) based field measurements have been proposed as a possible solution to provide calibration data for large ground based radio telescope arrays, such as the Mid Frequency Aperture Array (MFAA) planned for the Square Kilometre Array (SKA) project. As such, we investigate the viability of performing antenna radiation pattern measurements in the frequency range 450–1450 MHz utilising a quad-copter equipped with a test source in the form of two orthogonal transmitting dipole antennas. The vehicle is fitted with the necessary flight controllers to enable autonomous navigation and uses a differential GPS (DGPS) module featuring real-time kinematics (RTK) to improve on the positional accuracy obtained from conventional GPS systems.

Given the proposed size of the MFAA, the far-field region of the array, or it's various sub-arrays, may exist at distances where measurement via UAVs becomes infeasible. Therefore, we go on to consider measurements performed in the near-field, from which a suitable near- to far-field transformation algorithm can be used in order to determine the far-field radiation pattern. The effect of random positional errors associated with DGPS on two different near- to far-field transformations, namely the planar plane wave expansion (PPWE) and the fast irregular antenna field transformation algorithm (FIAFTA), are investigated. The study shows that FIAFTA greatly outperforms the PPWE with regard to resilience to probe positioning errors. We find that the PPWE breaks down rapidly even for positional errors on the order of $\lambda/50$, whereas FIAFTA is seen to produce reasonable results up to error levels of $\lambda/20$. Considering a positional inaccuracy of 5 cm, typically associated with DGPS/RTK systems, we find that FIAFTA can produce satisfactory results across the whole frequency band of interest. However, in order to achieve these results, it was necessary to significantly increase the number of measurement samples from that necessitated by the minimum sampling requirements of the algorithm.

Additional practical issues are also considered, such as an investigation into how to distribute a reference signal through the system. This is necessary in order to measure the phase response of the system under test, which is required in near- to far-field transformation. Given the nature of UAV measurements, this reference signal must be provided in a detached fashion, which we accomplish by incorporating a second antenna into the measurement process. With the receiving characteristics of this reference antenna well-known, we are able to extract the phase of the measured response at the test antenna, allowing for its far-field pattern to be predicted. While this method works well in general, we find that one must be careful in setting up the measurement configuration, a sentiment which is reinforced by results obtained from a practical near-field measurement attempting to extract the phase as described.

# Contents

# List of Figures

# Chapter 1

# Introduction

## 1.1 Radio Astronomy and the SKA

[1] Ever since Karl Jansky first detected radio waves emanating from the Milky Way [2], the field of radio astronomy has been gaining steady interest, especially in the last few decades. Today, modern radio astronomy projects take the form of global initiatives, which design and make use of radio telescopes with ever-increasing sensitivity, budget and scale. This degree of commitment, seen in scientific and governmental institutions alike, is no more prevalent than in the Square Kilometre Array (SKA) project, which has attracted many international partners. With an unprecedented scale and a global backing, the SKA seeks to probe ground-breaking areas of science, such as galaxy formation, the evolution of black holes, and the search for extra-terrestrial life [3].

Upon completion, the proposed system will make observations of the universe at frequencies from 70 MHz up to 30 GHz, and consist of a collecting area of up to one million square metres [4]. Such an undertaking is no small feat and the project will consist of a number of phases, each being built on insights garnered from various pathfinder systems [5]. These precursor telescopes will test various proposed technologies and attempt to solve some of the unique design challenges posed by the SKA. Some pathfinders, such as MeerKAT in South Africa [6], ASKAP [7] and the Murchison Widefield Array (MWA) [8] in Australia, and LOFAR [9] in the Netherlands, are now functioning telescopes and are busy providing data which will prove valuable in advancing the project further. These systems target various frequency bands by utilising different technologies, each with their own set of characteristic traits. MeerKAT, operating in the frequency band 580 MHz–3.5 GHz, and ASKAP, operating between 700 MHz–1.8 GHz, make use of reflector antenna systems. In order to cover lower frequencies in the range 30–300 MHz, aperture arrays (AAs), such as LOFAR and the MWA, have been proposed as the technology of choice. These two differing technologies under investigation by the SKA are juxtaposed in Fig 1.1.1, with MeerKAT and the MWA representing examples of reflector and AA systems respectively. While the ubiquitous reflector antenna may be more familiar to the general public, initial radio telescopes were, in fact, AAs.

(a) MeerKAT [6]

(b) MWA [8]

Figure 1.1.1: Pathfinder telescopes

### 1.1.1 Aperture arrays and the MFAA

Due to advances in computing and signal processing, aperture arrays have seen a recent resurgence in the field and can offer significant advantages in field-of-view, scanning speed and possibly cost. Aperture arrays are able to synthesize large collecting areas by combining signals from a number of antenna elements placed in a specific configuration. By electronically introducing different delays into each of these signal paths, the radiation pattern of the array can be manipulated, allowing one to focus the pattern in different directions. This process, known as beam-forming, attempts to focus the radiation pattern into a main lobe, the direction of which can be varied (steered) across the observation domain [10]. As depicted in Figure 1.1.2, this ability to direct the radiation pattern by artificially introducing delays (or shifting the phases) of various incoming signals differentiates AAs from reflector systems, where the antenna is directed via mechanical means. How the elements of an array are placed in a relation to one another, i.e. their baselines, plays a pivotal role in the system's performance and is the topic of much discussion. Furthermore, elements can be grouped into different stations and sub-stations, with beam-forming taking place at various stages. With this technology it is possible to form multiple-beams, which can be electronically steered to scan the observation domain in an extremely rapid fashion. This, together with the durability allowed for by the lack of moving parts, have made AAs an attractive technology for radio telescopes deployed in all-weather conditions.

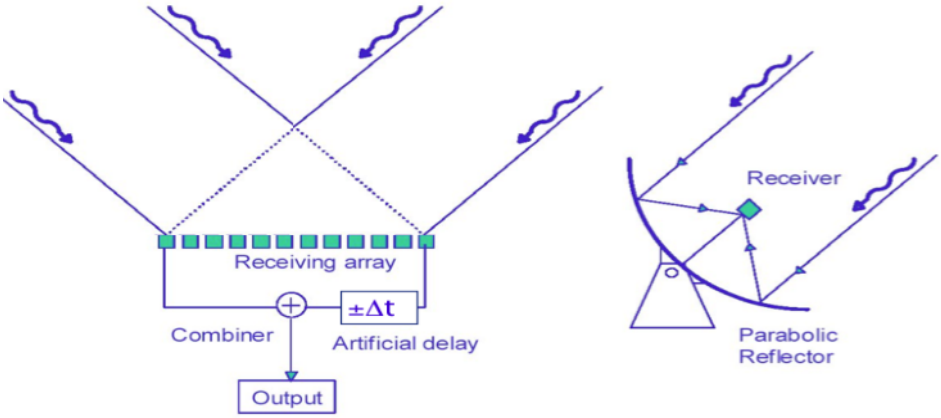


Figure 1.1.2: Schematic demonstrating the different steering mechanisms in AAs and reflectors [10]

The SKA plans to make full use of the benefits offered by AA technology with the low frequency aperture array (LFAA), which will function in the lowest planned frequency band from 50–350 MHz [11]. Due to the relatively long wavelengths at these frequencies, the components of a reflector antenna would have to be too large to make construction feasible. Instead, the LFAA will make use of log-periodic dipole array (LPDA) elements, an example of which can be seen in Figure 1.1.3a, named SKALA (the SKA LPDA) [12]. Building on the work of LOFAR and the MWA, an array of 256 of these antennas has been deployed in Western Australia as a prototype for the LFAA [13]. This demonstrator, shown in Figure 1.1.3b, serves to provide further insights into the practicality of a full scale system.

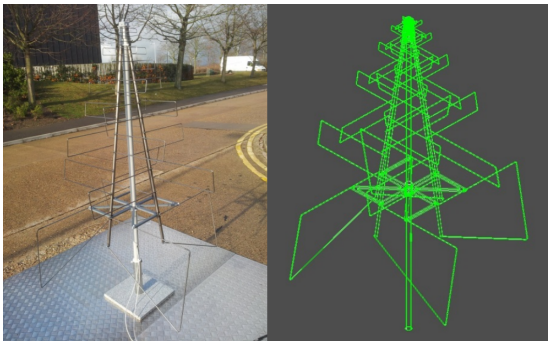

(a) SKALA antenna [12]

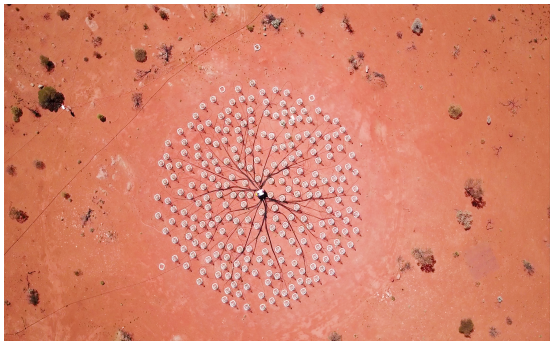

(b) Station of 256 SKALA antennas [13]

Figure 1.1.3: SKA low frequency prototype in Western Australia

The Mid-Frequency Aperture Array (MFAA), proposed for the next phase of the SKA, will extend the technologies of the LFAA to the frequency range 450–1450 MHz [14]. While most of this band is already covered by reflector arrays such as MeerKAT, the wide FoV and scanning speed make AAs particularly apt at studying transient events, such as fast radio bursts (FRBs) [15]. A number of front-end designs have been proposed for the

instrument, featuring different antenna elements and configurations. Candidates include a sparse array featuring an adaptation of the SKALA antenna in Figure 1.1.4a [16] and a dense array of Vivaldi antennas seen in the EMBRACE system, Figure 1.1.4b [17]. Other candidates include printed dipole or octagonal ring arrays, which provide a durable and scalable solution. Regardless of the chosen design, the essence of the instrument remains the same: implement large numbers of elements with a wide field of view (FoV) and use powerful computing and electronic beam-forming to achieve incredibly fast survey speeds. While this wide FoV is by design, it poses a significant challenge when it comes to calibration, which must be performed over the entire FoV simultaneously.

(a) 16 LPDA elements in Cambridge, UK [16]

(b) Vivaldi antennas in EMBRACE [17]

Figure 1.1.4: Candidates for the MFAA

### 1.1.2 Calibration and Verification

In order to make accurate observations of the universe, radio astronomers require that their antenna–receiver systems be well calibrated. Calibration, in general, refers to the process of reconciling the expected output of a system with that of the actual measured result for a given observation. In so doing, one is able to elucidate various environmental and instrumental factors affecting the system which, left unaccounted for, would corrupt the results of the experiment. When dealing with antenna arrays, calibration is performed in numerous ways and on various levels of the system. That being said, the general process remains the same: input a known signal into the component and use the measured result (instrumental response) to adjust the system parameters in order to obtain a true representation of the input signal [18]. Once the necessary adjustments are made, the system can proceed with the target measurement. By removing the effects of the instrument, one is able to compare the results of the experiment with others, performed on different instruments and at different times. The response of an entire array can be calibrated by observing a point source whose characteristics are very well defined. The choice of calibration source depends largely on what is being measured in the experiment and which factors are to be accounted for. Furthermore, the instrumental response is, in general, a function of the observation direction and a calibration source should reside in

close proximity to the target field. Alternatively, self-calibration (self-cal) techniques exist, whereby the actual target source is used to improve its own image. These techniques, which exploit redundancies in the measured data, now dominate the field over traditional calibration [19].

With the recent interest in aperture arrays, new demands are being placed on calibration routines. Algorithms must be adapted to account for the different phenomena affecting these instruments, such as that in [20], where the self-cal algorithm is extended to take into account directional dependent ionospheric effects. Given the sheer number of signal paths in the MFAA, existing calibration routines may become too computationally expensive to render them practical [21], and efforts must be made to optimise the process. Additionally, these routines depend on calibration sources in the observation domain with a high signal to noise ratio (SNR) and, as shown in [22], is not always possible when considering smaller subsystems or prototype arrays which one may wish to characterise. These systems do not always posses the necessary sensitivity or digital back-ends required to perform astronomical observations and one must seek other methods to verify the system.

## 1.2 Antenna Pattern Measurements

The radiation pattern of an antenna, which informs as to the ability to transmit or receive a signal in a given direction, is a major consideration in most antenna designs. While computational electromagnetic solvers can be used to predict this pattern to a reasonable accuracy, it is often necessary to validate a new design by performing a practical measurement on a prototype element. Considering the iterative design process of the SKA, whereby various pathfinders are deployed and analysed to improve subsequent designs, real-world measurements are of utmost importance in order to validate technologies.

### 1.2.1 Radiating Fields

Consider an antenna radiating in the spherical coordinate system, where a point anywhere in the field is described by the position vector $\mathbf{r} = r\hat{\boldsymbol{r}} + \theta\hat{\boldsymbol{\theta}} + \phi\hat{\boldsymbol{\phi}}$, with $\hat{\boldsymbol{r}}, \hat{\boldsymbol{\theta}}, \hat{\boldsymbol{\phi}}$ being the unit vectors in the radial, polar and azimuthal directions respectively. Very far away from the antenna, the field is seen to radiate in the $\hat{\boldsymbol{r}}$-direction from a point centred on the origin. Here, the electric and magnetic field components, $\mathbf{E}$ and $\mathbf{H}$, are perpendicular to the direction of propagation, forming a transverse electromagnetic (TEM) field mode [23]. Thus, we can relate $\mathbf{E}$ and $\mathbf{H}$ at any point $\mathbf{r}$ in this region by

$$\mathbf{H}(\mathbf{r}) = \frac{1}{\eta}\hat{\mathbf{r}} \times \mathbf{E}(\mathbf{r}), \tag{1.2.1}$$

where $\eta = 120\pi\ \Omega$ is the wave impedance of free space. Given that we can relate the **E**- and **H**-fields in this way, it is only necessary to consider one of these components when describing the radiation pattern of an antenna. For this, it is common to consider the **E**-field, where for any point **r** sufficiently far away from the antenna we can write

$$\mathbf{E}(\mathbf{r}) = \frac{1}{r}e^{-jkr}\left(E_\theta(\theta,\phi)\hat{\boldsymbol{\theta}} + E_\phi(\theta,\phi)\hat{\boldsymbol{\phi}}\right), \tag{1.2.2}$$

where $1/r$ and $e^{-jkr}$ denotes the divergence and phase factors respectively, with $k$ being the wave number and $r$ the distance from the origin to the field point $r = |\mathbf{r}|$. $E_\theta(\theta,\phi)$ and $E_\phi(\theta,\phi)$ represent the $\hat{\boldsymbol{\theta}}$ and $\hat{\boldsymbol{\phi}}$ components of the electric field respectively and it is convenient to group these terms in what can be referred to as the electric field radiation pattern function

$$\mathbf{F}(\theta,\phi) = E_\theta(\theta,\phi)\hat{\boldsymbol{\theta}} + E_\phi(\theta,\phi)\hat{\boldsymbol{\phi}}, \tag{1.2.3}$$

which gives the angular distribution of the electric field. Note that (1.2.3) is a function of direction alone and is not dependent on the distance $r$ from the antenna. This is a direct stipulation in the definition of the far-field region, also known as the Fraunhofer region, which is "that region of the field of an antenna where the angular field distribution is essentially independent of the distance from a specified point in the antenna's region" [24]. While the distance at which the far-field approximation of (1.2.2) holds true is dependent on the specific structure of the antenna, it is commonly taken as the region

$$r \geq \frac{2D^2}{\lambda}, \tag{1.2.4}$$

where $\lambda$ is the wavelength at the frequency in question and $D$ is the maximum dimension of the antenna. This region is taken to contain only the radiating field components, as opposed to the region directly surrounding the antenna which is dominated by reactive, evanescent waves and is called the reactive near-field region. This region is commonly taken to exist for $r < 0.62\sqrt{D^3/\lambda}$. The the region between this reactive near-field and the far-field, that is for

$$0.62\sqrt{\frac{D^3}{\lambda}} \leq r < \frac{2D^2}{\lambda}, \tag{1.2.5}$$

is known as the radiating near-field or Fresnel region. While reactive field components still exist here, the region is dominated by the radiating field contributions [25]. Unlike in the far-field region, **E** and **H** are no longer related by (1.2.1) and the angular field distribution varies as a function of distance $r$ away from the antenna. This variation in $r$ is seen as the result of interactions between the field components, which constructively and destructively interfere as the waves propagate outward.

For our purposes, we are interested in the power of radiated field, the square amplitude of the electric field pattern $|F(\theta,\phi)|^2$. For an antenna under test (AUT), this can be

measured by placing a probe antenna in the far-field of the AUT and recording the received power for different $\theta$ and $\phi$ angles. Depending on the size of the AUT, this is performed either in an anechoic chamber or on an outdoor measurement range, where mechanical positioning systems are used to orientate the AUT and probe relative to one another. Alternatively, we may perform the measurement in the near-field region and use near- to far-field transformation techniques in order to determine the radiation pattern of the AUT. Delaying an in-depth discussion of such techniques until Section 2.3, for now we suffice it to say that in order to perform such transformation, we require both the amplitude and phase to be measured in the near-field. This added phase requirement serves to further complicate the measurement process compared to those performed in the far-field region. Firstly, given that phase is a relative quantity, one must distribute a reference signal for comparison against the measured response [25]. Given that the phase of a signal with frequency $f$ varies in time between 0° and 360° every $T = 1/f$ seconds, demands on the phase stability of such reference signals grows with increasing frequency. Likewise, the phase of an antenna also varies in space on the order of the wavelength of the field $\lambda = c/f$, where $c$ is the speed of light. Considering this, any error made in the location of a measurement point will be seen as a corresponding phase error in the measured response. This added phase noise is built into our near- to far-field transformation, affecting the accuracy of the predicted pattern. This makes near-field measurements more susceptible to probe positioning errors than those performed in the far-field. As such, much effort on accurate positioning and tracking systems in near-field measurement chambers, aiming to reduce the positional error down to the range $\lambda/30$–$\lambda/50$ [26].

### 1.2.2 UAV-based Pattern Measurements

While antenna patterns are routinely measured in practise, large-scale aperture arrays such as the LFAA and MFAA pose a number of challenges. While the radiation pattern of a unit element may be measured in an anechoic chamber, the nature of these instruments means we are also interested in the resulting total pattern when these elements function together in an array. Apart from the specific design of the unit elements, other factors, such as the spacing between each antenna, will affect the performance of the array as a whole. Thus, in order to validate prototype designs, we are interested in measuring the total pattern of various arrays and sub-arrays of these antennas. Due to the large size of aperture arrays, such as the LFAA and the MFAA, conventional field measurements in an anechoic chamber soon become impractical, even when considering a few elements. Furthermore, measurements conducted on a far-field test range would require reconfiguring the array under test and neglect various environmental factors affecting the array when placed on site. Due to these factors, efforts are being made into performing un-

manned aerial vehicle (UAV) based field measurements. The term UAV, or drone, refers to an aerial vehicle equipped with the necessary positioning systems and flight controllers in order to enable autonomous navigation. The most common, commercially available drones feature electrically powered rotary motors, often classified by the number of rotors present (quadcopter for four rotors, hexacopter for six, etc.). By equipping these platforms with RF wave synthesizers and transmitting antennas, one is able to construct a highly configurable test source which can be used to characterise various array systems.

Various efforts have been made to perform such measurements, predominantly at frequencies less than 450 MHz. The system described in [27], featuring a hexacopter equipped with a transmitting dipole antenna, has been used to measure the radiation patterns of various antennas between 70–450 MHz. This is achieved by transmitting a continuous signal from the dipole and flying the drone through a predetermined path in the far-field of the antenna under test (AUT), while recording the voltage seen at its ports. During the measurement, the attitude (bearing, roll and pitch) of the drone is recorded by internal instruments, whereas the relative position of the source to the AUT is measured by a motorised total station. This is an optical/electronic instrument able to track the position of a retro-reflector placed on the drone to centimetric accuracy. By syncing the voltage measured at the AUT with the recorded position of the drone via a GPS clock, one is able to reconstruct the far-field radiation pattern of the AUT. This system has been used to characterise low frequency aperture arrays, such as LOFAR and the Aperture Array Verification System 0 (AAVS0), an array of 16 SKALA antennas constructed in the UK. As documented in [28], the UAV test source allowed various parameters of the arrays to be investigated, such as the embedded element patterns, sensitivity and polarisation performance. All these measurements are performed in the far-field of the system under test. As a result, pattern measurements of LOFAR were restricted to that of the individual sub-arrays, as the far-field of the entire array is located at a distance infeasible to cover with the drone. Other attempts have been made in the near-field region of the AUT, with the far-field pattern being determined by a suitable transform. This is demonstrated in [29], where a source fixed to a telescopic mast is used to measure the near-field of AAVS0 at specific points. These measurements are then used to update an electromagnetic method of moments (MoM) model of the array, increasing the accuracy of the predicted far-field radiation pattern. Measuring in the near-field requires that the relative phase between the source and AUT be taken into account in addition to the magnitude. This poses a significant hurdle when trying to distribute a constant phase reference between the AUT and drone. Attempting to solve this issue, the UAV system proposed in [30] uses a fibre optic cable directly linked to the UAV in order to provide a stable reference signal. Furthermore, an additional cable is used to supply power to the UAV, allowing for indefinite flight times.

## 1.3 About the Dissertation

### 1.3.1 Objectives

With the preceding discussion giving a brief overview of radio telescope arrays and antenna field measurements, we can move on to define the objectives of this study. Concerning ourselves with specific applications to the MFAA, we analyse the viability of UAV-based antenna pattern measurements in the frequency range 450–1450 MHz. Considering the large scale of the MFAA, the far-field region given by (1.2.4), may be located at distances unachievable by the UAV. Thus, we focus instead on near-field measurements and investigate different transformation algorithms used to predict the far-field pattern from this data. Furthermore, while optical and laser tracking systems have a reported accuracy on the millimetre scale, these instruments are in general expensive, bulky and must function within line of sight of the UAV. Therefore, following on from the recommendations in [26], we will consider a UAV equipped with a global navigation satellite system (GNSS) using real time kinematics (RTK) and differential GPS to improve accuracy of conventional GPS. Deciding to focus the study as such presents a number of challenges, the investigation of which forms the core of this work.

Firstly, the decision to perform the measurement in the near-field poses the challenge of distributing a phase reference between the AUT and drone. While the system presented in [30] uses direct cable links, this adds concerns on the manoeuvrability of the UAV. Thus, we investigate alternate methods in which this phase reference can be provided in a detached fashion.

Secondly, although RTK/DGPS provides a robust and relatively cheap solution, the positional accuracy is of concern. While a centimetric accuracy, reported to be anywhere in the range 1–10 cm, is a vast improvement on conventional GPS, it is still comparable to the shortest wavelength in our frequency band of interest, i.e. $\lambda \approx 20$ cm. With the previously discussed sensitivity of near-field measurements to positional error, the viability of our system is brought into question. We thus perform an analysis of this positional error sensitivity and attempt to find the limits at which our system will work.

### 1.3.2 Layout

With these objectives in mind, we structure the dissertation as follows:

- Chapter 2 - The theory behind antennas and radiating fields is presented. We define a number of fundamental antenna properties and go on to present two different near- to far-field algorithms which can be used to predict the radiating pattern of an antenna from measured data in the near-field.

- Chapter 3 - Both the UAV measurement platform and the characteristics of the antenna we wish to test play a major role in determining the viability of such a task. As such, this chapter sets out to define and characterise both the MFAA prototype element considered for testing and the specifics of our UAV measurement platform.

- Chapter 4 - Now knowing the type of antenna we wish to test, and having an indication as to the level of positional error we can expect from the UAV system, we proceed to investigate the positional error sensitivity of each of the two near- to far-field transformations presented in Chapter 2.

- Chapter 5 - Here, we focus on methods to distribute a phase reference whilst having no direct connection to the probe. This is attempted by incorporating a second antenna into the measurement process to act as a reference.

- Chapter 6 - Finally, we conclude with various remarks on the findings of the study and viability of UAV-based field measurements for the MFAA.

# Chapter 2

# Antenna Measurement Theory

## 2.1 Properties of Antennas

### 2.1.1 Radiation Intensity, Directivity and Gain

When analysing the merits of an antenna, we are concerned with its ability to transform input power, in the form of guided electromagnetic waves, into free-space propagating waves in a given direction. The average power density, $\mathbf{W}_{\text{av}}$, of the radiated field can then be calculated as

$$\mathbf{W}_{\text{av}} = \frac{1}{2}\Re\{\mathbf{E} \times \mathbf{H}^*\}, \tag{2.1.1}$$

where $\Re\{\cdot\}$ denotes the real part and $^*$ the complex conjugate. The quantity $\mathbf{W}_{\text{av}}$ describes the average power flow through an elemental surface in the field region. Considering our previous discussion on reactive fields, it is interesting to note that the imaginary part of $(\mathbf{E} \times \mathbf{H}^*)$ is associated with the reactive power of the field and is assumed to be negligible in the far-field. This is due to the fact that, as can be seen from (1.2.1), the **E**- and **H**-fields of a plane wave are always in phase and $(\mathbf{E} \times \mathbf{H}^*)$ is purely real. Taking this into account and using (1.2.2), (1.2.3), (1.2.1) and (2.1.1), the average power density can be written in terms of the far-field function $\mathbf{F}(\theta, \phi)$ as

$$\mathbf{W}_{\text{av}} = \frac{1}{2\eta r^2} \left|\mathbf{F}(\theta, \phi)\right|^2 \hat{\mathbf{r}}. \tag{2.1.2}$$

It is then common to introduce the radiation intensity $U(\theta, \phi)$ which is the power radiated per unit solid angle, calculated by multiplying the average power density by the square of the distance [31], as

$$U(\theta, \phi) = r^2(\mathbf{W}_{\text{av}} \cdot \hat{\mathbf{r}}) = \frac{1}{2\eta} \left|\mathbf{F}(\theta, \phi)\right|^2. \tag{2.1.3}$$

The total radiated power ($P_{\text{rad}}$) can be calculated by integrating the radiation intensity over the entire spherical surface,

$$P_{\text{rad}} = \int_0^{2\pi} \int_0^{\pi} U \sin\theta \, d\theta \, d\phi \,, \tag{2.1.4}$$

where $\sin\theta \, d\theta \, d\phi$ is the elementary solid angle. For directive antennas with one main beam, it is common to define the half-power beam width (HPBW) as the angular separation

between two points with a power level equal to half of that of the maximum power seen in the main beam. Given that the radiation intensity $U$ plots the power of the field, the half-power level is simply $0.5U_{\max}$, with $U_{\max}$ being the maximum radiation intensity seen in the beam. The beam width is then found by choosing a plane containing $U_{\max}$ and identifying two points on either side of the maximum with a value $0.5U_{\max}$. The $HPBW$ may be defined for different planes and provides a useful metric to describe the shape of the radiated field.

It is common to proceed by defining the directivity $D$ of an antenna. This is done by expressing the radiation intensity relative to the radiation intensity of an isotropic source $U_0$, radiating the same total power $P_{\text{rad}}$, equally in all directions. By normalising the intensity in this way, we shift focus from the amount of power radiated to that of the actual shape of the pattern and how concentrated the field is in specific directions. Given that $U_0$ is constant over all directions, (2.1.4) can be used to calculate the radiated power from an isotropic source as $P_{\text{rad}} = 4\pi\, U_0$ and the directivity can be expressed as

$$D(\theta, \phi) = \frac{U(\theta, \phi)}{U_0} = \frac{4\pi\, U(\theta, \phi)}{P_{\text{rad}}}\,. \tag{2.1.5}$$

The quantities of directivity and radiation intensity consider only the power which is radiated, and do not speak as to the antennas ability to transform an input power, supplied by a signal generator, into a radiated field. Therefore, we define the gain of an antenna, which relates the power supplied to the antenna to that which is radiated. There are different variations in exactly how the gain is defined and we will adhere to the convention in [24], which differentiates between gain and realised gain according to where the input power is defined. Gain $G$ compares the total power accepted by the antenna $P_{\text{o}}$ to that of the total radiated power $P_{\text{rad}}$ and is related to the directivity by

$$G(\theta, \phi) = e_{\text{rad}} D(\theta, \phi)\,, \tag{2.1.6}$$

where $e_{\text{rad}}$ is the radiation efficiency defined as

$$e_{\text{rad}} = \frac{P_{\text{rad}}}{P_{\text{o}}}\,. \tag{2.1.7}$$

Realised gain, on the other hand, relates the radiated power to that supplied by the signal generator. Assuming the generator is impedance matched with the line, the power supplied by the generator $P_{\text{in}}$ can be related to that accepted by the antenna $P_{\text{o}}$ by taking into account any mismatch between the impedance of the feed line and that of the antenna. The realised gain can then be defined as

$$G_{\text{R}}(\theta, \phi) = \left(1 - |\Gamma|^2\right) G(\theta, \phi) = e_{\text{rad}} \left(1 - |\Gamma|^2\right) D(\theta, \phi)\,, \tag{2.1.8}$$

with $(1 - |\Gamma|^2)$ being the impedance mismatch factor, defined in terms of the reflection coefficient

$$\Gamma = \frac{Z_{\text{in}} - Z_0}{Z_{\text{in}} + Z_0}\,, \tag{2.1.9}$$

where $Z_{\text{in}}$ is the input impedance of the antenna and $Z_0$ the characteristic impedance of the transmission line. The reflection coefficient $\Gamma$, also referred to as the $S_{11}$-parameter, gives the ratio between reflected and incident waves at the antenna port and, as is done here, can be used to calculate the amount of power that is transmitted across a boundary.

### 2.1.2 Polarisation

The polarisation of a field vector, "specifies the shape, orientation, and sense of the ellipse that the extremity of the field vector describes as a function of time," [24], where it is usually the electric field considered when describing the polarisation of a wave. Given that the radiated field of an antenna is approximated by plane waves, the electric field may be decomposed into any two vector components, with directions orthogonal to each other and the direction of propagation. While the pattern function given by (1.2.3) decomposes the field into $\hat{\boldsymbol{\theta}}$- and $\hat{\boldsymbol{\phi}}$-directed polarisations, a different set of orthogonal basis may be more suited to a specific application. When considering polarisation as a figure of merit for an antenna, we are concerned with its ability to receive or transmit a signal with a chosen reference or co-polar ($\hat{\mathbf{co}}$) orientation. The cross-polar component direction ($\hat{\mathbf{xp}}$), orthogonal to $\hat{\mathbf{co}}$ and the direction of propagation, represents the unwanted signal polarisation orientation and attention is placed on minimising its contribution to the entire field. Emphasis placed on the polarisation purity of an antenna is necessitated by various applications, such as when simultaneously transmitting multiple signals with different polarisation directions or with polarimetry in radio astronomy, which investigates the polarisation make up of different emissions in the universe.

We follow the convention outlined by Ludwig in [32], where three different polarisations are defined considering a linearly polarised radiating element. Ludwig's first definition considers the rectangular coordinate system, where one unit vector is chosen as the reference polarisation ($\hat{\mathbf{co}} = \hat{\mathbf{y}}$) and another as the cross-polar direction ($\hat{\mathbf{xp}} = \hat{\mathbf{x}}$). The second definition extends this to the spherical coordinate system, with polarisation directions chosen as unit vectors tangential to a spherical surface. Ludwig's third definition chooses polarisation directions to coincide with what is actually measured when performing a conventional spherical antenna measurement. The polarisation directions for this definition are given as

$$\hat{\mathbf{co}}(\theta, \phi) = \sin(\phi)\hat{\boldsymbol{\theta}} + \cos(\phi)\hat{\boldsymbol{\phi}}\,, \tag{2.1.10}$$

$$\hat{\mathbf{xp}}(\theta, \phi) = \cos(\phi)\hat{\boldsymbol{\theta}} - \sin(\phi)\hat{\boldsymbol{\phi}}\,. \tag{2.1.11}$$

These definitions are made considering a $\hat{\mathbf{y}}$-polarised source. If an $\hat{\mathbf{x}}$-polarised source is

to be considered instead, the corresponding expressions for definitions 1 and 3 are found by simply interchanging $\hat{\mathbf{co}}$ and $\hat{\mathbf{xp}}$.

The radiated field of an antenna can now be analysed according to the chosen polarisation definition. This is accomplished through decomposing the far-field function $\mathbf{F}$ into its co- and cross-polar components $F_{\text{co}}$ and $F_{\text{xp}}$, given by

$$F_{\text{co}} = \mathbf{F}(\theta, \phi) \cdot \hat{\mathbf{co}}^*(\theta, \phi)\,, \tag{2.1.12}$$

$$F_{\text{xp}} = \mathbf{F}(\theta, \phi) \cdot \hat{\mathbf{xp}}^*(\theta, \phi)\,. \tag{2.1.13}$$

From here, one can go on to analyse the different components of the various quantities defined previously, such as the partial directivities $D_{\text{co}}$ and $D_{\text{xp}}$.

## 2.2 Far-field Antenna Measurements

The radiation pattern of an antenna can be determined by using a second probe antenna to perform measurements directly in the far-field region. For reciprocal antennas the measurement may either be performed with the antenna under test (AUT) transmitting a signal and the probe receiving, or vice versa. By exciting the port of one antenna with a test signal and measuring the voltage seen at the other for different measurement positions, one is able to determine the radiation pattern of the AUT. The ratio between the power measured at the receiving antenna ($P_r$) to that of the power provided to transmitting antenna ($P_t$) is given by the well known Friis transmission formula [33], which is modified to include polarisation mismatch between the antennas and is given in terms of the antenna gains as

$$\frac{P_r}{P_t} = \left(1 - |\Gamma_t|^2\right)\left(1 - |\Gamma_r|^2\right)\frac{\lambda^2 G_t(\theta_t, \phi_t) G_r(\theta_r, \phi_r)}{(4\pi R)^2} \cdot \rho_f\,, \tag{2.2.1}$$

where $R$ is the distance between the two antennas. $G_t(\theta_t, \phi_t)$ and $G_r(\theta_r, \phi_r)$ are the gains of the transmit and receive antennas in the directions that the antennas "see" each other for a specific measurement point. The polarisation loss factor $\rho_f$ accounts for any power lost due to polarisation mismatch between the antennas. This can be calculated using

$$\rho_f = |\hat{\boldsymbol{\rho}}_t(\theta_t, \phi_t) \cdot \hat{\boldsymbol{\rho}}_r^*(\theta_r, \phi_r)|^2\,, \tag{2.2.2}$$

with $\hat{\boldsymbol{\rho}}_t$ and $\hat{\boldsymbol{\rho}}_t$ being the unit polarisation vectors of the transmit and receive antennas respectively, i.e. the unit vectors of the $\mathbf{E}$-field in the directions specified by $(\theta_t, \phi_t)$ for the transmitted field and $(\theta_r, \phi_r)$ for the receive field. Determining both the co- and cross-polar radiation patterns of an AUT requires resolving the components of its polarisation vector. As, in general, the polarisation vector contains more than one component, it is

necessary to perform multiple measurements with different probe/AUT orientations in order to resolve the number of unknowns. This is generally done by first aligning the probe to receive power from mostly the $\hat{\mathbf{co}}$-direction of the AUT and varying the probe through the measurement surface. Then the probe is aligned with the $\hat{\mathbf{xp}}$-direction of the AUT and the measurement performed again. With these two sets of results, it is possible to extract the complete radiation pattern of the AUT using (2.2.1).

If the AUT is relatively small, the far-field distance may be such to allow for the measurement to be performed in an anechoic chamber. However, this is not the case even for moderately sized antennas and so the measurement must be performed on a far-field test range. These ranges are usually outdoors, which presents an uncontrolled environment affected by the weather, radio frequency interference (RFI) and non-ideal ground plane. Given this, together with the fact that even these ranges may not be long enough when considering large arrays, extensive research has been done on performing the measurements in the near-field and subsequently predicting the far-field radiation pattern using a suitable near- to far-field transformation.

## 2.3 Near-field Antenna Measurements

The theory and practice of near-field antenna measurements has seen steady advancement over the years, a detailed overview of which is given in [34]. Early experimental work focussed on measuring and plotting the amplitude and phase of various radiating structures in the near-field, which then progressed to attempting to predict the far-field pattern of these structures while assuming the direct field components were being measured by the probe, i.e. assuming an ideal probe. In order to increase the accuracy of these measurements, various probe correction algorithms were introduced to take into account the effects of arbitrary measurement probes. One such algorithm is presented by Kerns in [35], where the known characteristics of an arbitrary measurement probe are used to correct the near-field measurement. This is achieved through the use of plane wave scattering matrix theory, rigorously detailed by Kerns in [36], which decomposes the field into sets of plane waves that can be superimposed to calculate the total power measured at the probe. The theory requires that the near-field be measured on a regularly spaced plane in front of the AUT, with the measured vector field components being tangential to the plane. This restricts analysis to the forward hemisphere of the AUT and can limit the FoV over which the antenna pattern can be resolved. To remove these limitations, the near-field may be measured on different surfaces, such as a cylindrical or spherical surface, where instead of decomposing the field into plane waves, a set of orthogonal modes propagating in the geometry of choice is used. While being relatively complex mathematically, spherical near-field measurements allow for the determination of the pattern over all angles, while possessing relatively straightforward positioning mech-

anisms. A comprehensive treatment on the spherical near-field measurement theory can be found in [37].

To extend the theory to include arbitrary scanning geometries, the electric- and magnetic- field integral equations (EFIE and MFIE), which relate current densities to their resulting radiated fields, are considered. These equations can be cast into a method of moments (MoM) formulation [38], where the measured coupling between the probe and AUT is used to resolve the current density on a surface representing the AUT. This may be a fictitious surface encompassing the AUT, as considered in [39], or may be chosen to coincide with the actual structure of the antenna, as in [40]. By resolving the currents in such a way, one is able to garner further insights into the radiation mechanisms of an antenna, providing a useful tool for design and optimisation. In addition to this, these formulations allow for the natural inclusion of any a priori information available on the AUT, which can be used to improve measurement results.

Given the type of UAV measurements being considered in this study, arbitrary scanning geometries allowed for by MoM formulations are seen as a huge advantage. In particular, the fast irregular antenna field transformation algorithm (FIAFTA), presented in [41], is to be considered. The performance of this algorithm will be compared to that of the more traditional planar plane wave expansion (PPWE), chosen for its mathematical simplicity and due to the fact that other scan geometries, such as cylindrical or spherical, would not be practically realisable with the UAV system considered.

### 2.3.1 Planar Plane Wave Expansion

#### Plane Wave Spectrum of Electromagnetic Fields

Following a procedure similar that in [42], we ignore probe effects at first and start by considering the fundamental problem of transforming measured near-field data of an AUT into its radiating far-field characteristics. Namely, we are concerned with calculating the value of the **E**-field as it radiates out into free-space, as described by the vector Helmholtz equation

$$\nabla^2\mathbf{E} + k^2\mathbf{E} = 0\,, \tag{2.3.1}$$

where for non-conductive media

$$k^2 = \omega^2\mu\epsilon\,, \tag{2.3.2}$$

with $\mu$ and $\epsilon$ respectively being the permeability and permittivity of the space, and $\omega$ the angular frequency of the wave. An elementary solution to (2.3.1) is obtained by considering a single plane wave, propagating in the rectangular coordinate system, where a point in the field is given by the positional vector $\mathbf{r} = x\hat{\mathbf{x}} + y\hat{\mathbf{y}} + z\hat{\mathbf{z}}$. This can be written as

$$\mathbf{E} = \mathbf{S}(\mathbf{k})e^{-j\mathbf{k}\cdot\mathbf{r}}\,, \tag{2.3.3}$$

where $\mathbf{S}(\mathbf{k})$ is the vector amplitude of the plane wave, propagating in the direction given by the vector wave number

$$\mathbf{k} = k_x\hat{\mathbf{x}} + k_y\hat{\mathbf{y}} + k_z\hat{\mathbf{z}}\,, \tag{2.3.4}$$

with a magnitude $k = |\mathbf{k}| = \sqrt{k_x^2 + k_y^2 + k_z^2}$. Given that the field is linear, a general solution to (2.3.1) can be given in terms of the superposition of plane waves over all $\mathbf{k}$ directions

$$\mathbf{E}(\mathbf{r}) = \frac{1}{8\pi^3}\iiint_{-\infty}^{\infty} \mathbf{S}(\mathbf{k})e^{-j(k_x x + k_y y + k_z z)}\,dk_x\,dk_y\,dk_z\,, \tag{2.3.5}$$

where $\mathbf{S}(\mathbf{k})$ is now the entire plane wave spectrum (PWS) of the radiated $\mathbf{E}$-field. It is clear from (2.3.11) that $\mathbf{E}(\mathbf{r})$ and $\mathbf{S}(\mathbf{k})$ form Fourier transform pairs, that is

$$\mathbf{S}(\mathbf{k}) = \mathcal{F}\{\mathbf{E}(\mathbf{r})\} = \iiint_{-\infty}^{\infty} \mathbf{E}(\mathbf{r})e^{j(k_x x + k_y y + k_z z)}\,dx\,dy\,dz\,, \tag{2.3.6}$$

where $\mathcal{F}$ denotes the Fourier transform operator with inverse $\mathcal{F}^{-1}$ as given by (2.3.5) for $\mathbf{E}(\mathbf{r}) = \mathcal{F}^{-1}\{\mathbf{S}(\mathbf{k})\}$, which also contains the lumped normalisation factor $1/8\pi^3$. Simplifications to the relation given by (2.3.5) and (2.3.6) can be made by noting that from (2.3.2) we have

$$k^2 = k_x^2 + k_y^2 + k_z^2 = \omega^2\mu\epsilon\,, \tag{2.3.7}$$

which means that for a plane wave of a single frequency, two components of $\mathbf{k}$ are sufficient to uniquely identify the wave direction. Considering the two components $k_x$ and $k_y$, $k_z$ can be calculated from the above relations as

$$k_z = \begin{cases} \sqrt{k^2 - (k_x^2 + k_y^2)}\,, & \text{for } \; k^2 \geq k_x^2 + k_y^2 \\ -j\sqrt{(k_x^2 + k_y^2) - k^2}\,, & \text{for } \; k^2 < k_x^2 + k_y^2\,, \end{cases} \tag{2.3.8}$$

where the first relation for $k^2 \geq k_x^2 + k_y^2$ represents the radiating portion of the field, whilst for $k^2 < k_x^2 + k_y^2$ the field is evanescent and does not contribute to the far-field of the antenna. This can be seen by noting that the calculated $k_z$ for this region results in a negative real exponent in (2.3.3), thus describing an exponentially decaying wave where $\mathbf{E}$ approaches zero for large $z$ displacement. Furthermore, as the region we are considering is source-free, we have from Gauss' law $\nabla \cdot \mathbf{E} = 0$ and substitution of (2.3.3) in here gives

$$\nabla \cdot \mathbf{E} = k_x S_x(\mathbf{k}) + k_y S_y(\mathbf{k}) + k_z S_z(\mathbf{k}) = 0\,. \tag{2.3.9}$$

Thus, if we specify the $\hat{\mathbf{x}}$ and $\hat{\mathbf{y}}$ components of the wave, the $\hat{\mathbf{z}}$ component can be calculated using

$$S_z(\mathbf{k}) = -\frac{k_x S_x(\mathbf{k}) + k_y S_y(\mathbf{k})}{k_z}\,, \tag{2.3.10}$$

where $k_z$ is calculated from $k_x$ and $k_y$ as in (2.3.8). Given this dependence of the $\hat{\mathbf{z}}$-component, we can rewrite the triple integral of (2.3.5) in terms of the 2D equivalent

$$\mathbf{E}(\mathbf{r}) = \frac{1}{4\pi^2}\int_{-\infty}^{\infty}\int_{-\infty}^{\infty}\mathbf{S}(\mathbf{k})e^{-j(k_x x+k_y y+k_z z)}\,dk_x\,dk_y\,, \tag{2.3.11}$$

where $k_z$ is given in terms of $k_x$ and $k_y$ as in (2.3.8). It is clear from the above that, if we know the PWS of a field $\mathbf{S}(\mathbf{k})$, we can calculate the value of the $\mathbf{E}$-field at any point $r$. However, as can be seen from (2.3.6), calculating $\mathbf{S}(\mathbf{k})$ requires integrating over the entire $\mathbf{E}$-field. As this is the unknown quantity we set out to determine initially, clearly some modification is required for the PWS to be of any use. This is accomplished by imposing the boundary condition $z = 0$, and considering the $\mathbf{E}$-field over the entire $xy$-plane. From the uniqueness theorem [23], we know that the tangential components $E_x$ and $E_y$ across this surface completely describes the field in the region $z \geq 0$. Therefore, using (2.3.6), we calculate the PWS components $S_x$ and $S_y$ as

$$S_x(k_x, k_y, z = 0) = \int_{-\infty}^{\infty}\int_{-\infty}^{\infty}E_x(x, y, z = 0)e^{j(k_x x+k_y y)}\,dx\,dy\,, \tag{2.3.12}$$

$$S_y(k_x, k_y, z = 0) = \int_{-\infty}^{\infty}\int_{-\infty}^{\infty}E_y(x, y, z = 0)e^{j(k_x x+k_y y)}\,dx\,dy\,. \tag{2.3.13}$$

By subsequently calculating $S_z$ as per (2.3.10), the complete spectrum $\mathbf{S}(\mathbf{k})$ is determined and (2.3.11) can be used to calculate the electric field at any point in the region $z \geq 0$.

### Plane Wave Scattering Matrix

In conventional circuit analysis, scattering parameters ($S$-parameters) are used extensively to characterise multi-port microwave networks in terms of the power waves seen at each port [43]. By considering the incident ($a_i$) and emerging ($b_j$) waves at each port $i$ and $j$, one can derive the $S$-parameters $S_{ij}$ which describe the response seen at port $i$ due to a signal at port $j$. A two-port network described by these parameters is shown in Fig. 2.3.1, where the terminal surfaces at ports 0 and 1 are represented by the dashed lines $P_0$ and $P_1$ respectively. Using the scattering matrix $\mathbf{S}$, one can relate the set of emergent waves $\mathbf{b}$ to the incident waves $\mathbf{a}$ as

$$\begin{gathered}\mathbf{b} = \mathbf{S}\mathbf{a} \\ \begin{pmatrix} b_0 \\ b_1 \end{pmatrix} = \begin{pmatrix} S_{00} & S_{01} \\ S_{10} & S_{11} \end{pmatrix}\begin{pmatrix} a_0 \\ a_1 \end{pmatrix}\,,\end{gathered} \tag{2.3.14}$$

where the incident and emergent (or reflected) directions are defined relative to an observer "looking" into the terminal surfaces $P_0$ and $P_1$ from the left and right respectively.

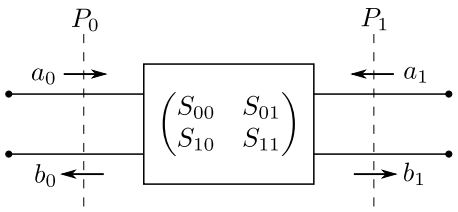


Figure 2.3.1: Two-port network described by $S$-parameters

These $S$-parameters can be defined in terms of the plane wave spectrum representation of electromagnetic fields, resulting in what is known as the plane wave scattering matrix (PWSM). The use of PWSM theory to describe antenna-antenna near-field interactions has been extensively developed by Kerns in [35], [36] and [44], where each antenna is described in terms of it's scattering matrix. This is achieved by viewing an antenna as a multi-port network, with one input and one output port for each polarisation and direction in the observation domain. With this description, a transmitting antenna can be seen as a transducer, which transforms guided waves supplied to the structure into a set of free space waves propagating in all directions. The reverse is true for a receiving antenna, whereby radiated waves impinging on the structure from all directions are transformed to guided waves which can be measured at the antenna terminal.

Consider the example illustrated in Fig. 2.3.2, depicting an AUT and probe antenna, aligned along the $\hat{\mathbf{z}}$-axis and separated by a distance $z_0$. For each antenna, we consider the incident and reflected waves over two terminal surfaces, taken to represent the port of the antenna and the boundary of free space. With the AUT in transmit mode, we wish to determine the response $b_0'$ seen at the probe when the AUT is supplied with the source wave $a_0$. These waves exist within the feed structure of each antenna, which we assume to support only a single mode of propagation. While these guided waves can be represented by scalar values, the free space waves $\mathbf{b}_1$ and $\mathbf{a}_2'$ are transmitted and received over all directions, and are thus vector quantities dependent on direction, i.e. $\mathbf{b}_1(k_x, k_y)$. To avoid cumbersome mathematics in the derivation to follow, the explicit denotation of this dependence on $\mathbf{k}$ is often omitted.

The corresponding network diagram of this scattering problem is shown in Fig. 2.3.3, where each antenna is described by it's scattering matrix and lumped between the terminal surfaces representing the port of the antenna and free space. Here, $S_{00}$ and $S_{00}'$ represent the reflection seen at the feeds of the AUT and probe respectively. This scalar quantity, known as the reflection coefficient, is commonly represented by the symbol $\Gamma$. While $\mathbf{S}_{11}$ and $\mathbf{S}_{22}'$ also represent reflection, these reflected waves are scattered over free space and are thus vector quantities. The receiving and transmitting characteristics of the AUT are given by $\mathbf{S}_{01}$ and $\mathbf{S}_{10}$ respectively, whereas $\mathbf{S}_{02}'$ and $\mathbf{S}_{02}'$ give the corresponding parameters for the probe. In the given configuration, the AUT acts as a source being supplied with the wave $a_0$, while the output of the probe is terminated with the load impedance $Z_L'$,

which has a reflection coefficient $\Gamma'_L$.

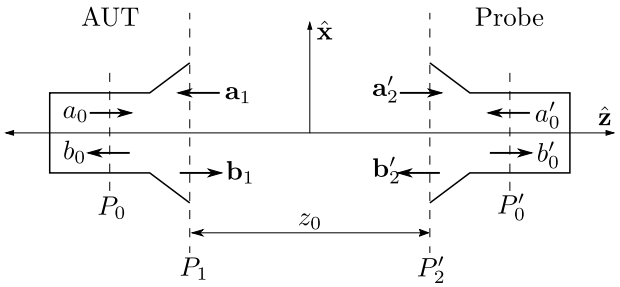


Figure 2.3.2: Schematic depicting scattering between AUT and probe

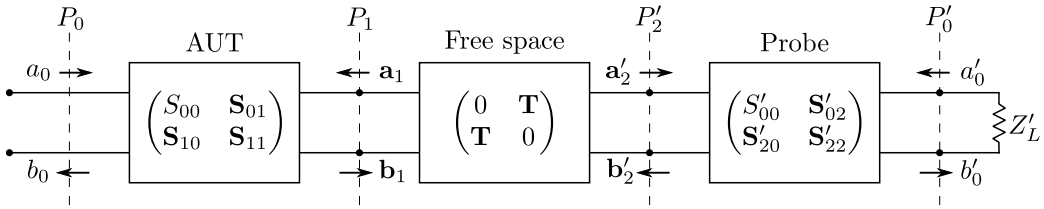


Figure 2.3.3: Network diagram of two antenna scattering problem

By incorporating the transmission over free space as yet another lumped element, we can form a complete network description of the antenna-antenna coupling problem. This transmission is accomplished through use of the translation matrix $\mathbf{T}$, which transforms plane waves emanating from the AUT into waves received by the probe. The same translation is used for waves coming from the probe to the AUT, and thus multiple reflections between these two antennas can be incorporated into the solution. Given that the waves are planar, translating them from one point to another is accomplished purely through a corresponding phase shift. Furthermore, considering that the antennas are aligned along the $\hat{\mathbf{z}}$-axis and separated by the distance $z_0$, $\mathbf{T}$ can be given by the diagonal matrix

$$\mathbf{T} = \begin{pmatrix} e^{jk_{z_1}z_0} & \dots & 0 \\ \vdots & \ddots & \vdots \\ 0 & \dots & e^{jk_{z_N}z_0} \end{pmatrix}, \tag{2.3.15}$$

where $N$ is the total number of discrete plane wave directions given by $k_x$ and $k_y$, which in turn are used to determine $k_z$ from (2.3.8).

Analysis of Fig 2.3.3 yields the network relations

$$\begin{pmatrix} b_0 \\ b_1 \end{pmatrix} = \begin{pmatrix} S_{00} & \mathbf{S}_{01} \\ \mathbf{S}_{10} & \mathbf{S}_{11} \end{pmatrix} \begin{pmatrix} a_0 \\ a_1 \end{pmatrix}, \quad \begin{pmatrix} b'_0 \\ b'_1 \end{pmatrix} = \begin{pmatrix} S'_{00} & \mathbf{S}'_{02} \\ \mathbf{S}'_{20} & \mathbf{S}'_{22} \end{pmatrix} \begin{pmatrix} a'_0 \\ a'_2 \end{pmatrix}, \tag{2.3.16}$$

and

$$\begin{pmatrix} a_1 \\ a_2' \end{pmatrix} = \begin{pmatrix} 0 & \mathbf{T} \\ \mathbf{T} & 0 \end{pmatrix} \begin{pmatrix} b_1 \\ b_2' \end{pmatrix}, \tag{2.3.17}$$

where we are interested in determining the output of the probe $b_0'$, given as $b_0' = S_{00}' a_0' + \mathbf{S}_{02}' \mathbf{a}_2'$. By making a number of simplifying assumptions, such as neglecting multiple reflections between the AUT and probe, we arrive at the result

$$b_0' = a_0 \left(1 - S_{00}' \Gamma_L'\right)^{-1} \mathbf{S}_{02}' \, \mathbf{T} \, \mathbf{S}_{10} \,, \tag{2.3.18}$$

which can be written in integral form as

$$b_0' = a_0 \left(1 - S_{00}' \Gamma_L'\right)^{-1} \iint_{-\infty}^{\infty} \mathbf{S}_{02}'(\mathbf{k}) \cdot \mathbf{S}_{10}(\mathbf{k}) e^{jk_z z_0} \, dk_x \, dk_y \,, \tag{2.3.19}$$

where it is clear that the observed response at the probe is the result of a superposition of plane wave over all directions $\hat{\mathbf{k}}$. If the antennas are not aligned along $\hat{\mathbf{z}}$ and the probe is displaced to a point defined by the coordinates $(x_p, y_p, z_0)$, the solution can be found by incorporating the necessary phase shifts in $\hat{\mathbf{x}}$ and $\hat{\mathbf{y}}$. Doing so allows us to express the coupling quotient between the two antennas, with the probe at any point $(x_p, y_p)$ in the $z = z_0$ plane, as

$$\frac{b_0'}{a_0} = \left(1 - \Gamma_0' \Gamma_L'\right)^{-1} \iint_{-\infty}^{\infty} e^{j(k_x x_p + k_y y_p)} \, \mathbf{S}_{02}'(\mathbf{k}) \cdot \mathbf{S}_{10}(\mathbf{k}) e^{jk_z z_0} \, dk_x \, dk_y \,, \tag{2.3.20}$$

where we have taken the source wave $a_0$ over to the left and interchanged the characteristic reflection coefficient of the probe $S_{00}'$ with the symbol $\Gamma_0'$. This coupling quotient describes the interactions between the two antennas in terms of the transmitting characteristics of the AUT $\mathbf{S}_{10}(\mathbf{k})$ and receiving characteristics of the probe $\mathbf{S}_{02}'(\mathbf{k})$. Alternatively, one may wish to define the problem with the probe transmitting and AUT receiving. Indeed, this would be the more natural configuration for radio telescope elements, where the normal mode of operation is receiving. For a reciprocal system, the plane wave transmitting characteristics $\mathbf{S}_{20}'(\mathbf{k})$ can be related to the receiving characteristics $\mathbf{S}_{02}'(\mathbf{k})$ using the reciprocity formula [44], which gives

$$\eta_0' \mathbf{S}_{02}'(\mathbf{k}) = \frac{k_z}{k Z_0} \, \mathbf{S}_{20}'(-\mathbf{k}) \,, \tag{2.3.21}$$

where $\eta_0'$ is the characteristic admittance seen in the antenna feed and $Z_0$ is the impedance of free space. The sign change of $\mathbf{k}$ is seen to reverse the direction of incoming waves to outgoing waves and vice versa. This reciprocity relation is useful considering the fact

that antennas are conventionally characterised by their transmitting characteristics, determined by a far-field pattern measurement. More specifically, the transmitting plane wave characteristics $\mathbf{S}_{10}$ and $\mathbf{S}'_{20}$ can be directly related to their respective far-field radiation patterns $\mathbf{F}(\theta, \phi)$, defined in the previous section. This is due to the fact that the far-field pattern already represents a set of plane waves, which propagate in the directions given by $\theta$ and $\phi$, related to $\mathbf{k}$ by

$$\begin{aligned} \mathbf{k} &= k\left(\sin\theta\cos\phi\hat{\mathbf{x}} + \sin\theta\sin\phi\hat{\mathbf{y}} + \cos\theta\hat{\mathbf{z}}\right) \\ &= k\left(\alpha\hat{\mathbf{x}} + \beta\hat{\mathbf{y}} + \gamma\hat{\mathbf{z}}\right) , \end{aligned} \tag{2.3.22}$$

where $\alpha, \beta$ and $\gamma$ are the directional cosines in the $\hat{\mathbf{x}}$, $\hat{\mathbf{y}}$ and $\hat{\mathbf{z}}$ directions respectively. With this, we can define the far-field pattern to be in terms of $\mathbf{k}$ as $\mathbf{F}(\mathbf{k})$, which relates directly to the transmitting plane wave characteristics, e.g. $\mathbf{S}_{10}(\mathbf{k})$ as [44]

$$\mathbf{S}_{10}(\mathbf{k}) = \frac{j}{k_z}\mathbf{F}(\mathbf{k})\,. \tag{2.3.23}$$

In order to deepen one's understanding of near- and far-field antenna interactions, it serves to take a moment here and compare the near-field coupling formula given by (2.3.20), to that of its far-field equivalent in (2.2.1). In the far-field, the received power is the result of the two gain patterns at the single transmitting and receiving direction, $(\theta_t, \phi_t)$ and $(\theta_r, \phi_r)$ respectively, where these directions are determined by the position and orientation of the probe's coordinate system, relative to that of the AUT's. On the other hand, near-field coupling for a single measurement point is given by integrating over all plane wave directions of the transmitting and receiving PWS. In other words, a single measurement point in the near-field does not measure the result of a single plane wave propagating from the AUT as it does in the far-field, but rather a combination of plane waves with different outgoing directions, weighted by the receiving characteristics of the probe at the corresponding incoming directions.

### Practical Measurement Formulation

We move on to consider practically evaluating the integrals describing near-field coupling. With the AUT placed at the origin, we measure the coupling seen at the probe as it moves through the plane at $z = z_0$, where the length of the scan plane in the $\hat{\mathbf{x}}$- and $\hat{\mathbf{y}}$-directions are denoted as $a$ and $b$ respectively. By only considering the field in this finite plane and assuming it is zero everywhere else, we are able to reduce the infinite integrals of the plane wave spectra to finite ones, with the boundaries $-a/2 \leq x \leq a/2$ and $-b/2 \leq y \leq b/2$.

Denoting the coupling ratio as the response $u(x, y, z = z_0)$, (2.3.20) can be rewritten as

$$u(x, y, z = z_0) = \frac{e^{jk_z z_0}}{(1 - \Gamma'_L \Gamma'_0)} \iint\limits_{k_x^2 + k_y^2 \leq k^2} \mathbf{S}'_{02}(\mathbf{k}) \cdot \mathbf{S}_{10}(\mathbf{k}) e^{-j(k_x x + k_y y)} \, dk_x \, dk_y \,, \tag{2.3.24}$$

where we evaluate the finite integral over the visible space, where $k_x^2 + k_y^2 \leq k^2$, exclusively. It is clear that the measured response is a Fourier transform of the factor $\mathbf{S}'_{02}(\mathbf{k}) \cdot \mathbf{S}_{10}(\mathbf{k})$. By taking the Fourier transform of the measured response as

$$U(k_x, k_y, z = z_0) = \mathcal{F}\{u(x, y, z = z_0)\} = \int_{-b/2}^{b/2} \int_{-a/2}^{a/2} u(x, y, z = z_0) e^{jk_x x} e^{jk_y y} \, dx \, dy \,, \tag{2.3.25}$$

we can write

$$U(k_x, k_y) = \frac{e^{jk_z z_0}}{(1 - \Gamma'_L \Gamma'_0)} \mathbf{S}'_{02}(\mathbf{k}) \cdot \mathbf{S}_{10}(\mathbf{k}) \,, \tag{2.3.26}$$

which we can write in terms of the transmitting characteristics of the probe using the reciprocity relation in (2.3.21)

$$U(k_x, k_y) = \frac{\gamma e^{jk_z z_0}}{\eta'_0 Z_0 \, (1 - \Gamma'_L \Gamma'_0)} \mathbf{S}'_{20}(-\mathbf{k}) \cdot \mathbf{S}_{10}(\mathbf{k}) \,. \tag{2.3.27}$$

With the unknown quantity $\mathbf{S}_{10}(\mathbf{k})$ shifted out of the integral and with known probe characteristics $\mathbf{S}'_{02}(\mathbf{k})$ it is then possible to set up a system of linear equations and solve for $\mathbf{S}_{10}(\mathbf{k})$. However, an important factor ignored up until now, is that, for a practical measurement, the receiving characteristics of a probe is usually given as its transmitting far-field pattern. While this can be converted to the receiving plane wave characteristics using (2.3.23) and (2.3.21), this does not take care of the fact that the far-field pattern, which is determined from a separate measurement of the probe, is given as referenced to the coordinate system of the probe and not the global system of the AUT during the measurement. Therefore, in order to evaluate the integrals in $\mathbf{k}$, it is necessary to relate the probe characteristics given for the directions $\mathbf{k}'$ to that of the global directions $\mathbf{k}$.

We will assume that the transmitting characteristics of the probe have been determined according to the reference system with unit vectors $\hat{\mathbf{x}}'$, $\hat{\mathbf{y}}'$ and $\hat{\mathbf{z}}'$. With the wave vector $\mathbf{k}'$ denoting the direction of propagation,

$$\mathbf{k}' = k_0 \left( \alpha' \hat{\mathbf{x}}' + \beta' \hat{\mathbf{y}}' + \gamma' \hat{\mathbf{z}}' \right) , \tag{2.3.28}$$

the transmitting characteristics of the probe can be written as

$$\mathbf{S}'_{20}(\mathbf{k}') = S'_{20x}(k'_x, k'_y) \hat{\mathbf{x}}' + S'_{20y}(k'_x, k'_y) \hat{\mathbf{y}}' + \frac{\alpha' S'_{20x}(k'_x, k'_y) + \beta' S'_{20y}(k'_x, k'_y)}{\gamma'} \hat{\mathbf{z}}' \,, \tag{2.3.29}$$

where we have used (2.3.10) in order to write the $\hat{\mathbf{z}}$ component in terms of the other two components. Before we can evaluate (2.3.27), it is necessary to transform (2.3.29) to be in terms of the reference coordinate system $\hat{\mathbf{x}}$, $\hat{\mathbf{y}}$ and $\hat{\mathbf{z}}$ with wave vector $\mathbf{k}$. Such a transformation can be accomplished using Eulerian angles, which specify the necessary rotations required to transform one coordinate system to another [45]. In literature, these three angles are commonly denoted by the symbols $\phi$, $\theta$ and $\psi$, however we will use the denotation $\xi$, $\chi$ and $\psi$ to avoid confusion with spherical angles. The definitions of these rotations varies according to reference coordinate systems and order of operation. In this work, we will follow the procedure depicted in Fig. 2.3.4, which defines three successive rotations required to transform the base orientation $\hat{\mathbf{x}}$-$\hat{\mathbf{y}}$-$\hat{\mathbf{z}}$ to the target orientation $\hat{\mathbf{x}}_w$-$\hat{\mathbf{y}}_w$-$\hat{\mathbf{z}}_w$. As each subsequent orientation is used to define the next rotation, the order of operations is important. Starting on the left with Fig. 2.3.4a, we rotate the base coordinate system by an angle $\xi$ about the $\hat{\mathbf{z}}$-axis, defining the new orientation $\hat{\mathbf{x}}_u$-$\hat{\mathbf{y}}_u$-$\hat{\mathbf{z}}_u$. Next, in Fig. 2.3.4b, we rotate this subsequent orientation about the new axis $\hat{\mathbf{y}}_u$ by an angle $\chi$. This gives us the new orientation $\hat{\mathbf{x}}_v$-$\hat{\mathbf{y}}_v$-$\hat{\mathbf{z}}_v$, which is rotated in Fig. 2.3.4c by $\psi$ about $\hat{\mathbf{z}}_v$, giving the final orientation $\hat{\mathbf{x}}_w$-$\hat{\mathbf{y}}_w$-$\hat{\mathbf{z}}_w$. With these Eulerian angles, we can

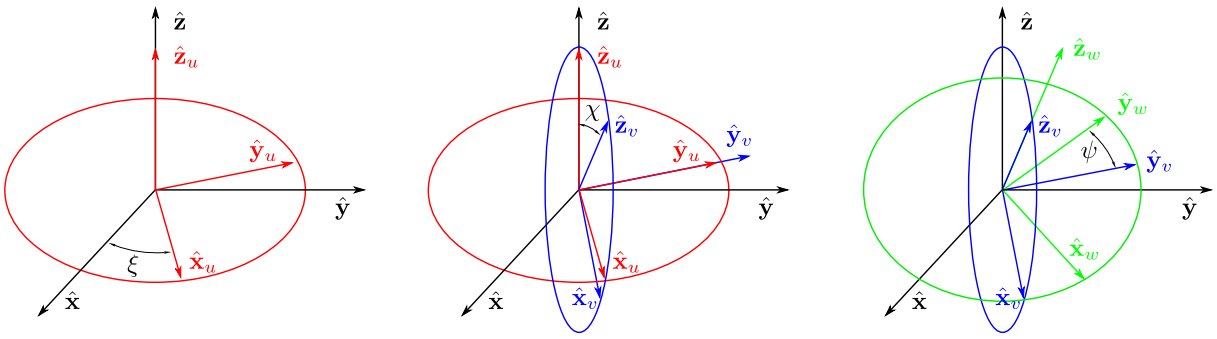


(a) Rotation about $\hat{\mathbf{z}}$ by $\xi$ (b) Rotation about $\hat{\mathbf{y}}_u$ by $\chi$ (c) Rotation about $\hat{\mathbf{z}}_v$ by $\psi$

Figure 2.3.4: Eulerian angle rotations

define the rotation matrix $\mathbf{R}$ as

$$\mathbf{R} = \begin{pmatrix} (\cos\xi\cos\chi\cos\psi - \sin\xi\sin\psi) & (\sin\xi\cos\chi\cos\psi + \cos\xi\cos\psi) & (-\sin\chi\cos\psi) \\ (-\cos\xi\cos\chi\sin\psi - \sin\xi\cos\psi) & (-\sin\xi\cos\chi\sin\psi + \cos\xi\sin\psi) & (\sin\chi\sin\psi) \\ (\cos\xi\sin\chi) & (\sin\xi\sin\chi) & (\cos\chi) \end{pmatrix}, \tag{2.3.30}$$

which can be used to express the rectangular components of a vector defined in one coordinate system, to that of another system with a different orientation.

To demonstrate the use of Eulerian angles in field measurements, we will consider the probe orientations depicted in Figure 2.3.5. With this relatively simple configuration, relations between the probe and AUT coordinate systems can be derived from simple

inspection, as is done in [46]. For probe B, we have the Eulerian angles $\xi = 0$, $\chi = \pi$ and

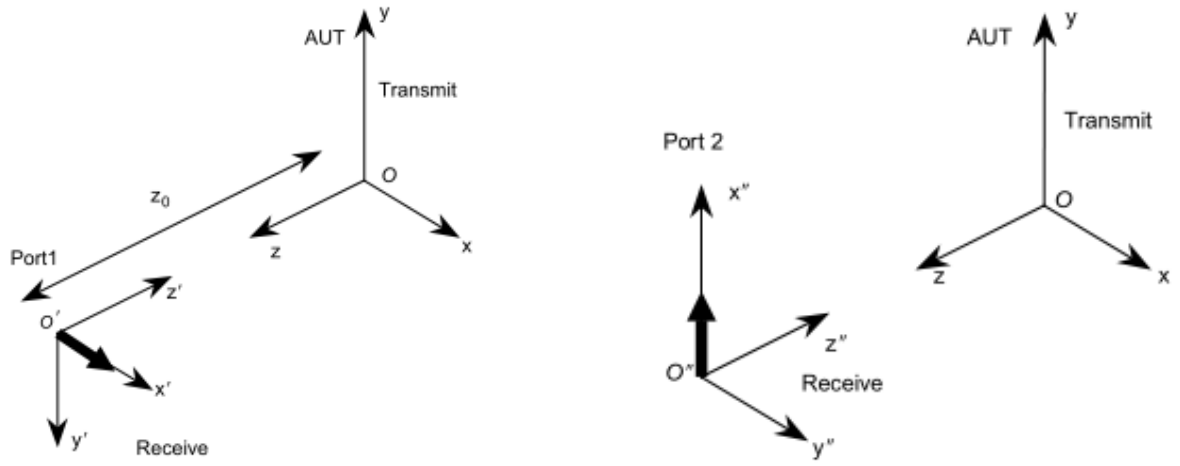


(a) Probe B for $\hat{\mathbf{x}}$-polarised measurement (b) Probe C for $\hat{\mathbf{y}}$-polarised measurement

Figure 2.3.5: Orientation of probe coordinate systems relative to AUT [46]

$\psi = \pi$. With this, the rotational matrix in (2.3.30) becomes

$$\mathbf{R}' = \begin{pmatrix} 1 & 0 & 0 \\ 0 & -1 & 0 \\ 0 & 0 & -1 \end{pmatrix}, \tag{2.3.31}$$

and the rectangular unit vectors can be related by

$$\begin{pmatrix} \hat{\mathbf{x}} \\ \hat{\mathbf{y}} \\ \hat{\mathbf{z}} \end{pmatrix} = \begin{pmatrix} 1 & 0 & 0 \\ 0 & -1 & 0 \\ 0 & 0 & -1 \end{pmatrix} \begin{pmatrix} \hat{\mathbf{x}}' \\ \hat{\mathbf{y}}' \\ \hat{\mathbf{z}}' \end{pmatrix} \tag{2.3.32}$$

which gives the relations $\hat{\mathbf{x}} = \hat{\mathbf{x}}'$, $\hat{\mathbf{y}} = -\hat{\mathbf{y}}'$ and $\hat{\mathbf{z}} = -\hat{\mathbf{z}}'$. Furthermore, with the outgoing direction being related to the incoming direction by opposite signs, we have

$$\begin{aligned} \mathbf{k}' = -\mathbf{k} &= -k_0 \left(\alpha\hat{\mathbf{x}} + \beta\hat{\mathbf{y}} + \gamma\hat{\mathbf{z}}\right) \\ &= -k_0 \left(\alpha\hat{\mathbf{x}}' + \beta(-\hat{\mathbf{y}}') + \gamma(-\hat{\mathbf{z}}')\right), \\ &= k_0 \left(-\alpha\hat{\mathbf{x}}' + \beta\hat{\mathbf{y}}' + \gamma\hat{\mathbf{z}}'\right) \end{aligned} \tag{2.3.33}$$

which, in turn, gives the relation between the directional cosines as

$$\alpha' = -\alpha\,, \quad \beta' = \beta\,, \quad \gamma' = \gamma\,. \tag{2.3.34}$$

Therefore we can write the probe transmitting characteristics in terms of the directional cosines of the AUT's coordinate system. This gives

$$\mathbf{S}'_{20}(-\mathbf{k}) = S'_{20x}(-\alpha,\beta)\hat{\mathbf{x}} - S'_{20y}(-\alpha,\beta)\hat{\mathbf{y}} - \frac{\alpha S'_{20x}(-\alpha,\beta) - \beta S'_{20y}(-\alpha,\beta)}{\gamma}\,\hat{\mathbf{z}}\,. \tag{2.3.35}$$

With the transmitting characteristics of the AUT given in a similar form as

$$\mathbf{S}_{10}(\mathbf{k}) = S_{10x}(\alpha,\beta)\hat{\mathbf{x}} + S_{10y}(\alpha,\beta)\hat{\mathbf{y}} - \frac{\alpha S_{10x}(\alpha,\beta) + \beta S_{10y}(\alpha,\beta)}{\gamma}\,\hat{\mathbf{z}}\,, \tag{2.3.36}$$

we can calculate the dot product of the two plane wave characteristics. Grouping together like terms and factoring out the $1/\gamma^2$ coefficient, we end up with

$$\begin{aligned}\mathbf{S}'_{20}(-\mathbf{k})\cdot\mathbf{S}_{10}(\mathbf{k}) =& \frac{1}{\gamma^2}\Big[\left(\gamma^2+\alpha^2\right)S'_{20x}(-\alpha,\beta)S_{10x}(\alpha,\beta) - \left(\gamma^2+\beta^2\right)S'_{20y}(-\alpha,\beta)S_{10y}(\alpha,\beta)\\ &- \alpha\beta S'_{20y}(-\alpha,\beta)S_{10x}(\alpha,\beta) + \alpha\beta S'_{20x}(-\alpha,\beta)S_{10y}(\alpha,\beta)\Big]\,,\end{aligned} \tag{2.3.37}$$

or, since $\alpha^2+\beta^2+\gamma^2 = 1$

$$\begin{aligned}\mathbf{S}'_{20}(-\mathbf{k})\cdot\mathbf{S}_{10}(\mathbf{k}) =& \frac{1}{\gamma^2}\Big[\left(1-\beta^2\right)S'_{20x}(-\alpha,\beta)S_{10x}(\alpha,\beta) - \left(1-\alpha^2\right)S'_{20y}(-\alpha,\beta)S_{10y}(\alpha,\beta)\\ &- \alpha\beta S'_{20y}(-\alpha,\beta)S_{10x}(\alpha,\beta) + \alpha\beta S'_{20x}(-\alpha,\beta)S_{10y}(\alpha,\beta)\Big]\,.\end{aligned} \tag{2.3.38}$$

Considering the above, we can write the response seen for the $\hat{\mathbf{x}}$-polarised measurement $U_x(k_x,k_y)$, as given by (2.3.27), in compact matrix notation

$$U_x(k_x,k_y) = \frac{e^{-jk_z z_0}}{\gamma}\begin{pmatrix}S'_{20x}(-\alpha,\beta) & S'_{20y}(-\alpha,\beta)\end{pmatrix}\cdot\begin{pmatrix}\left(1-\beta^2\right) & \alpha\beta\\ -\alpha\beta & -\left(1-\alpha^2\right)\end{pmatrix}\cdot\begin{pmatrix}S_{10x}(\alpha,\beta)\\ S_{10y}(\alpha,\beta)\end{pmatrix}. \tag{2.3.39}$$

In order to calculate the two unknowns $S_{10x}$ and $S_{10y}$, it is necessary to obtain two independent sets of measurements. This is accomplished performing a second measurement with probe C, shown in Figure 2.3.5b, which is simply probe B rotated by 90° about the $\hat{\mathbf{z}}$-axis to realise a $\hat{\mathbf{y}}$-polarised dipole. The Eulerian angles required to relate probe C's coordinates, $\hat{\mathbf{x}}''$, $\hat{\mathbf{y}}''$ and $\hat{\mathbf{z}}''$, to that of the global system are now given as $\xi = -\pi/2$, $\chi = \pi$ and $\psi = 0$. From (2.3.30) we can calculate the rotational matrix $\mathbf{R}''$ required to relate

probe C to the global coordinate system as

$$\begin{pmatrix} \hat{\mathbf{x}} \\ \hat{\mathbf{y}} \\ \hat{\mathbf{z}} \end{pmatrix} = \mathbf{R}'' \begin{pmatrix} \hat{\mathbf{x}}'' \\ \hat{\mathbf{y}}'' \\ \hat{\mathbf{z}}'' \end{pmatrix} = \begin{pmatrix} 0 & 1 & 0 \\ 1 & 0 & 0 \\ 0 & 0 & -1 \end{pmatrix} \begin{pmatrix} \hat{\mathbf{x}}'' \\ \hat{\mathbf{y}}'' \\ \hat{\mathbf{z}}'' \end{pmatrix}, \tag{2.3.40}$$

which gives $\hat{\mathbf{x}} = \hat{\mathbf{y}}''$, $\hat{\mathbf{y}} = \hat{\mathbf{x}}''$ and $\hat{\mathbf{z}} = -\hat{\mathbf{z}}''$. Relating $\hat{\mathbf{k}}''$ to $-\hat{\mathbf{k}}$, as performed for probe B in (2.3.33), we find that

$$\alpha'' = -\beta\,, \quad \beta'' = -\alpha\,, \quad \gamma'' = \gamma\,. \tag{2.3.41}$$

Following the analysis given by (2.3.35) – (2.3.39) for probe B, the system defining the response of the $\hat{\mathbf{y}}$-polarised measurement $U_y(k_x, k_y)$ can be determined. Combining this result with (2.3.39) the complete system of equations can be written in matrix form as

$$\begin{pmatrix} U_x(k_x,k_y) \\ U_y(k_x,k_y) \end{pmatrix} = \frac{e^{-jk_z z_0}}{\gamma} \begin{pmatrix} S'_{20x}(-\alpha,\beta) & S'_{20y}(-\alpha,\beta) \\ S'_{20y}(-\beta,-\alpha) & -S'_{20x}(-\beta,-\alpha) \end{pmatrix} \cdot \begin{pmatrix} \left(1-\beta^2\right) & \alpha\beta \\ -\alpha\beta & -\left(1-\alpha^2\right) \end{pmatrix} \cdot \begin{pmatrix} S_{10x}(\alpha,\beta) \\ S_{10y}(\alpha,\beta) \end{pmatrix} \tag{2.3.42}$$

Rewriting this in the compact form

$$\mathbf{U} = \frac{e^{-jk_z z_0}}{\gamma} [\mathbf{P}]\,[\mathbf{M}]\,[\mathbf{S}_{10}]\,, \tag{2.3.43}$$

where $\mathbf{P}$ contains the probe characteristics and $\mathbf{M}$ relates the orientation of the probe and AUT reference systems. The solution to the transmitting characteristics $\mathbf{S}_{10}$ of the AUT can be solved via

$$\mathbf{S}_{10} = \frac{e^{jk_z z_0}}{\gamma} [\mathbf{M}]^{-1}[\mathbf{P}]^{-1}[\mathbf{U}]\,, \tag{2.3.44}$$

with $[\cdot]^{-1}$ denoting the matrix inverse. This is easily related to the far-field of the AUT $\mathbf{F}(\mathbf{k})$ using (2.3.23), from which the $\mathbf{E}$-field at any point in the far-field is given by (1.2.2).

It is important to note that while the Eulerian rotation matrix given by (2.3.30) can be used to relate the global coordinate system to any chosen orientation of the probe, it is imperative that this orientation remain constant during the entire measurement. This is due to the fact that representing the coupling integral as simply the scalar product of the two plane wave characteristics of the antennas requires that the probe pattern remain constant over the measurement plane. This requirement of a constant probe pattern also prevents measuring within the reactive near-field of the AUT, where interactions between the probe and AUT will distort the probe pattern [46].

### Sampling Requirements

In order for the radiating field of the AUT to be reconstructed from near-field measurements, it necessary for the sample locations to fulfil certain requirements. The Fourier transform of the measured response, given in (2.3.25) for a scan plane with side lengths $a$ and $b$, is calculated for a discrete number of samples using the fast Fourier transform (FFT) algorithm. Following the FFT requirements of a constant sampling frequency, the near-field samples are acquired over a rectangular grid, with uniform spacing, $\Delta x$ and $\Delta y$, between points. Considering side lengths $a$ and $b$ in the $x$- and $y$-dimensions, the corresponding number of sample points, $M$ and $N$ are calculated as

$$M = \frac{a}{\Delta x} + 1\,, \tag{2.3.45}$$

$$N = \frac{b}{\Delta y} + 1\,. \tag{2.3.46}$$

From the Nyquist sampling theorem, we know that a band-limited function should be sampled at a frequency at least double to that of the maximum frequency seen in the function. Equating this to the spatial domain, the distance between points should be no greater than half a wavelength at the given frequency, thus making the choice

$$\Delta x = \Delta y = \frac{\lambda}{2}\,, \tag{2.3.47}$$

sufficient for full reconstruction of the field. The measurement coordinates can then be defined by $(m\Delta x, n\Delta y, z_0)$, where $m$ and $n$ are integers in the range $-M/2 \leq m \leq M/2-1$ and $-N/2 \leq n \leq N/2-1$ respectively. The wave numbers $k_x$ and $k_y$ are related to the measurement locations by

$$k_x = \frac{2\pi m}{M\Delta x}\,, \tag{2.3.48}$$

$$k_y = \frac{2\pi n}{N\Delta y}\,, \tag{2.3.49}$$

in turn determining the directions for which the transformed far-field is calculated. The angular region over which this transformation is valid is restricted by the size of the scan plane, where the maximum polar angle $\theta_{max}$ can be calculated as

$$\theta_{max} = \tan^{-1}\left(\frac{L-D}{2z_0}\right), \tag{2.3.50}$$

with $L$ being the length of the scan plane and $D$ the maximum dimension of the AUT. Given measurements over a single plane above the AUT, we are inherently restricted to resolving the far-field over the forward hemisphere, where $\theta_{max} < \pi/2$.

### 2.3.2 Fast Irregular Antenna Field Transformation Algorithm

The fast irregular antenna field transformation algorithm (FIAFTA), developed by Eibert et al. in [41], [47] and [48], presents an alternative to the classical near- to far-field transformations and provides a number of traits which can be seen as advantageous to the focus of this study. As the name suggests, FIAFTA is able to transform probe measurements, taken at a number of irregular points in the near-field of the AUT, into the radiating far-field. This is accomplished through the use of the diagonal translation operator $T_L$, well-known from the fast multipole method (FMM) [49] as

$$T_L(\mathbf{k}, \mathbf{r}_M) = -\frac{jk}{4\pi} \sum_{l=0}^{L} (-j)^l (2l+1) \mathrm{h}_l^{(2)}(kr_M) \mathrm{P}_l(\hat{\mathbf{k}} \cdot \hat{\mathbf{r}}_M) \,, \tag{2.3.51}$$

which is used to translate outgoing plane waves from the AUT into incoming plane waves at the probe for each measurement point $\mathbf{r}_M = r_M \hat{\mathbf{r}}_M$. The spherical Hankel function of the second kind $\mathrm{h}_l^{(2)}$ and Legendre polynomial $\mathrm{P}_l$ are both well known functions described in [50]. The multipole order $L$ is chosen according to the size of the AUT and probe, with the general rule being [48]

$$L = \frac{kd}{2} + 10 \,, \tag{2.3.52}$$

where $d$ is the sum of the diameters of the smallest spheres enclosing the probe and AUT, respectively. In contrast to the PPWE, where plane waves are seen to propagate from a rectangular aperture, here the radiating structure is represented by plane wave currents $\tilde{\mathbf{J}}(\mathbf{k})$ over the $\mathbf{k}$-space (or Ewald) sphere. These currents are seen as equivalent sources to the plane waves propagating in the direction defined by $\mathbf{k} = k\hat{\mathbf{k}} = k_\theta \hat{\boldsymbol{\theta}} + k_\phi \hat{\boldsymbol{\phi}}$. The output voltage $U$ seen at the probe for the measurement point $\mathbf{r}_M$ can then be calculated by integrating over the entire spherical surface

$$U(\mathbf{r}_M) = -j\frac{\omega\mu}{4\pi} \oiint T_L(\mathbf{k}, \mathbf{r}_M) \tilde{\mathbf{w}}^*(\hat{\mathbf{k}}) \cdot (\bar{\mathbf{I}} - \hat{\mathbf{k}}\hat{\mathbf{k}}) \cdot \tilde{\mathbf{J}}(\mathbf{k}) d\hat{\mathbf{k}}^2 \,, \tag{2.3.53}$$

with $\bar{\mathbf{I}}$ being the unit dyad and $\tilde{\mathbf{w}}(\mathbf{k})$ the spectral representation of the probe's transmission characteristics, where the conjugate denotes that it is now in receiving mode. The surface integral above may be evaluated via numerical quadrature, resulting in the discrete formulation

$$U^{1/2}(\phi_m, \theta_n, r_M) = -j\frac{\omega\mu}{4\pi} \sum_{k_\phi} \sum_{k_\theta} T_L(\hat{k}, \hat{r}_M) W(k_\theta) \, \mathbf{P}^{1/2}(k_\phi, k_\theta, \phi_m, \theta_n) \cdot (\bar{\mathbf{I}} - \hat{k}\hat{k}) \cdot \tilde{\mathbf{J}}(k_\phi, k_\theta) \,, \tag{2.3.54}$$

where the measured voltages $U^1$ and $U^2$ are the result of two sets of measurements performed with different probes, represented by their far-field receiving patterns $\mathbf{P}^1$ and $\mathbf{P}^2$ respectively. $W(k_\theta)$ is the weighting function from the chosen quadrature algorithm. Each

sample location is represented by $m = [1, 2, ..., M]$ and $n = [1, 2, ..., N]$, where $M$ and $N$ are the number of samples in the $\hat{\boldsymbol{\phi}}$ and $\hat{\boldsymbol{\theta}}$ directions respectively. Considering the above, it is possible to set up the system of linear equations

$$\mathbf{U}' = -j\frac{\omega\mu}{4\pi}||C|| \cdot \tilde{\mathbf{J}}' \,, \tag{2.3.55}$$

where

$$C^{1/2}_{\theta/\phi}(k_{\phi p}, k_{\theta q}, \phi_m, \theta_n) = T_L(\hat{k}, \hat{r}_M)W(k_{\theta_q})P^{1/2}_{\phi/\theta}(k_{\phi_p}, k_{\theta_q}, \phi_m, \theta_n) \,. \tag{2.3.56}$$

The discrete plane wave numbers $k_{\phi p}$ and $k_{\theta q}$, with $p = [1, 2, ..., P]$ and $q = [1, 2, ..., Q]$, are determined by the quadrature rule, where the number of samples ($P$ and $Q$ respectively) are a function of the multipole order $L$. It can be seen that the pattern of the probe has been split into its $\hat{\boldsymbol{\phi}}$- and $\hat{\boldsymbol{\theta}}$-polarised components, such that $||C||$ has the form

$$||C|| = \left(\begin{array}{ccc} C^1_\phi(k_{\phi 1}, k_{\theta 1}, \phi_1, \theta_1) & \dots & C^1_\theta(k_{\phi P}, k_{\theta Q}, \phi_1, \theta_1) \\ \vdots & \ddots & \vdots \\ C^1_\phi(k_{\phi 1}, k_{\theta 1}, \phi_M, \theta_N) & \dots & C^1_\theta(k_{\phi P}, k_{\theta Q}, \phi_M, \theta_N) \\ \hline C^2_\phi(k_{\phi 1}, k_{\theta 1}, \phi_1, \theta_1) & \dots & C^2_\theta(k_{\phi P}, k_{\theta Q}, \phi_1, \theta_1) \\ \vdots & \ddots & \vdots \\ C^2_\phi(k_{\phi 1}, k_{\theta 1}, \phi_M, \theta_N) & \dots & C^2_\theta(k_{\phi P}, k_{\theta Q}, \phi_M, \theta_N) \end{array}\right) , \tag{2.3.57}$$

and the corresponding forms of $\mathbf{U}'$ and $\tilde{\mathbf{J}}'$ are given as

$$\mathbf{U}' = \left(\begin{array}{c} U^1(\phi_1, \theta_1, r_M) \\ \vdots \\ U^1(\phi_M, \theta_N, r_M) \\ \hline U^2(\phi_1, \theta_1, r_M) \\ \vdots \\ U^2(\phi_M, \theta_N, r_M) \end{array}\right) , \tag{2.3.58}$$

$$\tilde{\mathbf{J}}' = \begin{pmatrix} \tilde{J}_\phi(k_{\phi 1}, k_{\theta 1}) \\ \tilde{J}_\theta(k_{\phi 1}, k_{\theta 1}) \\ \vdots \\ \tilde{J}_\phi(k_{\phi P}, k_{\theta Q}) \\ \tilde{J}_\theta(k_{\phi P}, k_{\theta Q}) \end{pmatrix} . \tag{2.3.59}$$

A suitable solver, such as the generalised minimal residual (GMRES) solver, can then be used to solve for the both components of the plane wave currents $\tilde{J}_\phi$ and $\tilde{J}_\theta$. With these known, the far-field of the AUT can be approximated as

$$\mathbf{E}^{FF}(r, \theta, \phi) = -j\frac{\omega\mu}{4\pi}\frac{e^{-jkr}}{r}\tilde{\mathbf{J}}(k_\theta, k_\phi)\,, \tag{2.3.60}$$

### Sampling Requirements

While the Nyquist sampling criterion of FFT based algorithms, such as the PPWE, require a fixed number of measurement samples for a given frequency, the number of samples required by FIAFTA depends on the size of the AUT relative to the wavelength of the frequency in question. This is due the fact that the number of samples must be equal to, or greater than, the number of unknown plane wave currents, determined by the multipole order $L$ which, as given by (2.3.52), is a function of frequency and AUT size. The specifics of choosing measurement locations for FIAFTA is discussed in [48], where the number of $\phi$- and $\theta$-directed unknown plane wave currents over the Ewald sphere of the AUT is respectively given as

$$P = 2\alpha_1 L\,, \quad Q = \alpha_2 L\,, \tag{2.3.61}$$

where $\alpha_1$ and $\alpha_2$ are said to range from one, to slightly greater than one depending on the level of noise present in the measurement. The number of required measurement samples in the $\phi$- and $\theta$-directions is then chosen according to

$$M = \chi_1 P = 2\chi_1\alpha_1 L\,, \tag{2.3.62}$$

$$N = \chi_2 Q = \chi_2\alpha_2 L + 1\,, \tag{2.3.63}$$

where $\chi_1$ and $\chi_2$ are factors relating the number of unknowns to the number of measurement samples. Choosing $\chi_1 = \chi_2 = 1$ fulfils the minimum requirements of the system, while greater values results in an overdetermined system where the number of samples is greater than the number of unknowns. This may, in turn, increase the accuracy of the algorithm and decrease sensitivity to noise. While FIAFTA is able to handle completely arbitrary measurement locations, the performance of the algorithm can be increased by

choosing the least redundant configuration. Given that we are attempting to resolve currents over the Ewald sphere, a natural choice is that of a spherical sampling geometry of constant radius, with a uniform step size in the $\phi$- and $\theta$-directions, given as

$$\Delta\phi = \frac{2\pi}{M}\,, \quad \Delta\theta = \frac{\pi}{(N-1)}\,. \tag{2.3.64}$$

Sample locations over an arbitrary surface can then be determined by projecting the points given over the sphere, defined by $\phi_m$ and $\theta_n$ onto the chosen measurement plane. For a planar surface situated at $z = z_0$, the rectangular measurement coordinates $(x_{mn}, y_{mn})$ can be calculated as

$$x_{mn} = z_0 \tan\theta_n \cos\phi_m\,, \tag{2.3.65}$$

$$y_{mn} = z_0 \tan\theta_n \sin\phi_m\,, \tag{2.3.66}$$

where the maximum polar angle $\theta$ is limited by the size of the scan plane, such as in (2.3.50), and is always less than 90°, given that only sample locations projected from the forward hemisphere will intersect with the plane at $z_0$. Choosing the configuration as such results in samples being more densely located around the poles of the AUT, with sample locations spreading out as we move away from zenith. Depending on the situation, one may wish to spread the sample locations more uniformly, such as with the planar spiral geometry presented in [51]. The optimal choice of measurement locations is dependent on the particular scenario, where a discussion on non-redundant representation of different sources is given in [52]. For moderately sized antennas, the number of samples required by FIAFTA is considerably less than required by the PPWE for a Nyquist sampling rate. However, given that FIAFTA is dependent on the size of the AUT and the PPWE is not, for large antenna structures FIAFTA may require more samples than the PPWE. Considering the large aperture size of the MFAA, this may make for a computationally intensive procedure. This may be alleviated by adopting a multilevel hierarchical grouping scheme, as used in the multilevel fast multipole method (MLFMM). By dividing the AUT into a number of source boxes and solving for the unknown plane wave currents of each, one can aggregate the individual contributions to calculate the total field, thus making for a more robust algorithm.

# Chapter 3

# System Description

## 3.1 Introduction

In Chapter 1, the technology of current radio telescopes is discussed and several goals of the SKA project are set forth. Additionally, Section 1.2.2 served to highlight various attempts at measuring the radiation pattern of antenna structures, utilising a UAV as either a test source or field probe. With the viability of such measurements being dependent on both the specifics of the antenna under test (AUT) and the UAV used to perform the measurement, it is necessary to define each by considering specific examples. To this end, we will introduce the SKA aperture prototype (SKAAP), a collaboration project between Stellenbosch and Cambridge Universities with the goal of deploying a 16 element array in Klerefontein, close to the SKA SA support building. The specifics of this system are taken into account when considering near-field measurements performed with the UAV documented in Section 3.3, named the flying electromagnetic unit (FEMU). With these two systems in mind, we seek to elucidate the various practical limitations that one will encounter when attempting to perform the antenna measurements outlined in Chapter 2. Much of this is built on the work of Dr. Hardie Pienaar [53] during his collaboration between Stellenbosch and Cambridge Universities.

## 3.2 SKA Aperture Prototype

The SKA aperture prototype (SKAAP) is a demonstrator array for the MFAA project, designed for deployment on site in Klerefontein, South Africa. The array features 16 dual-polarised LPDA antennas, designed by Cambridge University as a candidate for the MFAA. With the elements spaced in a sparse random configuration, the front end design of SKAAP closely resembles that of the prototype system described by [16] and shown in Fig 1.1.4a, which is deployed at Lord's Bridge in the UK. However, the antenna elements of SKAAP are of a subsequent design to this, documented below, which features some slight adaptions to the structure. The purpose of SKAAP is to demonstrate technology relevant to the MFAA and will be used to investigate various pertinent topics, such as the degradation of antenna elements in the Karoo environment, in addition to possibly serving as a test-bed for UAV-based field measurements.

### 3.2.1 MFAA Antenna Element

The antenna element we will consider during the course of this study is that presented in [1], featuring some slight adaptions which can be seen in the FEKO model shown in Fig. 3.2.1a. We simulate the $\hat{\mathbf{x}}$-polarised element, shown with maximum dimensions in Fig. 3.2.1b, with a finite ground plane measuring $305 \times 205$ mm. The results obtained from FEKO are compared with those measured on the actual prototype element, manufactured for the SKAAP system. First, we compare the magnitude of the reflection coefficient $|S_{11}|$ in Fig. 3.2.2a over the band 400–1500 MHz, where it can be seen that the measured reflection is better (lower) than that of the simulated value for most of the band. Next, we compare the bore-sight gain over the frequency band. To accomplish this in measurement, the three-antenna gain method is used, whereby the on-axis $S_{21}$ parameter between three different antennas is measured in the anechoic chamber. With the MFAA prototype as the AUT, the other two antennas used are a double ridged broadband horn (NSI-RF-RGP10) and a bi-conical antenna, manufactured by Nearfield Systems, Inc. (NSI) and Rohde&Shwarz respectively. The gain of the MFAA antenna is extracted and shown in Fig. 3.2.2b, where, due to limitations of the test antennas and chamber absorbers, we are restricted to frequencies above 750 MHz. The differences seen between measured and simulated results here may be due to a variety of reasons. While we make no attempt here to determine the exact source of these discrepancies, the results in Fig. 3.2.1 serve to illustrate the importance of performing practical measurements in order to validate simulated results.

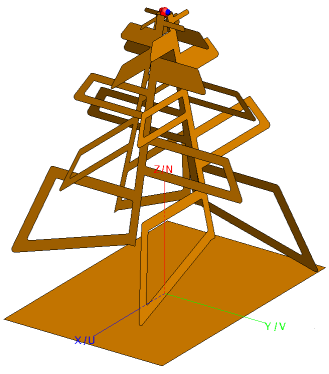

(a) FEKO model of LPDA element [53]

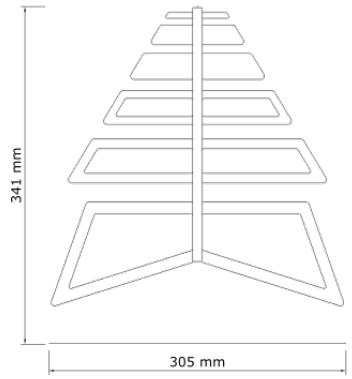


(b) Side view of single element showing maximum dimensions.

Figure 3.2.1: Mid-frequency LDPA designed for the MFAA

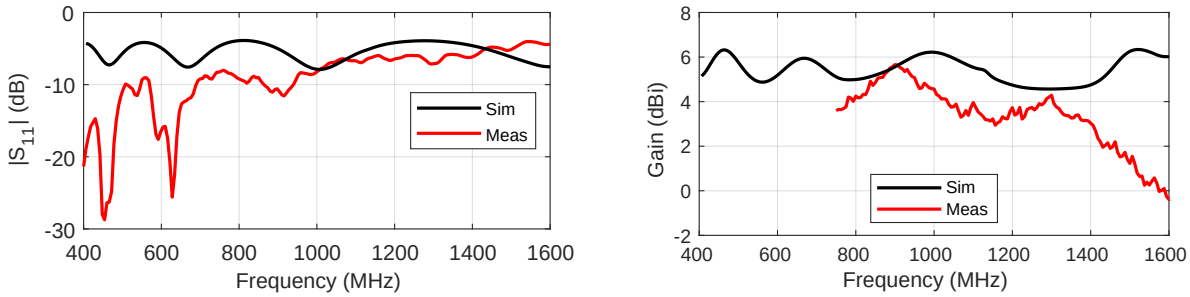


(a) Reflection coefficient (b) Gain

Figure 3.2.2: Comparing reflection coefficient and gain for measurement and simulation

We move on to perform a spherical near-field measurement of the MFAA prototype, using the horn antenna (RGP10) as a probe. As previously mentioned, we are restricted to above 750 MHz, and measure the co- and cross-polarised patterns from 750–1500 MHz, with a 50 MHz spacing between frequencies. The measurement system used in the anechoic chamber here at Stellenbosch University utilises equipment and software developed by NSI, which performs the acquisition of the near-field data, as well as transforming to the far-field via a spherical wave expansion (SWE). The software produces the resulting far-field patterns at each measurement frequency, where Fig. 3.2.3a and Fig. 3.2.3b respectively show the Ludwig 3 co- and cross-polarisation patterns at 1 GHz. These 3D figure are shown in decibels (dB) and normalised to the maximum of each. Also at

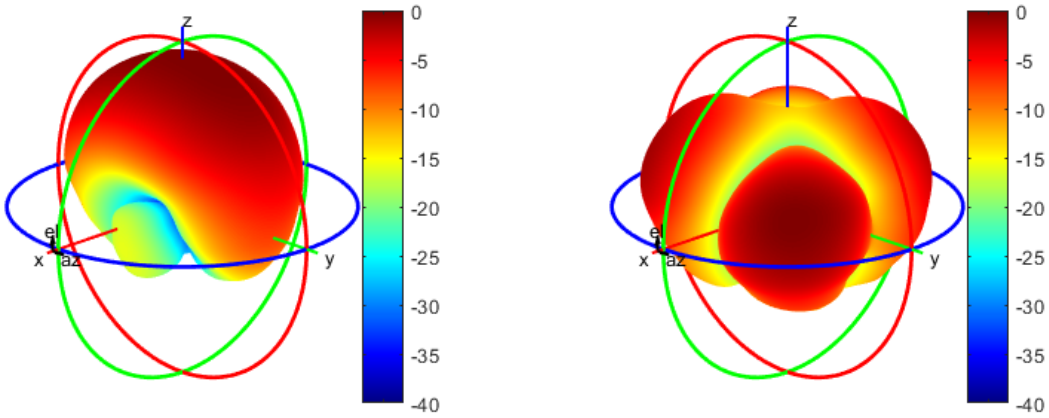


(a) Co-polarised (b) Cross-polarised

Figure 3.2.3: 3D patterns far-field for MFAA antenna, computed from spherical near-field measurement in the anechoic chamber

1 GHz, Fig. 3.2.4a and Fig. 3.2.4b compares the measured and simulated patterns for $\phi = 0°$ (**E**-plane) and $\phi = 90°$ (**H**-plane) respectively. While these figures show that the

simulation does reasonably well at predicting the far-field pattern of the structure, there is nonetheless a noticeable deviation from the measured results. This serves to illustrate the importance of using real-world measurement data in order to properly characterise a system.

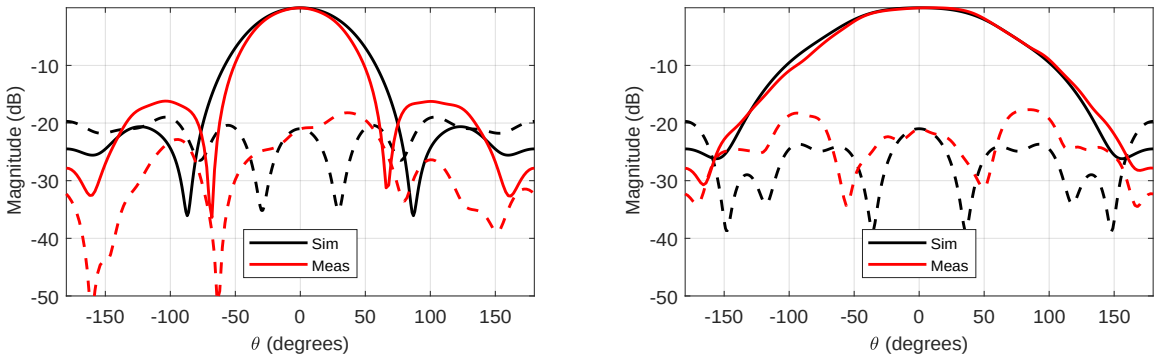


(a) $\phi = 0°$ (b) $\phi = 90°$

Figure 3.2.4: Comparing simulated and measured radiation patterns at 1 GHz, where the solid and dotted lines represent the co- and cross-polar magnitudes respectively

Although the NSI measurement system performs all the necessary processes in order to produce the complete far-field patterns, considering that a great deal of this work is concerned with near- to far-field transformation, we would be remiss if we did not use this opportunity to test and compare the performance of FIAFTA on this measured data set. Referring back to the discussion of transformation algorithms in Section 2.3, it is obvious that the planer plane wave transformation is not suitable for this spherical near-field measurement. However, the irregular sampling capabilities of FIAFTA means that it can be used in this example. Given the maximum dimensions of the AUT and probe as 341 mm and 242 mm respectively, the multipole order required is calculated using (2.3.52) as

$$\begin{aligned} L &= \frac{1}{2}(kd) + 10 \\ &= \frac{1}{2}\left(\frac{2\pi}{\lambda} \cdot (0.341 + 0.242)\right) + 10 \\ &= 16.1094 \\ &\approx 18\,, \end{aligned} \tag{3.2.1}$$

at 1 GHz, where we have rounded off to the nearest even integer as this seems to be preferred by the quadrature routine. This results in the discrete set of 684 unknown plane waves emanating from the AUT. The necessary mathematical procedures required by FIAFTA are coded in MATLAB and used to produce the result shown in Fig. 3.2.5, which is compared against the reference far-field given by the NSI system. It is seen how the result from FIAFTA matches the reference almost exactly for both polarisations. Also

shown in the figures is the direct measured near-field data, which possesses a narrower beam than the transformed far-field. This near-field data was sampled on the spherical surface of radius $r = 1.12$ m centred on the AUT, with an angular spacing between samples $\Delta\phi = \Delta\theta = 2.5°$ between $-90° \leq \phi \leq 90°$ and $-180° \leq \theta \leq 180°$ respectively. With M=73 samples in the $\phi$-direction and N=145 samples in the $\theta$-direction, we have a total of 10 585 near-field samples, which is more than sufficient to solve for the 684 unknown radiating plane waves of the AUT. It should be noted that the result from FIAFTA is achieved by assuming an ideal probe antenna, i.e. no probe correction. We can see that this has little consequence on the predicted far-field. Given that this is a spherical measurement, probe correction is seen as less important as the direction of maximum gain of the probe is always directed toward the AUT.

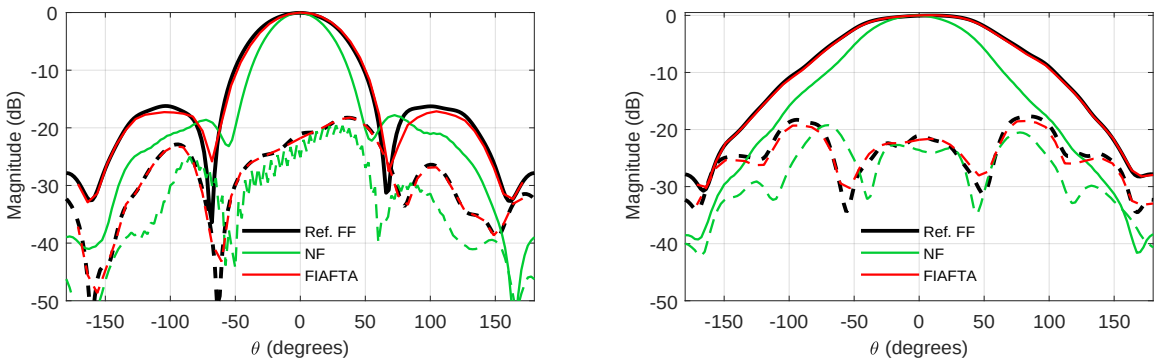


(a) $\phi = 0°$ (b) $\phi = 90°$

Figure 3.2.5: Comparing transformed far-field of FIAFTA with reference given by NSI system for 1 GHz, where the solid and dotted lines represent the co- and cross-polar magnitudes respectively

### 3.2.2 Receiver System

The back-end system, designed by Hardie Pienaar [53], is shown in Fig. 3.2.6. At present, the system does not posses any digital beam forming capabilities and, instead, a linear combiner is used to add the signals from each element in phase, essentially forming a total array pattern with one main beam directed towards zenith. As each element is dual-polarised, we use two separate 16:1 combiners producing a single output for each polarisation. These signals are fed into two Airspy R2 software defined radios (SDRs), which are controlled by a Raspberry Pi micro-computer. With various open-source software libraries targeted at SDR applications, we can run scripts to perform simple measurement routines. The system allows for these to be executed remotely, where a media converter handles the communication between the fibre-optic network on-site and the Raspberry Pi. A DC source supplies power to these components, as well as providing the necessary voltage to bias the low-noise amplifiers (LNAs) present in the antenna through the bias T

network. This back-end system is to be housed in an aluminium box and located on site, where it can be used to monitor the state of the antenna through running various test measurements. Given the proximity to other radio telescope experiments, the SKAAP system must not be a source of any radio frequency interference (RFI) at a level which may impact these projects. As such, the aluminium box is designed to add shielding, as well as to protect the system from the weather.

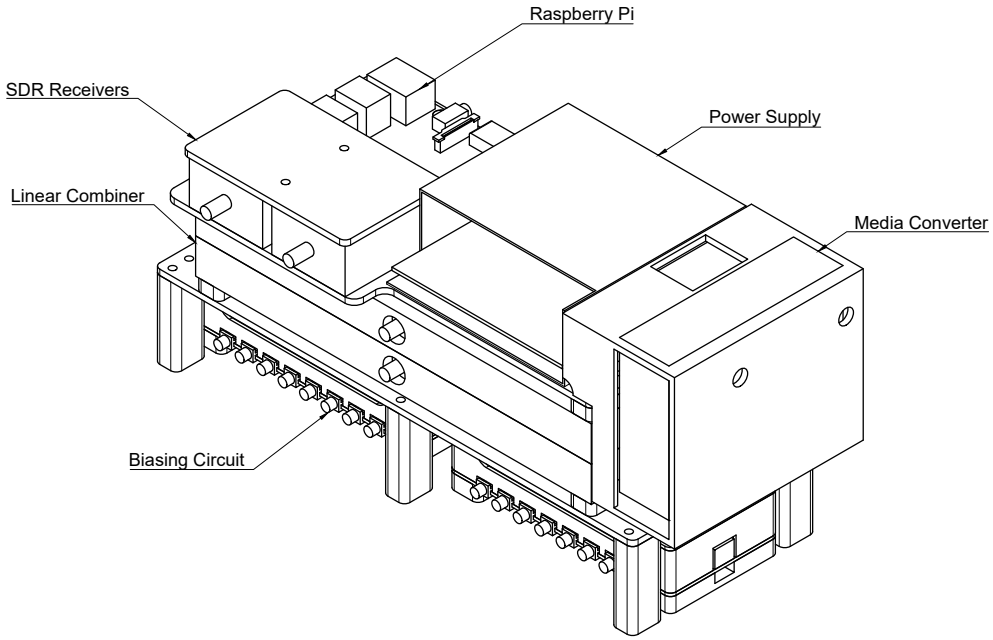


Figure 3.2.6: Schematic of SKAAP receiver box [53]

## 3.3 UAV Platform

The UAV platform we consider in our investigation was designed and built by Dr. Hardie Pienaar, as part of a continuation of his work in [54]. The platform, a schematic of which is shown in 3.3.1, is a third generation of flying electromagnetic unit (FEMU 3.1) designed by Dr. Pienaar, which is configured to act as a transmitting test source to provide measurement data for receiving antenna systems. This is accomplished using onboard wave synthesisers, which generate and transmit a chosen test signal through two orthogonal printed dipole antennas, mounted on the underside of the platform. A Raspberry Pi Zero is used to control these wave synthesisers, as well as logging telemetric data such as position and orientation as a function of time.

Along with all necessary receivers allowing for remote control, the vehicle is also capable of full-autonomous flight. This is accomplished with the Pixhawk v2 flight controller

[55], which uses the open-source autopiloting software Ardupilot [56]. The Pixhawk contains a vibration-damped inertial measurement unit (IMU), which integrates digital gyroscopes, accelerometers and magnetometers to provide accurate determination of the vehicles angular rotation about three different axes, i.e. roll, pitch and yaw. These can in turn be related to the Eulerian angle rotations, introduced in Section 2.3.1, in order to determine the probe's transmitting pattern to be used in probe correction. In order for the position of the vehicle to be determined, the Pixhawk can be integrated with a global navigation satellite system (GNSS). We use the HERE+ v2 kit [57], which features a GPS antenna and GNSS module (NEO-M8P [58] with a quoted accuracy of 25 mm) fitted to the vehicle and provides data on the position of the vehicle to the Pixhawk. To improve the accuracy of the system, a second GNSS module forms part of a ground base station. By using this as a reference, differential GPS (DGPS) and real time kinematic (RTK) technology can be used to determine the position of the drone relative to the base station to a centimetric accuracy.

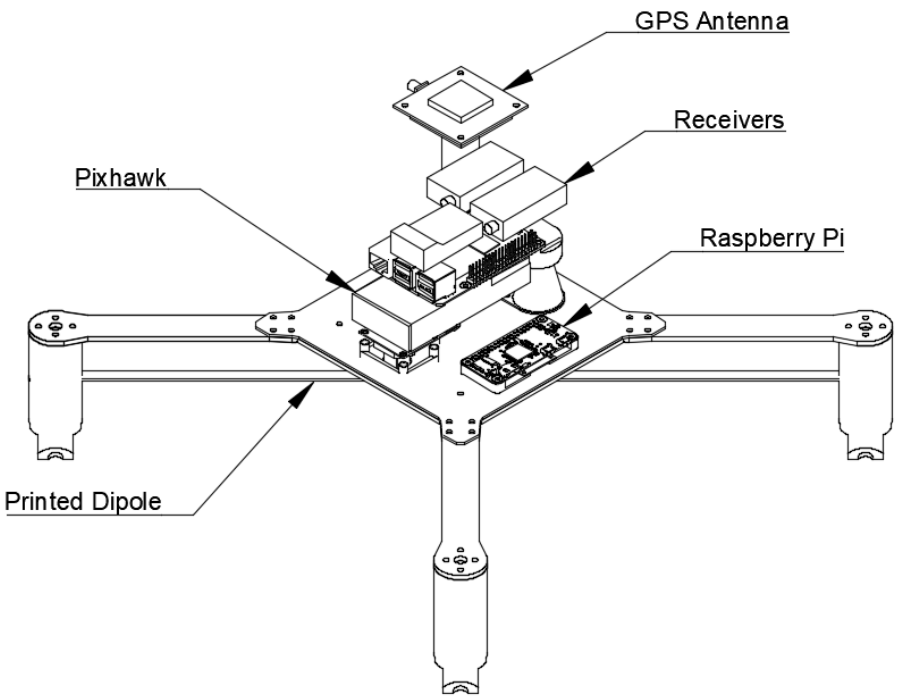


Figure 3.3.1: Schematic of FEMU 3.1 [53]

# Chapter 4

# Probe Positional Error Sensitivity

## 4.1 Introduction

A primary concern when considering the viability of UAV-based antenna field measurements, is the ability to accurately determine the position of the UAV at each sample location. While amplitude-only far-field measurements can produce acceptable results even for relatively high probe position uncertainties, the additional phase requirement in near-field measurements means that near- to far-field transformation algorithms are more sensitive to random probe positioning errors, where a phase error of less than 12 degrees is seen to produce acceptable results for most algorithms [26]. This corresponds to an allowable position inaccuracy of $\lambda/30$, or from around 22 mm down to 7 mm for our frequency band of interest. Given that the NEO-M8P GNSS module used in the positioning system described in the previous chapter has a quoted horizontal position accuracy in the range of 25 mm [58], the ability of the UAV system to produce usable results is of serious concern and warrants further investigation.

Analysis of the effects of various errors on the performance of the PPWE are presented in [59] and [60]. While these analyses consider predominately high-gain antennas, the nature of the MFAA means we are more concerned with the ability to measure antennas with a wide FoV. Such an analysis is performed in [61], where the effect of horizontal position errors on the predicted far-field pattern of a radiating dipole is investigated. We follow a similar procedure here, where we include vertical position error and compare the performance of the PPWE to that of FIAFTA. Transverse errors in the $x$- and $y$-directions will, in general, impact the accuracy of the measurement differently to those in the vertical/longitudinal $z$-direction. The level of sensitivity to either transverse or longitudinal position inaccuracies is dependent on the specific pattern being measured, where the direction of propagation indicates the direction of maximum phase change and thus the direction along which positional errors have the most impact on the accuracy of the measurement. While an error analysis of FIAFTA, akin to that undertaken here, is performed in [62], the positional error levels were far lower than that considered for this study.

We start by investigating the effect of probe positional errors when measuring the radiated field of a dipole above an infinite ground plane. With this simple example, we develop the necessary procedure to analyse and compare the effect of varying levels of positional error on the performance of both the PPWE and FIAFTA. Many of these results

have been previously presented by the author in [63], where the analysis is extended here to consider the MFAA antenna element introduced in Section 3.2.1. Ignoring non-ideal probe effects, we simulate near-field measurements of this antenna, where we assume that the positional inaccuracies are the only source of error. In so doing, we seek to determine whether near-field measurements of the MFAA is at all possible when faced with the positional inaccuracies associated with DGPS/RTK.

## 4.2 Dipole Test Antenna

We start with the AUT as an $\hat{\mathbf{x}}$-polarised half-wavelength dipole, situated $\lambda/4$ above an infinite ground plane. This provides an antenna with a wide FoV, akin to that of the MFAA, while enabling a short simulation time when modelled in FEKO [64]. Owing to the random nature of the positional error, this short simulation time is beneficial as it allows us to repeat the experiment multiple times and give some insight as to the typical performance of both algorithms. We excite the dipole with an ideal voltage source and directly extract the **E**-field components $E_x$ and $E_y$ on a 10x10 m plane at $z = 3\lambda$ above the AUT. With this, the maximum polar angle $\theta_{max}$ at which we can expect a valid result of the transformed far-field can be calculated from (2.3.50). Given that both the size of the AUT and $z_0$ are dependent on the wavelength in question, $\theta_{max}$ is a function of frequency and falls in the range $67.5° \leq \theta_{max} \leq 82.8°$ for the frequency band 450 MHz–1.45 GHz. For the duration of the analysis, we will restrict the FoV of interest to $\theta \leq 60°$.

By directly computing the field components, as given by FEKO, we neglect the effects of non-ideal probes and focus purely on errors caused by the incorrect position of measurement locations. It is also worthwhile to note that, given the small size of the dipole, the sample locations may very well reside in the far-field of the AUT, rendering near- to far-field transformation unnecessary. However, the focus of this experiment is not on the ability to calculate the far- from the near-field, but rather on the effect of positional errors. Given that we are attempting to measure the phase of the field, the transformation algorithms still exhibit sensitivity to erroneous measurements of this phase and the premise of the experiment remains valid.

The sample locations for the PPWE are set out according to Section 2.3.1, where the sample spacing is chosen as $\Delta x = \Delta y = \lambda/2$ to satisfy the minimum Nyquist criteria. For FIAFTA, we utilise a spherical sample spacing projected on to the measurement plane at

$z_0$, as detailed in Section 2.3.2, with the multipole order being calculated by (2.3.52) as

$$\begin{aligned} L &= \frac{1}{2}(kd) + 10 \\ &= \frac{1}{2}\left(\frac{2\pi}{\lambda} \cdot \frac{\lambda}{2}\right) + 10 \\ &= 11.5708 \\ &\approx 12\,, \end{aligned} \tag{4.2.1}$$

where we have rounded up to the nearest even integer. With this, directions of the discrete set of plane waves over the Ewald sphere of the AUT are determined using a suitable quadrature rule. Here, we use a Legendre-Gauss-Lobato scheme, which differs slightly from the more common Legendre-Gauss rule, in that it includes a sample at the pole. Furthermore, given that we are measuring in the positive $z$ half-space, only plane waves propagating from the forward hemisphere of the Ewald sphere will contribute to the measured response at each location. Therefore, we restrict the analyses to determining only these plane wave currents, resulting in a situation where the minimum number of samples required by FIAFTA is far less than that of the PPWE. Thus, in order to provide a fair comparison of the two algorithms, we choose values of $\chi_1$ and $\chi_2$ such that the total number of samples, as calculated from (2.3.62) and (2.3.63), is equal to that of the PPWE. This leads to a system where the number of unknowns is significantly less than the number of field measurements, making for an overdetermined system which may be more resilient to errors.

### 4.2.1 Error Calculation

To investigate the effect of inaccurate measurement locations, random positional error is artificially added to each rectangular component of the coordinates defining the sample locations $(x, y, z)$, giving the noisy positions $(x_n, y_n, z_n)$ defined by

$$(x_n, y_n, z_n) = (x + n_x, y + n_y, z + n_z)\,, \tag{4.2.2}$$

where $n_x$, $n_y$ and $n_z$ are randomly chosen from a normal distribution with a standard deviation $\sigma$ determining the level of positional error being investigated. We compute the field values at these noisy measurement locations in FEKO and use each algorithm to calculate the total far-field magnitude $E^{FF}_{total}$ at a distance of $r = 100$ m. By assuming that the samples were taken at the ideal coordinates $(x, y, z)$ when performing the transforms, the scenario is analogous to that of a near-field measurement plagued by some level of unknown, random probe positing error. The result from each algorithm is then compared to the reference far-field $E_{REF}$, taken directly from FEKO at $r = 100$ m. Given that the noisy measurement locations are randomly chosen, the experiment is repeated a number

of times for each level of error, which allows us to determine the general response of each algorithm. Then, for the $k^{th}$ run, the far-field error seen in the direction $(\theta, \phi)$, as normalised to the reference, is calculated as

$$e_k(\theta,\phi) = \frac{|E_{REF}(\theta,\phi)| - |E^{FF}_{total}(\theta,\phi)|}{|E_{REF}(\theta,\phi)|}\,, \tag{4.2.3}$$

which gives an error map over the entire FoV. By repeating the experiment $N$ times, we can analyse the average error seen in the transformed far-field, given as the root-mean-square (RMS) error

$$e_{RMS}(\theta,\phi) = \sqrt{\frac{1}{N}\sum_{k=1}^{N}(e_k(\theta,\phi))^2}\,. \tag{4.2.4}$$

Furthermore, in order to gauge the worst-case response of the transformations, it is beneficial to consider the maximum error seen at each angle

$$e_{max}(\theta,\phi) = max(\mathbf{e}(\theta,\phi))\,, \tag{4.2.5}$$

where $\mathbf{e}(\theta,\phi)$ is the vector $[e_1, e_2, ..., e_N]$ and $max(\cdot)$ takes the maximum seen at each angle $(\theta,\phi)$. It would be helpful for analyses if we could reduce these error maps, giving the error levels seen at each angle, to a single value describing the total error seen over the FoV of interest. This is achieved by integrating the error map in question over the FoV of interest (taken here as 60° from zenith), such that

$$e_i = \frac{1}{S}\int_0^{\pi}\int_{-\frac{\pi}{3}}^{\frac{\pi}{3}} e(\theta,\phi)\cos(\theta)d\theta d\phi\,. \tag{4.2.6}$$

where we have normalised to the surface area $S$ of the FoV

$$S = \pi\left(\sin^2\left(\frac{\pi}{3}\right) + \left(1-\cos^2\left(\frac{\pi}{3}\right)\right)\right)\,. \tag{4.2.7}$$

The scalar value $e_i$ provides a metric which can be used to easily compare the performance of each algorithm to varying levels of positional error. All of these error metrics can either be given in terms of decibels (dB), or, considering the normalisation in (4.2.3), a percentage error (%) of the reference far-field pattern.

### 4.2.2 Results

We begin by investigating the performance of each algorithm when subjected to positional error levels in the range $\lambda/50 \leq \sigma \leq \lambda/5$. The affected far-field patterns for various levels of positional error in this range can be seen in Figure 4.2.1, where we compare the PPWE and FIAFTA to the reference pattern. Included in the legends is the far-field scalar error $e_i$, calculated using (4.2.6) and given as a percentage, which allows one to reconcile this

metric with the affected pattern plot. It can be seen that an error level of around $e_i = 10\,\%$ corresponds to an FF pattern that represents the reference to some degree of accuracy. Above this, with error levels reaching 15–20 %, the resulting transformed FF patterns are seen to degrade past a point where any usable data could be extracted. The graphs show that FIAFTA produces usable results for error levels as high as $\sigma = \lambda/10$, whereas the PPWE begins to break down long before this, at around $\sigma = \lambda/30$. Further illustrating

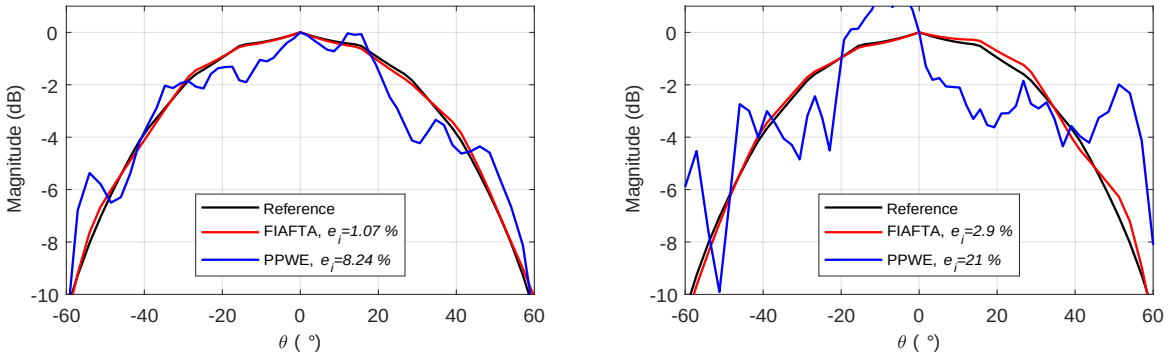


(a) $\sigma = \lambda/50$




(b) $\sigma = \lambda/20$

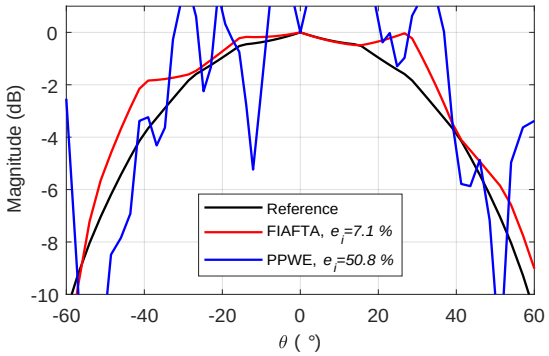


(c) $\sigma = \lambda/10$

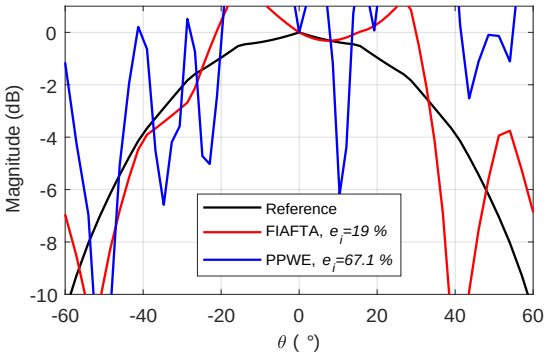


(d) $\sigma = \lambda/5$

Figure 4.2.1: Comparing the performance of FIAFTA and the PPWE for various positional error levels $\sigma$

the superior performance of FIAFTA, far-field error maps over the entire FoV, as given by (4.2.3), are displayed in Figs. 4.2.2 and 4.2.3 for the PPWE and FIAFTA respectively. These are plotted in terms of the directional cosines $\alpha$ and $\beta$ (also referred to as a $uv$-plot), where it is clear that FIAFTA is more stable for the positional error levels considered.

It can easily be seen that FIAFTA appears to be more resilient to positional error levels below $\lambda/10$. Above this and FIAFTA is seen to perform worse than the PPWE. This is demonstrated in Fig. 4.2.4a, which compares the maximum and RMS errors ($e_{max}$ and $e_{RMS}$), as converted to scalars via (4.2.6), for increasing levels of positional error. It can be seen that FIAFTA outperforms the PPWE up to around $\sigma = 0.22\lambda$. Beyond this and the RMS error of FIAFTA is seen to be greater than that of the PPWE. This is of little significance considering the fact that, at this error level, both patterns are corrupted

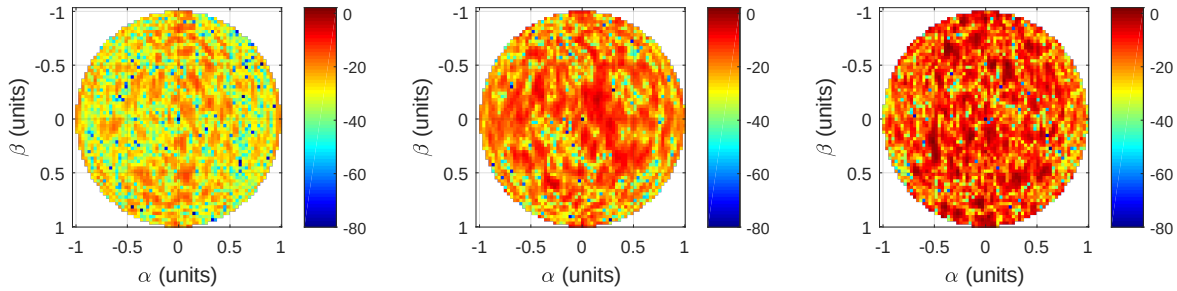


(a) $\sigma = \lambda/50$ (b) $\sigma = \lambda/20$ (c) $\sigma = \lambda/10$

Figure 4.2.2: Error maps seen in PPWE transformed far-field for increasing positional error

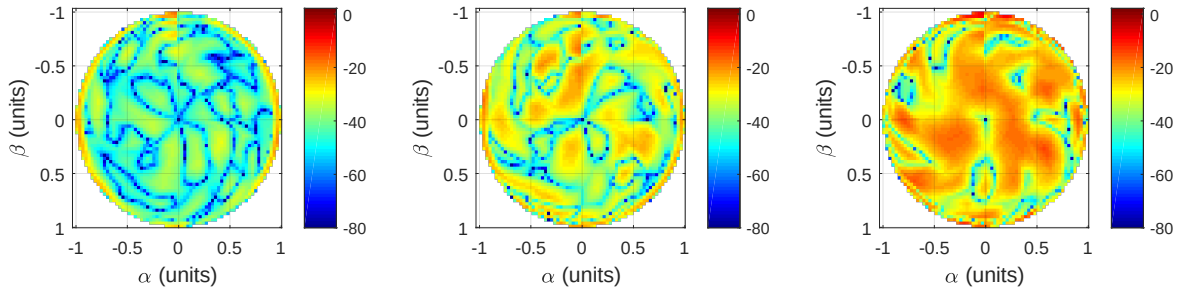


(a) $\sigma = \lambda/50$ (b) $\sigma = \lambda/20$ (c) $\sigma = \lambda/10$

Figure 4.2.3: Error maps seen in FIAFTA transformed far-field for increasing positional error

beyond being able to serve any practical purpose.

We move on to investigate the effect of positional errors associated with the GPS system in question, for our frequency band of interest. We choose a lower error level as $\sigma_{lower} = 1$ cm and an upper level as $\sigma_{upper} = 5$ cm and compute the maximum error seen in the predicted far-field patterns for the frequency band 10 MHz–1450 MHz. The lower level of 1 cm corresponds to accuracy achievable through use of optical or laser tracking systems, such as those demonstrated in [26]. The upper limit of 5 cm corresponds to the accuracy of DGPS or RTK systems. Given that the 2.5 cm accuracy listed in [58] for the GPS module in question is calculated for ideal conditions (clear skies, full satellite lock, etc.) a 5 cm error for a real measurement seems reasonable, and maybe even slightly optimistic, considering that other sources of error have not been taken into account. We repeat the experiment 50 times ($N = 50$), and compute the maximum error $e_{max}$, which is subsequently converted to a scalar using (4.2.6). The result is shown in Fig. 4.2.4b, where the shaded regions show the area between the lower and upper positional error levels, $\sigma_{lower}$ and $\sigma_{upper}$. It can be seen that FIAFTA outperforms the PPWE over the whole frequency band. Considering the upper error level $\sigma_{upper} = 5$ cm, we see that the PPWE starts producing unsatisfactory results even before 100 MHz, where the maximum

far-field error is around 20%. Contrary to this, FIAFTA produces an acceptable error level of 3% at 100 MHz. However, as we approach our band of interest, this is seen to rise to 23% at 450 MHz, indicating that FIAFTA produces unsatisfactory results throughout our band of interest. Considering the lower error level $\sigma_{lower} = 1$ cm, we see that FIAFTA would produce reasonable results throughout the band of interest, reaching a level of 12% at 1450 MHz. On the other hand, the PPWE still produces unsatisfactory results over the whole band for this amount of positional error, where it is seen to rise from around 20% at 450 MHz to 60% at 1450 MHz. These results show how the PPWE produces highly

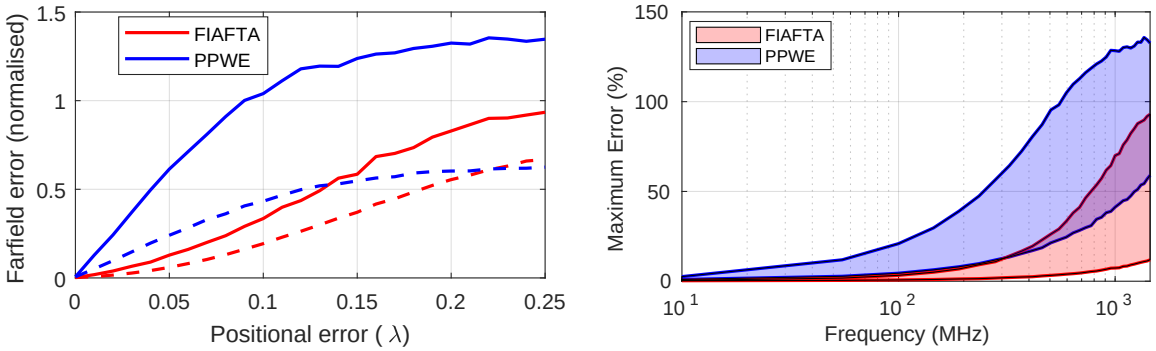


(a) Maximum (solid) and average (dotted) far-field pattern error

(b) Error bounds for positional error level between $1 \leq \sigma \leq 5$ cm

Figure 4.2.4: Observed far-field pattern error

corrupted far-field patterns, even for modest levels of positional error, indicating that it is unsuitable for our purposes. Although both algorithms are plagued by an erroneous phase measurement, given that the PPWE performs a FFT on the measured data, irregular sample locations are seen to violate the fundamental requirement of the FFT on a constant sample spacing. The irregular sampling capabilities of FIAFTA results in an algorithm more resilient to positional error, however, for $\sigma = 5$ cm in the frequency band of interest, the transformed far-field is largely unsatisfactory. This brings into question the viability of near-field measurements performed in this manner and we proceed to investigate methods of improving these results below.

## 4.3 MFAA Antenna

The results presented in the above analysis suggest that the PPWE is unsuitable for near-field measurements affected by probe positional inaccuracies associated with DGPS/RTK (where $\sigma = 5$ cm can be seen as a somewhat optimistic expected error level). While, FIAFTA is seen to produce useful results up to the 100 MHz range, the algorithm begins to break down as we approach our band of interest, where a maximum error of around 20 % is seen at 450 MHz. Considering that the objective of this study is to perform UAV

measurements in band 450–1450 MHz, this is a troublesome result and begs the question whether near-field measurements of the MFAA using UAVs equipped with DGPS/RTK is at all feasible.

We therefore extend the analysis to consider the MFAA antenna presented in Section 3.2.1 and simulate the noisy near-field measurements of the single antenna, as performed for the dipole in the preceding analysis. By considering an error level of $\sigma = 5$ cm in the frequency band 450–1450 MHz, we provide some insight into what one may expect from a typical UAV measurement utilising DGPS/RTK. We begin the analysis at 450 MHz, with the diameter of the smallest sphere enclosing the MFAA antenna given as $d = 0.34$ m, the multipole order is calculated according to (2.3.52) as $L = 12$. Setting up the spherical projected planar sample locations as per (2.3.65) and (2.3.66), we choose $\chi_1 = \chi_2 = 1$ to provide the minimum number of samples necessary to solve for the set of plane wave currents. The resulting transformed Ludwig 3 co- and cross-polarised far-field patterns are shown in Fig 4.3.1a and Fig 4.3.2a respectively, where the 5 cm positional error has notably corrupted the transformed pattern and resulted in a far-field error around 18%. It is worthwhile to note that the 168 measurement samples used here is significantly less than the 1024 samples required to fulfil the Nyquist requirements of the PPWE. In an effort to improve the results of the transform, we increase the number of measurement samples by incrementing $\chi_1$ and $\chi_2$. Choosing these values such that the total number of samples coincides closely to multiples of the Nyquist rate of 1024 samples, we compute the transformed far-field and plot the resulting co- and cross-polarised patterns in Fig. 4.3.1 and Fig. 4.3.2. For 1216 samples (close to the Nyquist sampling rate) the transformed far-field is seen to improve to an error level of 7.6% and, as evident by Fig. 4.3.1b and Fig. 4.3.2b, is seen to represent the reference pattern more closely. Doubling this sampling rate, the result for 2430 samples is shown in Fig. 4.3.1c and Fig. 4.3.2c, for the co- and cross polarised patterns respectively. While the calculated far-field error of 7.97% is higher than that of the previous plot with half the number of samples, visually the transformed pattern seems to represent the reference more accurately. Finally, increasing the number of samples to 4864 (just under 5 times Nyquist) is seen to improve the resulting error to around 4%. As can be seen from Fig 4.3.1d and Fig. 4.3.2d, this produces a respectable result which accurately represents the reference pattern within 60° from zenith. These results suggest that suitable performance of FIAFTA can be achieved, for a frequency of 450 MHz and positional error $\sigma = 5$ cm, if a suitable number of measurement samples are taken.

In the above, we showed that UAV pattern measurements of the MFAA may be viable at the beginning of the band of interest (450 MHz). The question remains whether the same procedure of increasing the number of samples can be used to provide suitable results for higher frequencies in the band. We therefore repeat the procedure at a number of frequencies throughout the band, namely 750 MHz, 1 GHz, 1.25 GHz and 1.45 GHz.

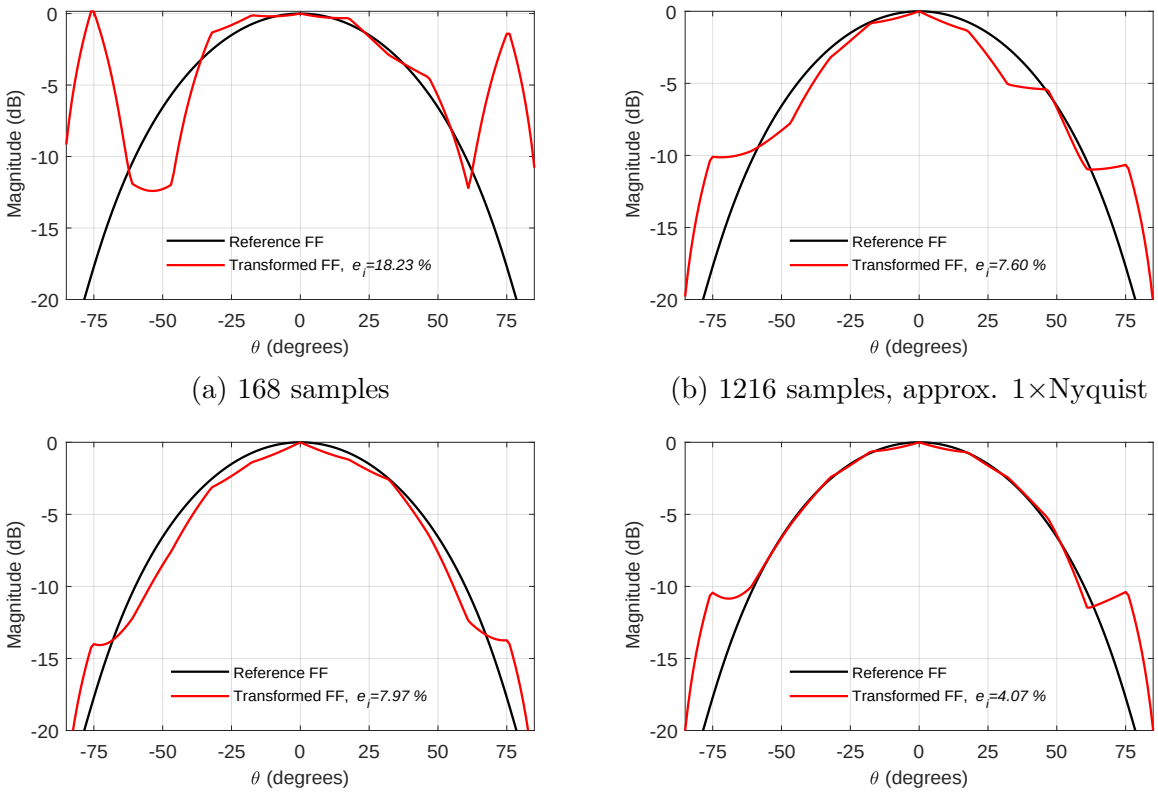


(a) 168 samples

(b) 1216 samples, approx. 1×Nyquist

(c) 2430 samples, approx. 2×Nyquist

(d) 4864 samples, approx. 5×Nyquist

Figure 4.3.1: The effect of increasing number of samples to FIAFTA transformed co-polarised far-field, for a positional error $\sigma = 5$ cm at 450 MHz

Again with a 5 cm positional error, we record the far-field error seen as we increase the number of samples up to just under 12 times the Nyquist rate for each frequency. The result, given in Fig. 4.3.3, shows the percentage far-field error vs. the number of samples for each frequency. It can be seen that for frequencies of 1 GHz and lower, we are able to decrease the far-field error to less than 10% by taking a suitable amount of samples. However, for 1.25 GHz and 1.45 GHz, the error level does not decrease much below 20% and further increasing the number of samples is seen to have little effect. This suggests that UAV measurements performed in this manner may be viable up to 1 GHz, where Fig. 4.3.4 shows that the transformed far-field at this frequency provides a reasonable representation of the reference for both the co- and cross-polarisations, with an error level just below 7%. Comparing this to the result for 1.45 GHz, shown in Fig. 4.3.5, it can be seen that the transformed far-field has been notably corrupted, although it still resembles the reference somewhat. It should be pointed out that we have chosen to display the best results seen for the entire analyses, which, given the random nature of the sample locations, does not always correspond to the measurement with the most number of samples, as is evident from Fig. 4.3.3. Considering that we will not have the luxury of knowing what the pattern should be before a real measurement, the results given here can be seen as a best case scenario for a positional error of 5 cm. Furthermore, with

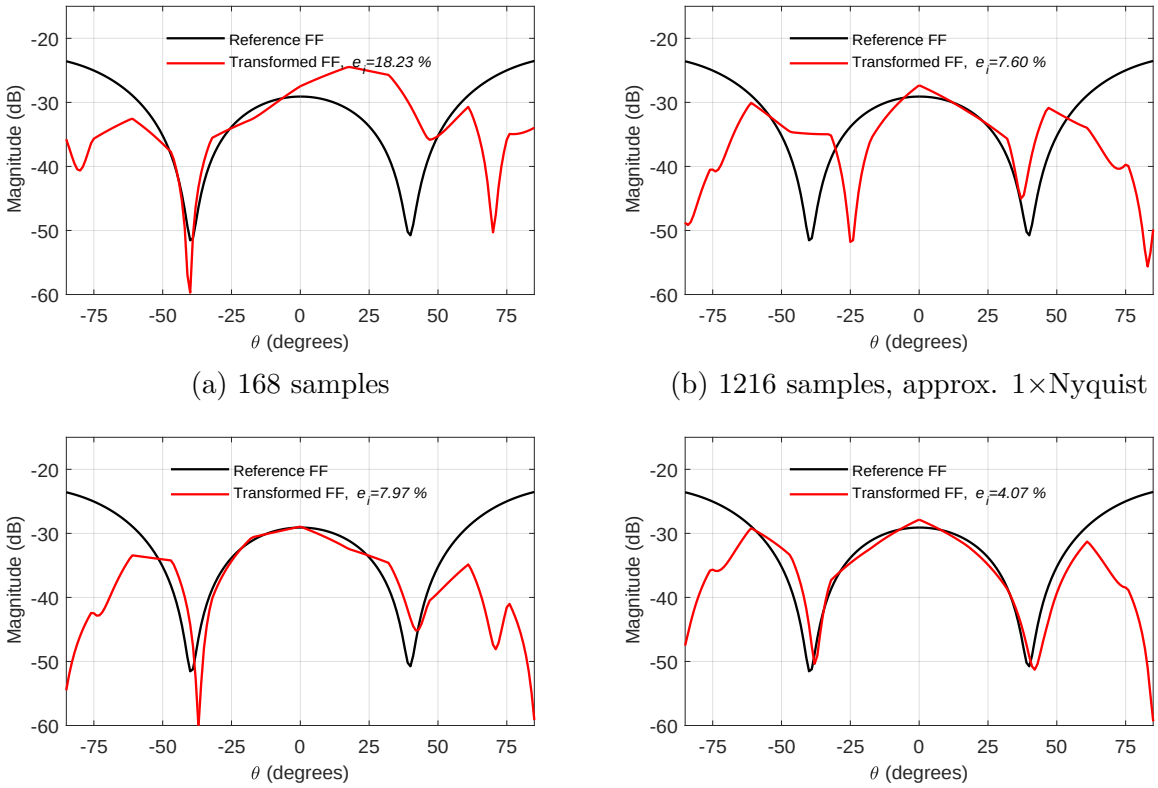


(a) 168 samples

(b) 1216 samples, approx. 1×Nyquist

(c) 2430 samples, approx. 2×Nyquist

(d) 4864 samples, approx. 5×Nyquist

Figure 4.3.2: The effect of increasing number of samples to FIAFTA transformed cross-polarised far-field, for a positional error $\sigma = 5$ cm at 450 MHz

the number of samples required to achieve the level of accuracy seen here at roughly ten times the Nyquist rate, the spacing between some sample points may be too small for the tolerance of the UAV positioning system. An alternative method is to include fewer samples, but average the results over multiple scans, thus improving the results akin to increasing the number of samples.

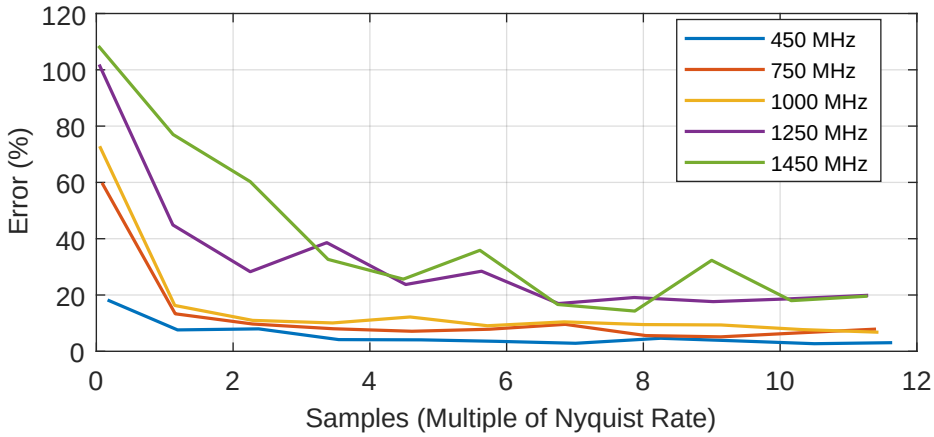


Figure 4.3.3: Error

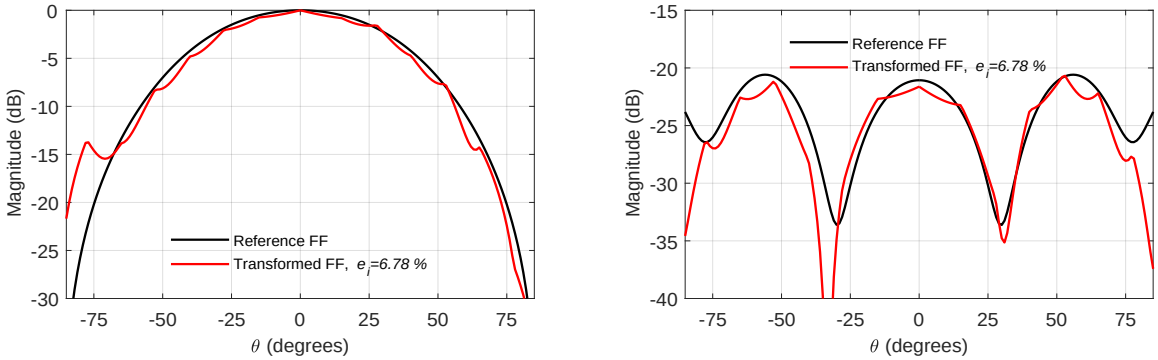


(a) Co-polarised (b) Cross-polarised

Figure 4.3.4: FIAFTA transformed far-field for 1 GHz with a positional error $\sigma = 5$ cm and 52890 samples (approx. 11×Nyquist rate)

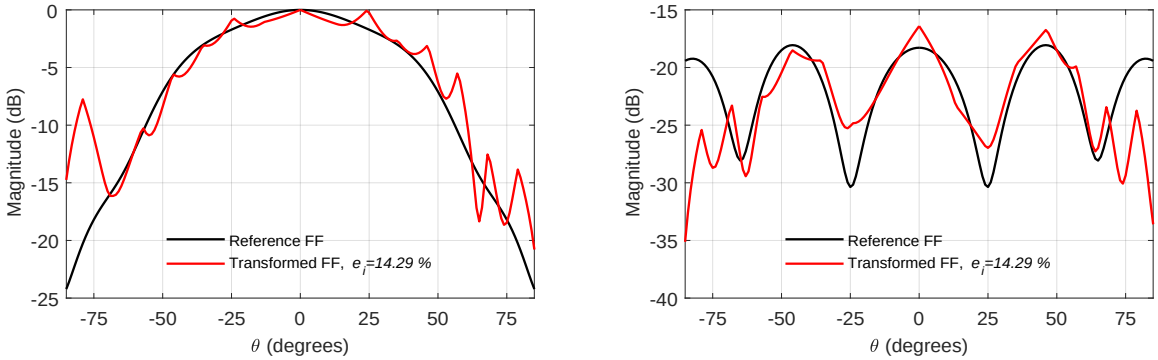


(a) Co-polarisation (b) Cross-polarisation

Figure 4.3.5: FIAFTA transformed far-field for 1.45 GHz with a positional error $\sigma = 5$ cm and 75628 samples (approx. 8×Nyquist rate)

# Chapter 5

# Probe Correction and Phase Retrieval

## 5.1 Introduction

Throughout the investigation in the preceding chapter, we assumed that the direct near-field components ($E_x$ and $E_y$) are measured at each sample location. This is possible during simulation as FEKO calculates these values mathematically, resulting in the full complex field measurements at each sample location. Such direct field measurements are not possible in reality, where the only manner in which to determine the field at a point is to record the response of a probe antenna to this field. The specific characteristics of this probe inevitably affect the measurement in some way, causing the measured response to differ from the actual field values. In order to accurately determine the true radiated field of an AUT, the effects of the probe must be removed from the measured data mathematically. This process, known as probe correction, is especially important in near-field measurements, where many methods have been developed over the years which consider various measurement geometries and probe antennas. Furthermore, in order to provide the necessary phase information required by near- to far-field transformations, the full complex signal of the response must be measured. This means that both source and received signals must be defined in relation to a common phase reference, which remains stable for the duration of the measurement. The accurate retrieval of this phase, together with a robust probe correction routine, is imperative if high-quality far-field patterns are to be obtained. When considering UAV based field measurements, some of these requirements may prove challenging in practise. Thus, this chapter investigates the matter further by simulating a real-world near-field measurement in FEKO and analysing the performance of FIAFTA in predicting the far-field pattern of the AUT (chosen as the MFAA prototype antenna introduced previously).

## 5.2 Perfect phase with probe correction

Given that an ideal isotropic antenna, which radiates/receives electromagnetic waves equally in all directions, is not physically realisable, the pattern of any probe will be directed in some way. This directionality results in the signals being transmitted/received from different directions with varying levels of gain, causing over- or under-estimation of

the true field values. Considering a planar near-field measurement using a probe antenna with one main beam directed along bore-sight, this directionality will cause the radiating field to be strongly received when the probe is positioned exactly above the AUT, and less so when moved off to the outer extents of the scan plane. While this effect is less pronounced in spherical near-field measurements, it is often still required to account for the characteristics of the probe (regarding polarisation, gain, etc.).

We proceed with the analysis by considering the $\hat{\mathbf{x}}$-polarised MFAA prototype unit element as the AUT. We choose a half-wavelength dipole, situated $\lambda/4$ above a finite ground plane, to act as our probe antenna. This choice allows for simple modelling in FEKO, as well as providing a probe pattern directed along bore-sight which will serve to emphasise the effect of probe correction. Conforming to the configuration of a real-world drone measurement, the probe antenna will be excited with a voltage source and moved through the scan plane, while recording the voltage measured at the port of the AUT. With the frequency set to 1 GHz, we simulate the measurement over a $10\times10$ m scan plane, positioned $z_0 = 3\lambda$ above the AUT. The sample coordinates are chosen across a rectilinear grid, with a Nyquist sample spacing $\Delta x = \Delta y = \lambda/2$, resulting in the $M\times N$ sample plane, where $M = N = 68$. In order to determine both the co- and cross-polarisation patterns of the AUT, it is necessary to perform two measurements with different probes. This is accomplished by simply rotating the dipole 90° about its $z$-axis, in order to form an $\hat{\mathbf{x}}$- and $\hat{\mathbf{y}}$ polarised antenna. The recorded voltage at the AUT for each probe orientation gives us the two responses $U_1$ and $U_2$, where their respective magnitudes over the sample plane are shown in Figs. 5.2.1a and 5.2.1b. By keeping the phase of the source constant, we ensure that the measured voltage at the AUT is made with zero phase error.

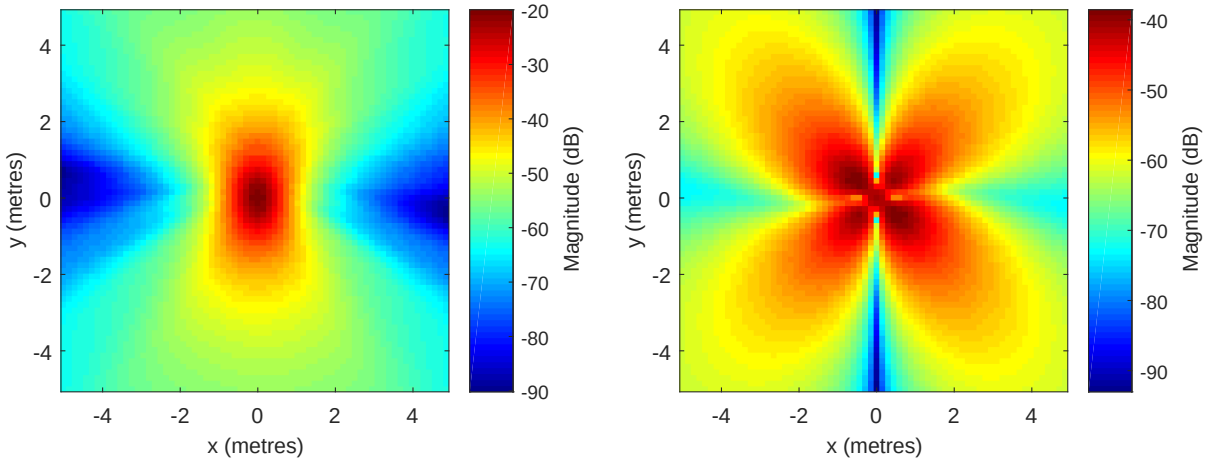


(a) $U_1$ with $\hat{\mathbf{x}}$-polarised probe

(b) $U_2$ with $\hat{\mathbf{y}}$-polarised probe

Figure 5.2.1: Magnitude of the voltage measured over the scan plane for both probe orientations

In order to account for the effects of the probe when predicting the far-field using FI-

AFTA, it is necessary to include the probe far-field receiving pattern, represented by the term $\mathbf{P}^{1/2}(k_\phi, k_\theta, \phi_m, \theta_n)$ in (2.3.54). This requires the determination of the full complex field pattern of the probe, which would be available from a preceding near-field measurement. By keeping the orientation of the probe fixed during the measurement, its pattern remains constant and is not dependent on $\phi_m$ and $\theta_n$. During a real drone measurement, any deviation in the orientation should be measured with the various sensors outlined in Section 3.3, where the Eulerian angle rotations performed in Section 2.3.1 can be used to subsequently determine the probe pattern at each measurement location. The probe pattern here is determined by simulating the dipole in FEKO and extracting the radiated far-field. This pattern is interpolated over the discrete directions $k_{\phi p}$ and $k_{\theta q}$ determined by the quadrature rule over the Ewald sphere of the AUT. With a multipole order of $L = 16$, we calculate the transformed far-field patterns of the AUT and compare this to the reference for the azimuthal planes $\phi = 0\,°$, $\phi = 45\,°$ and $\phi = 90\,°$, shown in Fig. 5.2.2, Fig. 5.2.3 and Fig. 5.2.4 respectively. Also included in these plots is the uncorrected far-field patterns, calculated assuming an ideal probe was used in the measurement. It can be seen how not taking into account the directivity of the probe causes the uncorrected pattern to be underestimated in the off-axis directions. Results for the corrected patterns show how this is alleviated, resulting in a predicted far-field that represents the reference to a satisfactory degree of accuracy.

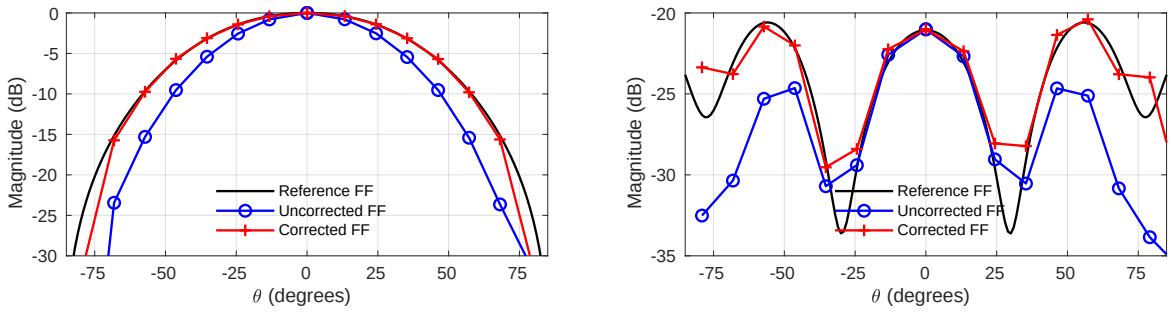


(a) Co-polarised (b) Cross-polarised

Figure 5.2.2: Comparing corrected and uncorrected radiation patterns from simulated measurement for $\phi = 0°$

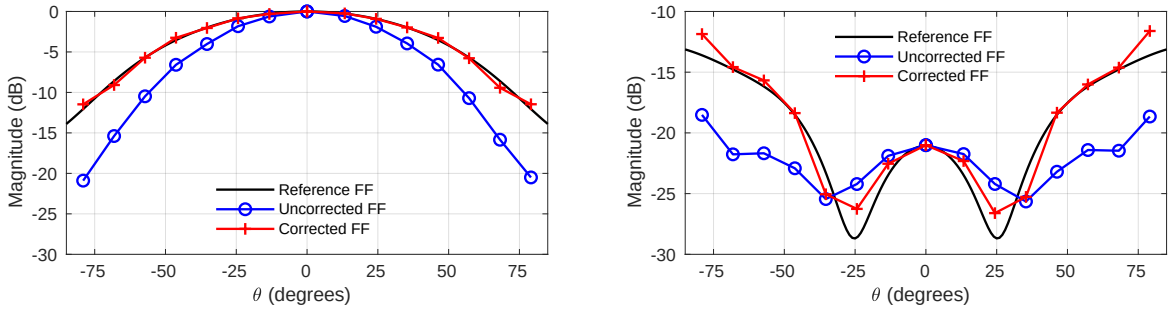


(a) Co-polarised (b) Cross-polarised

Figure 5.2.3: Comparing corrected and uncorrected radiation patterns from simulated measurement for $\phi = 45°$

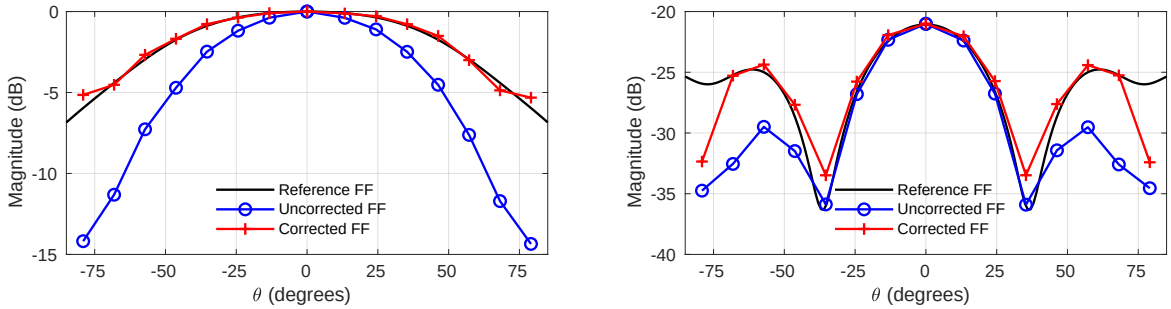


(a) Co-polarised (b) Cross-polarised

Figure 5.2.4: Comparing corrected and uncorrected radiation patterns from simulated measurement for $\phi = 90°$

## 5.3 Phase Extraction

Throughout our analysis thus far, the fields and measured quantities of interest have been considered as complex values in the frequency domain. In order to get a better handle on the phase extraction problem at hand, we consider the time domain equivalent of these quantities i.e. their instantaneous values. Considering the example of an $\hat{\mathbf{x}}$-polarised electric field $\mathbf{E}(\mathbf{r}) = E_x(x, y, z)\hat{\mathbf{x}}$. As with any complex number, we can write $E_x$ in exponential form as

$$E_x(x, y, z) = |E_x(x, y, z)|\, e^{j\Phi}\,, \tag{5.3.1}$$

where $\Phi$ is the phase of the field. The value of this field as it varies in time $t$ is given by the instantaneous field quantity $\tilde{E}_x$, where

$$\begin{aligned}\tilde{E}_x(x,y,z,t) &= \Re\left\{E_x(x,y,z)e^{j\omega t}\right\} \\ &= \Re\left\{|E_x(x,y,z)|\, e^{j(\omega t+\Phi)}\right\}, \\ &= |E_x(x,y,z)|\cos(\omega t+\Phi)\end{aligned} \tag{5.3.2}$$

where $\omega$ is the angular frequency $\omega = 2\pi f$ in radians/second with $f$ being the frequency in hertz. The above shows that, at a fixed point, we see a sinusoidally varying time signal of constant amplitude, which has been shifted along the time axis by $\Phi$. Considering the fact that our choice of initial time $t = t_0$ is an arbitrary one, the phase $\Phi$ must be defined in terms of some common reference point, which remains constant for all $(x, y, z)$. The accurate implementation of this phase reference is a major topic in near-field antenna measurements, where the requirements on stability increases with frequency.

Consider our measurement configuration, where a source voltage is used to excite the probe antenna, which, in turn transmits a signal received by the AUT causing a voltage response at its port. The phase of this measured voltage $\Phi_{meas}$ can be seen as the phase of the source $\Phi_{source}$ which has undergone a number of phase shifts caused by different contributing factors. Neglecting various phase contributions, such as that of the cables, we can write

$$\Phi_{meas} = \Phi_{source} + \Phi_t + \Phi_{free} + \Phi_r\,, \tag{5.3.3}$$

where $\Phi_t$ and $\Phi_r$ are the phase contributions of the transmitting probe and receiving AUT respectively, and $\Phi_{free}$ is the phase shift seen as the wave propagates through free space. This free space propagation is intrinsically included in the near- to far-field transformation being employed, which also accounts for $\Phi_t$ during probe correction. This leads us to conclude that, in order to properly extract the receiving phase characteristics of the AUT $\Phi_r$, the measured phase $\Phi_{meas}$ must be taken in reference to $\Phi_{source}$, i.e. one must record the difference between these two phase values. This is accomplished during simulation in FEKO by keeping the source phase zero and referencing all measurements to this zero phase. In practise, a two-port vector network analyser (VNA) is used, whereby the ports are connected to the AUT and probe via coaxial cables. Compared to a spectrum analyser, which purely measures the power amplitude of a received signal, the VNA generates and transmits a test signal on one port, whilst measuring the received response at the other. By tapping off a portion of the generated signal and using as a reference, both the amplitude and phase of the received wave can be measured, allowing for a full complex $S$-parameter characterisation. Considering near-field measurements performed with a UAV acting as a test source, we no longer have a closed system where the source and received signals are handled by the same device. Rather, the source is generated by wave synthesisers aboard the drone whilst the response at the AUT is measured separately, with no knowledge

of the test signal. While one could provide a common phase reference to the drone and AUT via cables, this would no doubt impede the movement of the UAV, as well as adding complexity to it's design. We must therefore resort to either providing a common phase reference in a semi-detached fashion, or make use of an algorithm to retrieve the phase information mathematically. Such phase-less, near- to far-field transformations exist which attempt to calculate the far-field radiation pattern of the AUT, given amplitude only near-field measurement data. These methods, such as those employing FIAFTA in [65] and [66], allow near-field measurements to be performed utilising a spectrum analyser to record the amplitude-only response of the AUT. Such algorithms often require the near-field to be measured on more than one surface, whereby the phase pattern of the AUT is reconstructed by considering different combinations of these measured responses. These added sampling requirements, together with the concern that probe positioning inaccuracies may seriously affect the performance of such phase reconstruction methods, leads us to consider an alternative option.

We resort to incorporating a second antenna which is used to provide a phase reference to the measured response at the AUT. With this reference antenna placed in the vicinity of the AUT, as depicted in Fig. 5.3.1, we simultaneously record the full complex response seen at both antennas during the measurement process. This can be accomplished in practise by using a 2-channel oscilloscope, which is set to trigger on the incoming reference signal $V_{ref}$, whilst recording the response seen at the AUT $V_{aut}$. This allows us to measure the phase difference between these two antennas which, assuming the receiving characteristics of the reference antenna are well-known, allows us to determine the true phase response of the AUT. This is accomplished by noting that the equivalent source currents, $\tilde{J}_\phi$ and $\tilde{J}_\theta$ employed by FIAFTA, are directly related to the far-field pattern of an antenna by (1.2.2). Thus, with the pattern of the reference antenna known, we can use FIAFTA to predict the response $V_{ref}$ for the given measurement configuration. Here, we use the translation operator $T_L(\mathbf{k}, \mathbf{r}_{rp})$ from (2.3.51) with $\mathbf{r}_{rp}$ the vector from the reference antenna to the probe. With the reference placed at $\mathbf{r}_r$ and probe at $\mathbf{r}_p$, we have $\mathbf{r}_{rp} = \mathbf{r}_p - \mathbf{r}_r$. This translation operator, together with the transmitting characteristics of the probe, is used in (2.3.54) to determine the predicted response $V_{ref}$ seen at the output of the reference antenna, whilst assuming the source voltage $V_s$ has a constant phase of zero. Then, by taking the difference between the phase of this predicted response to that of the actual $V_{ref}$ measured at the reference, we can determine the phase of $V_s$ at the probe. This phase is then taken into account in order to determine the true response of the AUT $V_{aut}$ from the random phase measurement.

Simulating this phase extraction problem in FEKO, we follow the configuration of Fig. 5.3.1, placing a reference antenna on the $y$-axis at $\mathbf{r}_r = y_{ref}\hat{\mathbf{y}}$, a distance $y_{ref}$ away from the AUT at the origin. As in Section 5.2, we excite the probe with the source voltage $V_s$, only this time, for each measurement point, the phase is randomly chosen out of a

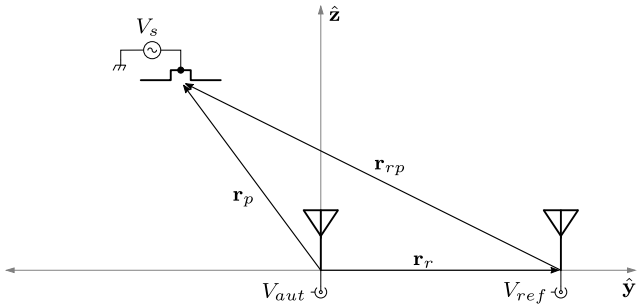


Figure 5.3.1: Measurement configuration with reference antenna to extract phase

uniform distribution between 0° and 360°. By assuming this source phase as unknown, we essentially mimic the situation of a practical near-field measurement performed with an unknown, random source. Moving on, we choose a seven element Yagi-Uda antenna (or Yagi for short) to function as a reference during our FEKO near-field measurement simulation. As shown by the schematic in Fig. 5.3.2a, the Yagi features an array of linear wire elements, where only a single element is supplied with a source voltage. The other elements are seen to couple to this driven element, and serve to reflect, and direct, the radiation in the broadside direction. The length and spacing of these elements is dependent on the wave-length of the desired operating frequency, where standard choices can be found in [67] for Yagi's with different boom lengths. Choosing a boom length of $1\lambda$ for a frequency of 1 GHz, we design an $x$-polarised Yagi according to the dimensions given in [67] and simulate in FEKO, where the resulting Ludwig 3 co-polarised far-field is shown in Fig. 5.3.2b. We incorporate this reference antenna into the near-field measurement

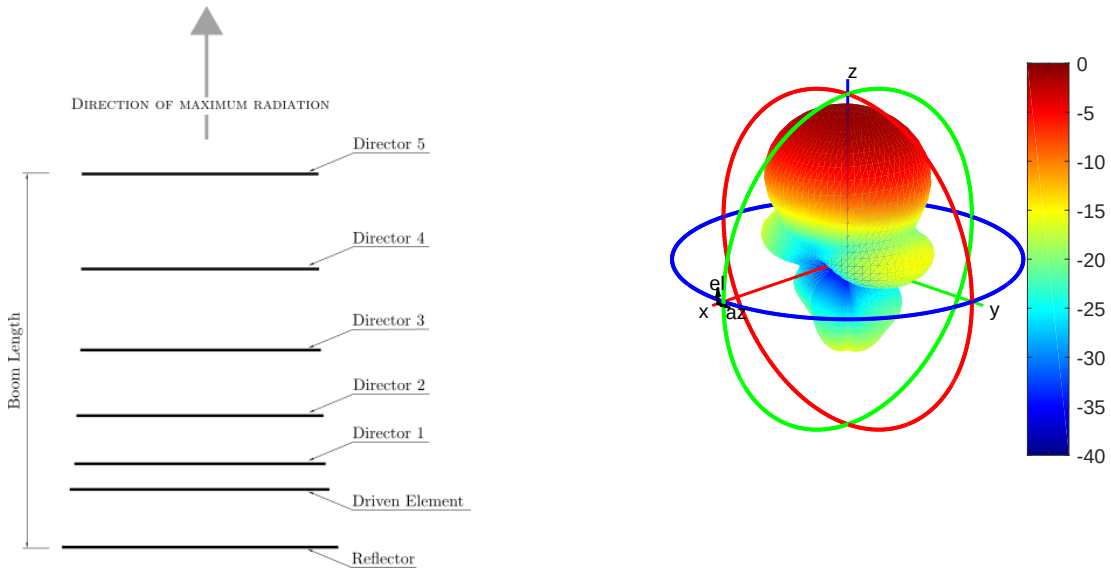


(a) Schematic (b) Co-polarised far-field

Figure 5.3.2: Yagi-Uda antenna with 7-elements aligned with $x$-axis

simulation, orientating the polarisation to align with the probe antenna for each scan. Using the same sampling configuration as in Section 5.2, and with the reference Yagi at

$y_{ref} = 1$ m, we simulate the near-field measurement whilst randomly varying the phase of the source voltage. Performing the phase extraction method defined above, we compute the far-field of the AUT using FIAFTA. The resulting patterns from this reconstructed phase measurement are shown for different azimuthal planes in Figs. 5.3.3–5.3.5, where, together with the ideal reference far-field, we also show the pattern resulting from the perfect phase measurement performed in Fig. 5.2. It can be seen that the predicted patterns obtained for the reconstructed phase measurement are notably corrupted, particularly in the $\phi = 90°$ plane. It is suspected that, at a separation distance of 1 m, there is significant mutual coupling between the AUT and reference antenna, serving to alter their radiation patterns from that computed when the antennas are isolated. Considering the $\hat{\mathbf{co}}$-polarised radiation pattern of the Yagi given by Fig. 5.3.2b, as well as that of the AUT given in Fig. 3.2.3a, we see that, for our measurement configuration, the $yz$-plane contains the maximum beamwidth of both antennas. This then may explain why the predicted pattern at $\phi = 90°$ is the most severely affected, as this is the plane which sees the most mutual coupling between the AUT and reference.

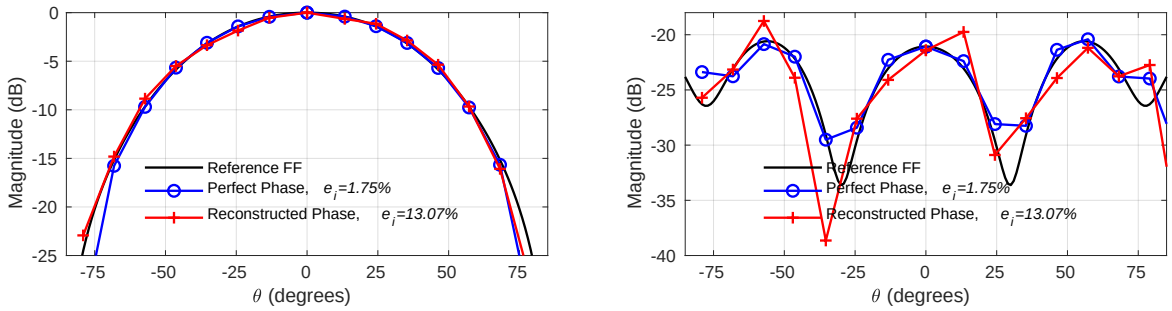


(a) Co-polarisation

(b) Cross-polarisation

Figure 5.3.3: Transformed far-field pattern at $\phi = 0°$ with reconstructed phase using reference antenna at $y_{ref} = 1$ m

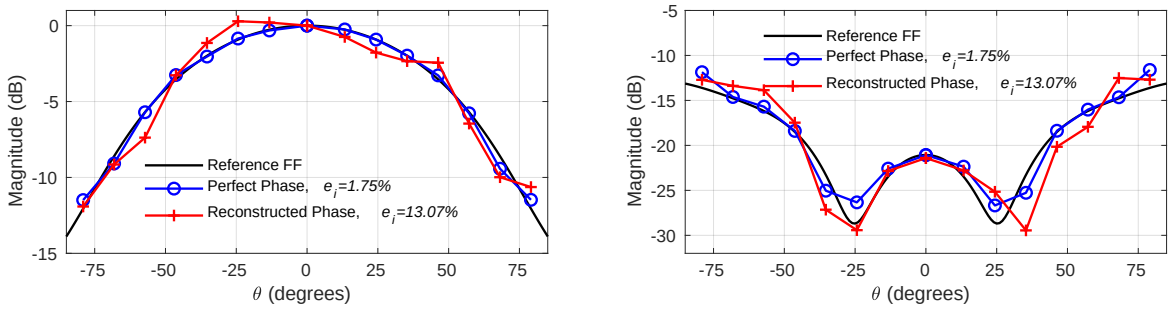


(a) Co-polarisation (b) Cross-polarisation

Figure 5.3.4: Transformed far-field pattern at $\phi = 45°$ with reconstructed phase using reference antenna at $y_{ref} = 1$ m

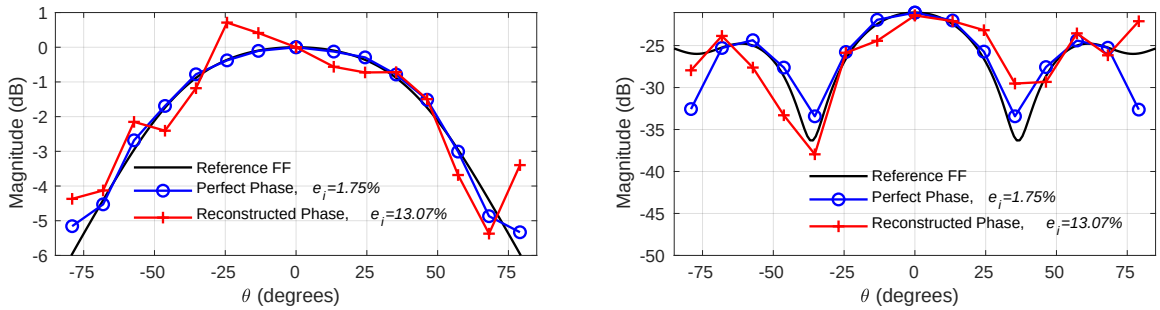


(a) Co-polarisation (b) Cross-polarisation

Figure 5.3.5: Transformed far-field pattern at $\phi = 90°$ with reconstructed phase using reference antenna at $y_{ref} = 1$ m

Proceeding to analyse this coupling effect more closely, we compute the direct far-fields of both antennas in FEKO, with the reference antenna placed 1 m away from the AUT. First, the AUT is driven with a voltage source and the direct far-field is computed when in the presence of the reference antenna, which is terminated in a 50Ω load impedance. The result is then compared to the far-field computed when the reference antenna is removed from the simulation. Given that the reference antenna's far-field pattern also affects the measurement, the above is repeated, only now with the voltage source driving the reference antenna and the AUT is terminated with the load. The resulting far-field patterns are shown in Fig. 5.3.6, where a slight but noticeable difference can be seen between the isolated and coupled far-field patterns. The far-field error $e_i$ shown in the legends is computed as in Chapter 4, with the FoV is taken as the whole forward hemisphere for $\theta \leq 90°$. While the coupling effect on the far-field patterns is slight, we should nevertheless increase the spacing between the antennas in order to avoid building errors into our system. To ascertain a suitable spacing between the reference antenna and

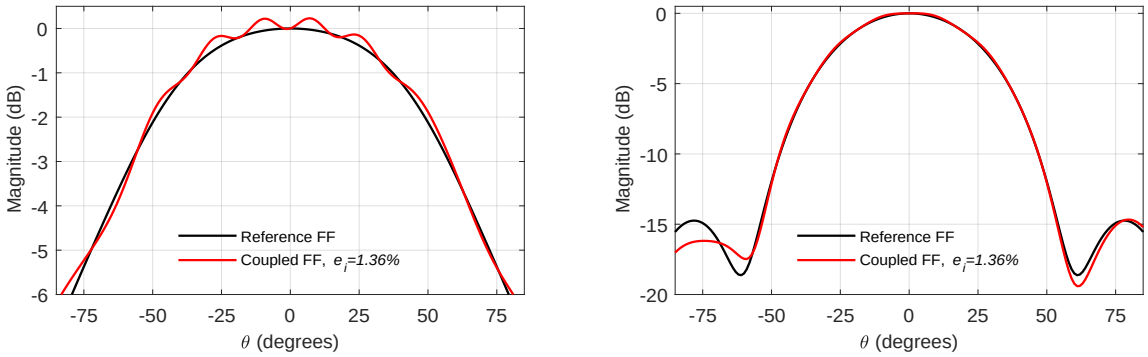


(a) AUT (b) Reference antenna

Figure 5.3.6: Comparing far-fields of isolated AUT and reference antenna to coupled patterns when $y_{ref} = 1$ m

the AUT, we repeat the above experiment while increasing the position of the reference antenna on the $y$-axis between 1 m $\leq y \leq$ 20 m. The resulting error $e_i$, in decibels, for both antennas is shown in Fig. 5.3.7, where it can be seen that $e_i$ closely matches the measured coupling between the two ports $S_{21}$. While Fig. 5.3.7 shows some level of

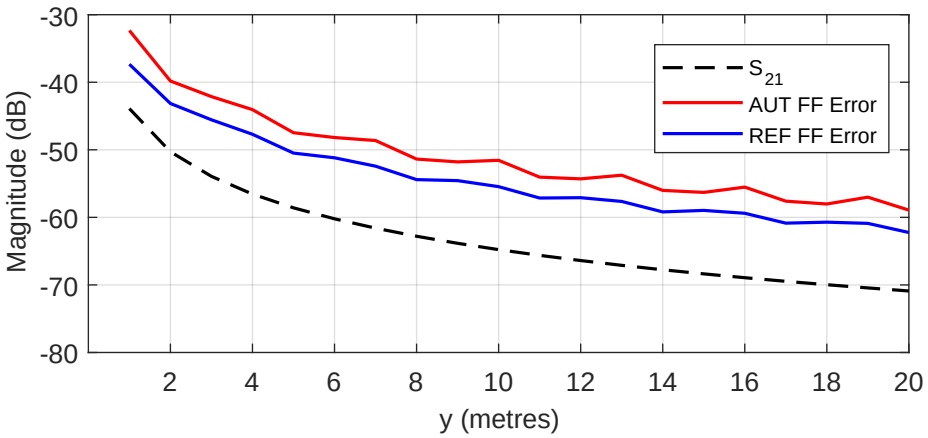


Figure 5.3.7: Comparing scalar far-field error $e_i$ with the magnitude of mutual coupling between the AUT and reference antenna $S_{21}$ for increasing distance between the two antennas

interaction between the antennas, even when placed as far as 20 m apart, the affect on the resulting far-field patterns is slight and almost imperceptible for $y_{ref} \geq 2$ m. Nonetheless, we find that performing a near-field measurement simulation with $z_0 = 3\lambda$ and $y_{ref} = 4$ m, still produces an unsatisfactory result in the $\phi = 90°$ plane, as shown in Fig. 5.3.8.

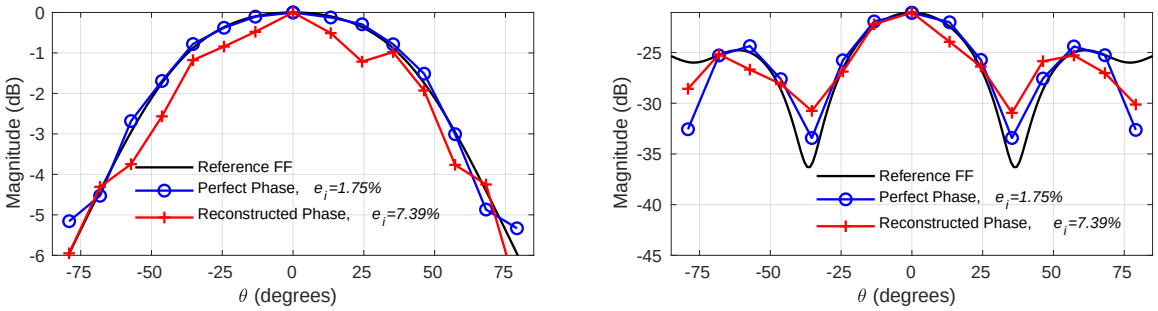


(a) Co-polarisation (b) Cross-polarisation

Figure 5.3.8: Transformed far-field pattern at $\phi = 90°$ with reconstructed phase using reference antenna at $y_{ref} = 4$ m and $z_0 = 3\lambda$

This leads us to consider the possibility that this coupling affect seen in the directly computed far-field may be more pronounced in the region closer to the antennas, where the near-field measurement is performed. In this light, we analyse the directly computed near-fields in the region around the AUT and reference. More specifically, given that our previous findings show that the predicted patterns at $\phi = 90°$ are most severely affected, we consider the near-field in the $yz$-plane between $-5 \leq y \leq 5$ metres and $1 \leq z \leq 6$ metres. Then, analogous to the procedure previously performed in the far-field, we excite the AUT in the presence of the reference antenna and compare the recorded near-field in the chosen plane to that computed when the AUT is isolated. Given a reciprocal system, this effect the reference antenna has on the transmitted field of the AUT also describes the effect seen when the AUT is receiving a signal from a source placed at the corresponding point in the field. Furthermore, given that the receiving properties of the reference antenna also affect our far-field prediction (in the phase extraction process), we repeat the experiment with the reference acting as a source, analysing the affect the AUT has on it's transmitted field. The error in the field seen here is then added to that found for the AUT, in order to give a total error level which is an indication as to the incurred error seen in the far-field pattern prediction. This is carried out with the reference antenna placed at $y_{ref} = 1$ m, where the magnitude and phase error is shown in Figs. 5.3.9a and 5.3.9b respectively. We see that the errors encountered are more severe the closer we are to the ground plane, where we see a phase error of over 10°, corresponding to a wavelength error of around $\lambda/30$. Furthermore, particularly in the phase plot, we see low error levels in the region where each antenna has a clear FoV, unobstructed by the presence of the other antenna.

It is now clear that both the distance $y_{ref}$ between the AUT and reference, together with the height $z_0$ of the chosen measurement plane, affect the phase extracted near-field measurement in question. In order to obtain adequate results, these variables should be

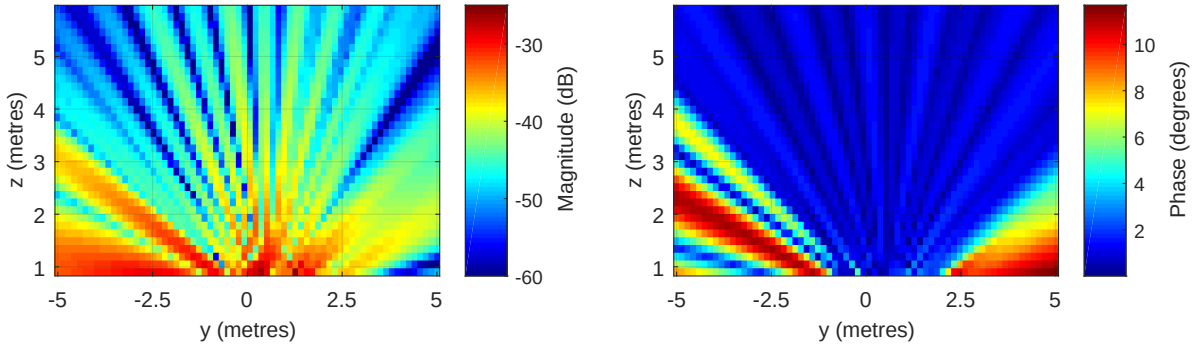


(a) Magnitude error (b) Phase error

Figure 5.3.9: Near-field error in the $yz$-plane, displaying difference between directly measured field with and without reference antenna placed at $y = 1$ m

chosen such that the measurement plane lies within in a region where each antenna has an unobstructed FoV. To find suitable choices for both, we repeat the above experiment 34 times, shifting the reference antenna by $\lambda/2$ along the $\hat{\mathbf{y}}$-axis from $y_{ref}1$ m to $y_{ref} = 6$ m. Then, for each measurement, we compute the average error seen along $-5 \leq y \leq 5$ m as a function of height $z$ above the antennas. These results are collated in order to produce the 2D plots shown in Fig. 5.3.10, which show the average error seen in the field as a function of height $z$ above the antennas and separation distance $y_{ref}$. These contour plots, which show decreasing levels of error for increasing $z$ and $y_{ref}$, can be used in order to find a suitable choice of measurement configuration. In so doing, one should keep in mind that these results are obtained from the fields as directly calculated in FEKO, whilst not considering probe effects, nor the phase extraction process itself. Thus, whilst the difference seen in the direct near-fields may be slight, any implicit error built into the measurement here will be compounded when extracting the far-field pattern of the AUT and may corrupt the results significantly.

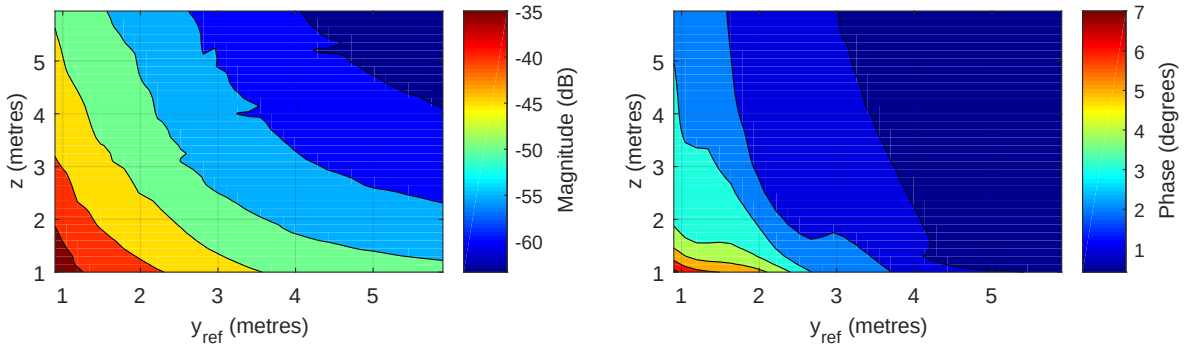


(a) Magnitude error (b) Phase error

Figure 5.3.10: Contour plots showing the average near-field error between $-5 \leq y \leq 5$ m as a function of increasing height $z$ above the AUT and position of reference antenna $y_{ref}$

Informed by the above investigation, we set up the measurement simulation with

$z_0 = 4$ m and $y_{ref} = 4$ m. The resulting far-field pattern predictions for different $\phi$-cuts are shown in Figs. 5.3.11–5.3.13. It can be seen that increasing the separation distance $y_{ref}$ between the AUT and reference antenna, as well as the height of the measurement plane $z_0$, serves to improve the results considerably. However, there is still a slight ripple affecting the $\phi = 90°$ plane prediction.

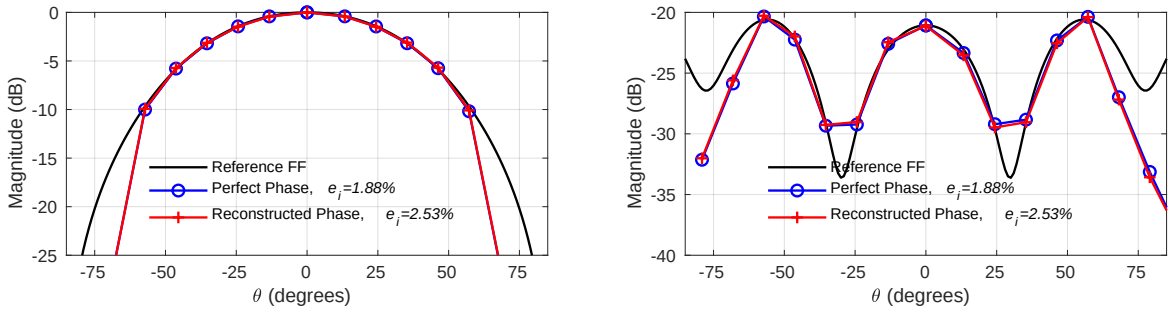


(a) Co-polarisation (b) Cross-polarisation

Figure 5.3.11: Transformed far-field pattern at $\phi = 0°$ with reconstructed phase using reference antenna at $y_{ref} = 4$ m and $z_0 = 4$ m

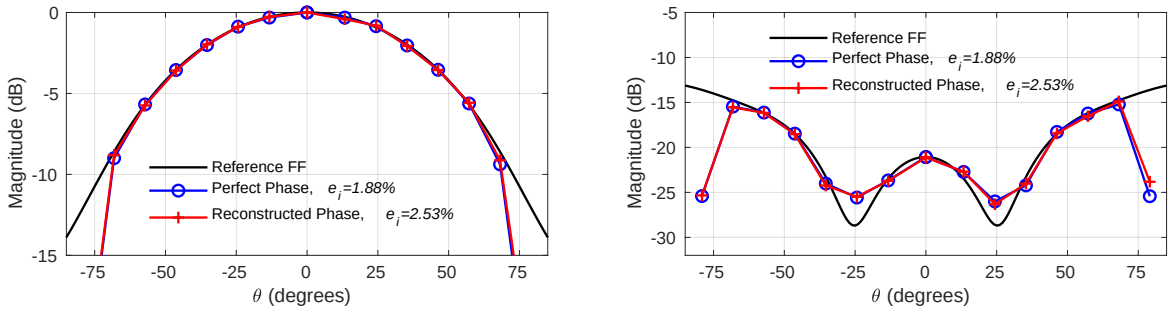


(a) Co-polarisation (b) Cross-polarisation

Figure 5.3.12: Transformed far-field pattern at $\phi = 45°$ with reconstructed phase using reference antenna at $y_{ref} = 4$ m and $z_0 = 4$ m

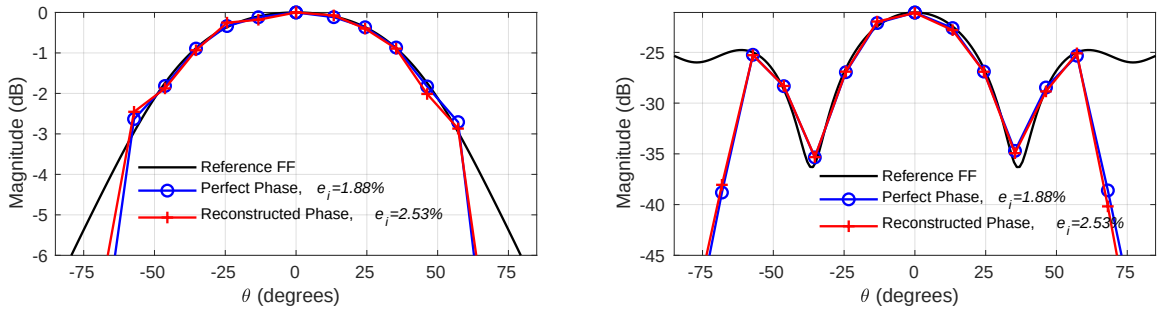


(a) Co-polarisation (b) Cross-polarisation

Figure 5.3.13: Transformed far-field pattern at $\phi = 90°$ with reconstructed phase using reference antenna at $y_{ref} = 4$ m and $z_0 = 4$ m

## 5.4 Practical Phase Extracted Measurement

We wish to proceed our investigation by performing a practical near-field antenna measurement which illustrates the techniques of probe correction and phase extraction performed in the simulations above. Considering the MFAA prototype element introduced in Section 3.2.1 as our AUT, we emulate the phase extraction problem in the anechoic chamber by exciting the probe with a voltage source which is generated independently from the instrument used to the response at the AUT. While the chamber provides a controlled environment and accurate probe positioning system, physical constraints limit the size of our scan plane which decreases the maximum angle $\theta_{max}$ over which the far-field pattern can be accurately predicted. Specifically, we are limited to the square scan plane with side lengths of 1.95 m, which is considerably smaller than the 10x10 metre scan plane considered in the simulation of the problem. With this relatively small scan plane, $\theta_{max}$ decreases considerably, even if we perform the measurement close to the antenna at $z_0 = 3\lambda$, where (2.3.50) gives $\theta_{max} \approx 42°$. In addition to decreasing the angle over which we can expect a valid far-field prediction, sampling this scan plane at a Nyquist spacing of $\lambda/2$, and attempting to solve for the equivalent currents over the AUT (with multipole order $L = 16$), results in a situation where the number of unknowns outweighs the total number of measurement samples. With this under-determined system, will affect the performance of FIAFTA to predict the far-field pattern, even within the valid region given by $\theta_{max}$. Furthermore, we are not able to place the reference antenna as far away from the AUT as was indicated necessary to reduce mutual coupling affects between the antennas. Before proceeding with any practical measurement, we briefly return to FEKO and simulate the problem considering our new set of limitations in order to gauge the effect they will have on our experiment. Choosing $y_{ref} = 1.085$ m and $z_0 = 3\lambda$ m (corresponding to a convenient configuration in the chamber), we simulate the near-field

measurement for the reduced 1.95x1.95 metre scan plane. The predicted far-field patterns resulting are shown for different $\phi$ cuts in Figs. 5.4.1–5.4.3. Together with the patterns which result from utilising our phase reconstruction method, we have also included results which assume this phase is perfectly extracted, i.e. we use the exact phase values which were assigned to the source voltage at the probe instead of using the reference antenna to determine this. The results show a noticeable level of corruption in the patterns predicted with the reconstructed phase, where again it is most severe at $\phi = 90°$. Even the patterns obtained considering a perfect phase extraction are seen to suffer from the close spacing between the AUT and reference antenna.

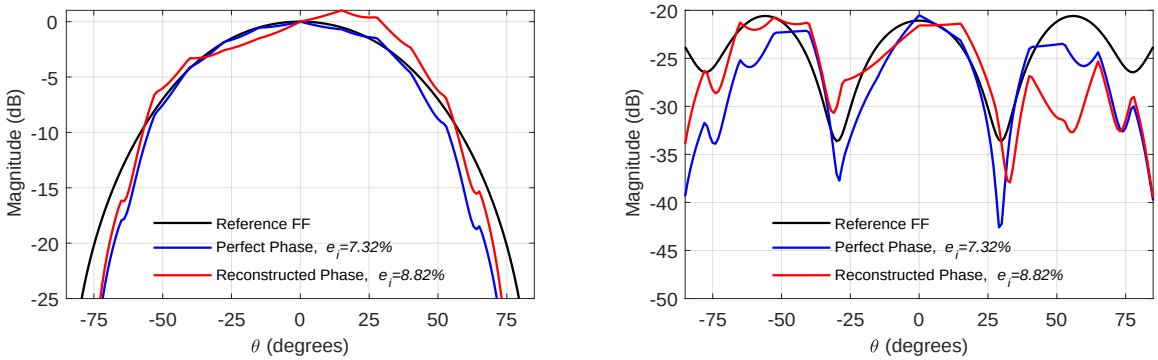


(a) Co-polarisation (b) Cross-polarisation

Figure 5.4.1: Transformed far-field pattern at $\phi = 0°$ for limited scan plane measurement simulation, taken at $z_0 = 3\lambda$ and reconstructed phase using reference antenna at $y_{ref} = 1$ m

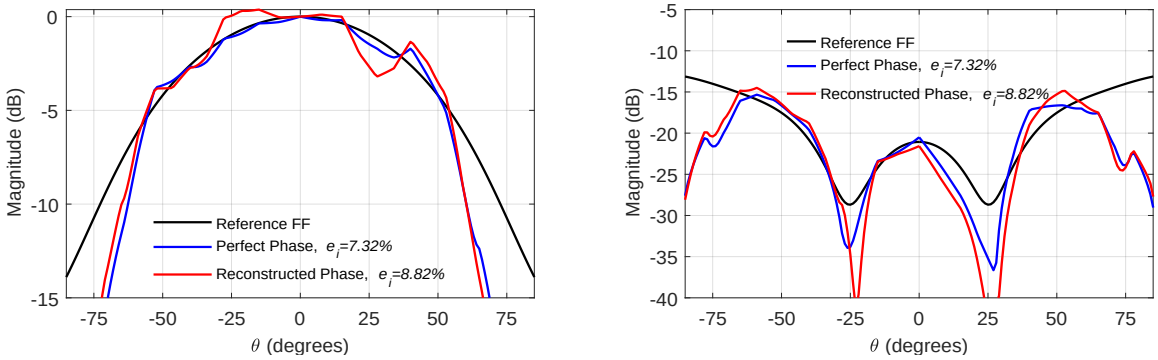


(a) Co-polarisation (b) Cross-polarisation

Figure 5.4.2: Transformed far-field pattern at $\phi = 45°$ for limited scan plane measurement simulation, taken at $z_0 = 3\lambda$ and reconstructed phase using reference antenna at $y_{ref} = 1$ m

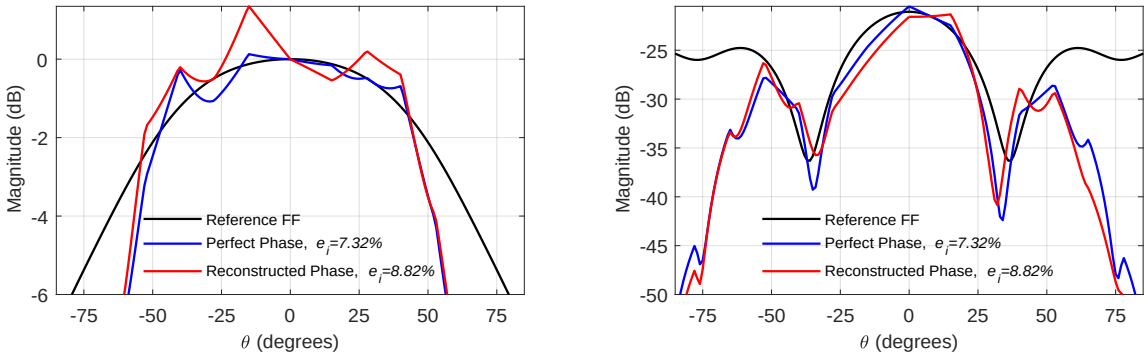


(a) Co-polarisation (b) Cross-polarisation

Figure 5.4.3: Transformed far-field pattern at $\phi = 90°$ for limited scan plane measurement simulation, taken at $z_0 = 3\lambda$ and reconstructed phase using reference antenna at $y_{ref} = 1$ m

We find that our simulation of the problem indicates that the given measurement configuration will produce rather unsatisfactory results. Nevertheless, with limited alternatives, we proceed with the practical measurement as is. At the very least, finding a level of corruption in the practical measurement akin to that found for the simulation, will corroborate some of our previous sentiments on phase extraction and serve to warrant further investigation into the subject. With the same probe antenna (RGP10) used in the spherical near-field measurement of Section 3.2.1, we proceed with the measurement in the configuration given above. We use a printed LPDA as our reference antenna, which possesses similar maximum dimensions and co-polarised beam pattern as the Yagi used in the simulation. Emulating the situation we would have for a UAV-based measurement, we use an AnaPico signal generator to excite the probe antenna with a 1 GHz source, whilst recording the response seen at the AUT and reference with a high-speed Tektronix MS06 oscilloscope. The measurement process involved recording the time domain responses seen at the AUT and reference antenna for each probe position in the scan plane. An example of these recorded signals for a single measurement point is shown in Fig. 5.4.4, where one can see a clear phase difference between the two waves. Subsequently, we take the FFT

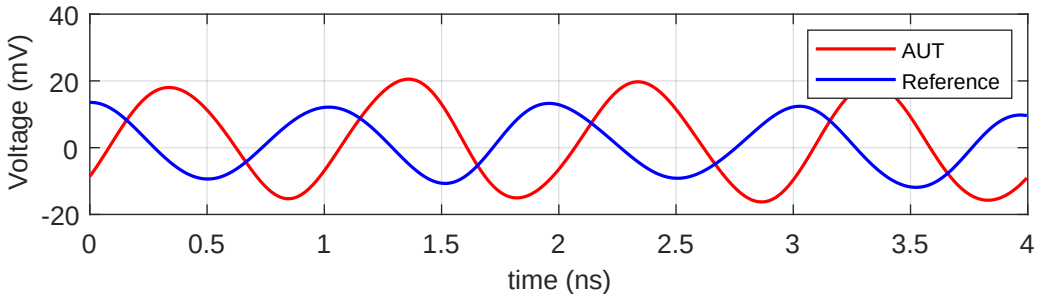


Figure 5.4.4: Time domain signals of recorded when probe is placed at a single point in the measurement plane

of each of these recorded time domain signals to get the response of each antenna over a 14×14 sample grid. This is performed for both co- and cross-polarisation by rotating the AUT by 90° about $\hat{\mathbf{z}}$, giving the two sets of responses for the AUT $U_1$ and $U_2$. The magnitude of these two responses is shown in Fig. 5.4.5, where $U_1$ corresponds to the polarisation of the probe aligned with $\hat{\mathbf{x}}$, and $U_2$ corresponds to alignment with $\hat{\mathbf{y}}$.

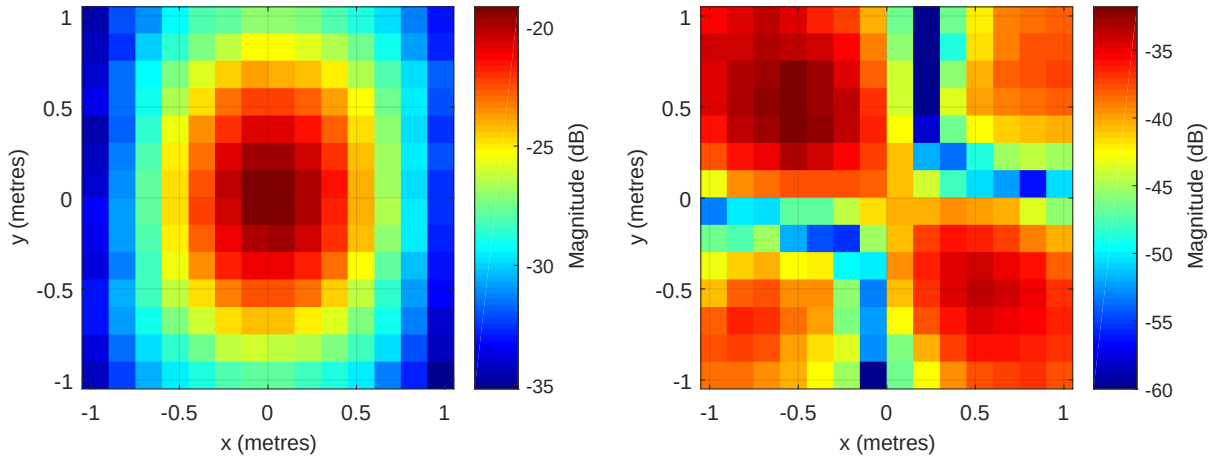


(a) $U_1$ (b) $U_2$

Figure 5.4.5: Magnitude of response measured on AUT for practical near-field measurement

We proceed to reconstruct the phase of the response by employing our reconstruction method, where the far-field pattern of the LPDA is given from a previous near-field measurement. Unfortunately, such measured data was not available for the RGP10 probe and we resorted to modelling this structure in FEKO in order to extract its far-field pattern at 1 GHz. As well as being used in the phase extraction process, this pattern is also required to correct for the directionality of the probe transmitting pattern during probe correction. The predicted far-field patterns from this phase reconstructed measurement are shown in Figs. 5.4.6–5.4.8 for different $\phi$-cuts in, where the reference pattern is that which we determined in Section 3.2.1 using a conventional near-field measurement. We include both the corrected and uncorrected pattern predictions, where, as in Section 5.2, we see that correcting for the directionality of the probe serves to increase the off-axis pattern values, making for a wider co-polarised beam in the predicted AUT patterns. We see a similar level of corruption in the patterns to that observed for the simulation of this configuration. Yet again we notice that the $\phi = 90°$ is the worst affected, where Fig. 5.4.8a shows how the predicted beam falls off sharply to the sides.

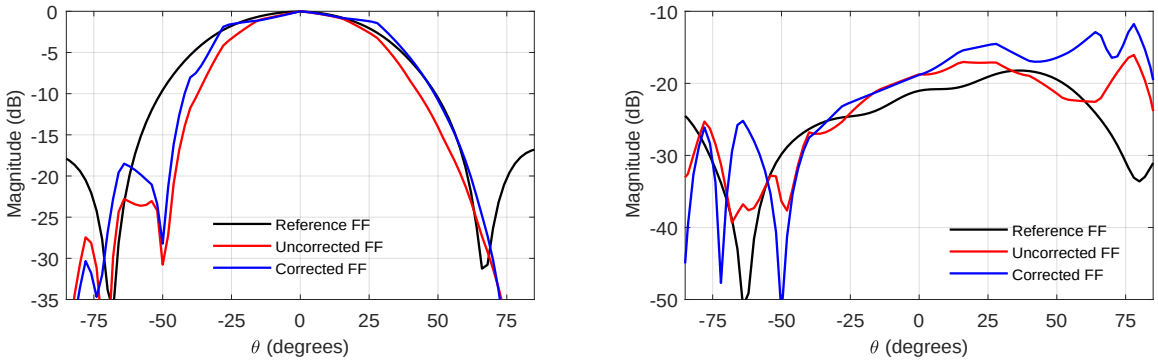


(a) Co-polarised (b) Cross-polarised

Figure 5.4.6: Predicted patterns at $\phi = 0°$ for practical, phase extracted measurement

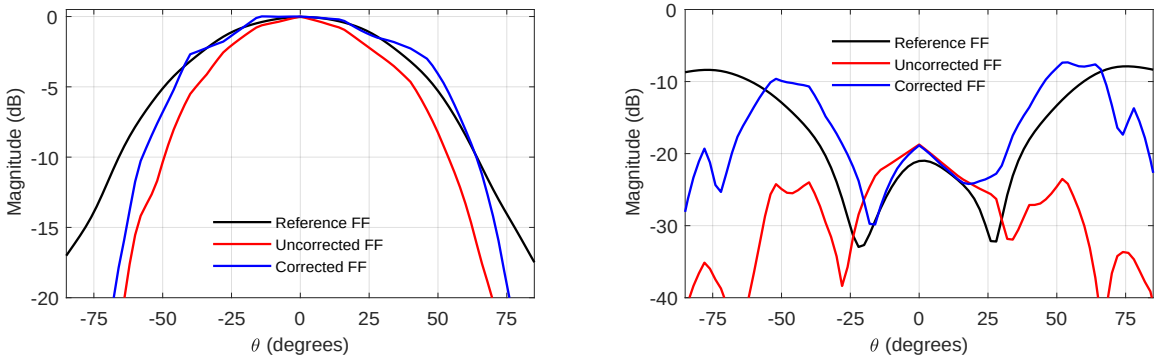


(a) Co-polarised (b) Cross-polarised

Figure 5.4.7: Predicted patterns at $\phi = 45°$ for practical, phase extracted measurement

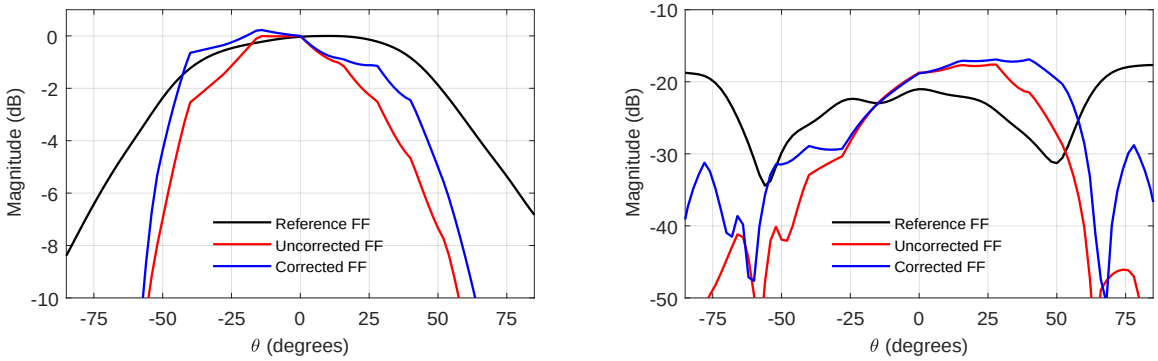


(a) Co-polarised (b) Cross-polarised

Figure 5.4.8: Predicted patterns at $\phi = 90°$ for practical, phase extracted measurement

Although these plots leave a lot to be desired in terms of accuracy, our phase reconstructed near-field measurement does at least capture the general shape of the far-field. This can be seen by considering the 3D pattern plots which result from this measurement

in Fig. 5.4.9, to those obtained for the conventional spherical near-field measurement performed in Section 3.2.1 and reprinted here for convenience in Fig.5.4.10. Whilst we cannot expect our planar measurement to be as accurate as the spherical measurement for large $\theta$ angles, we find that we are able to describe the main beam of the AUT reasonably well close to bore-sight.

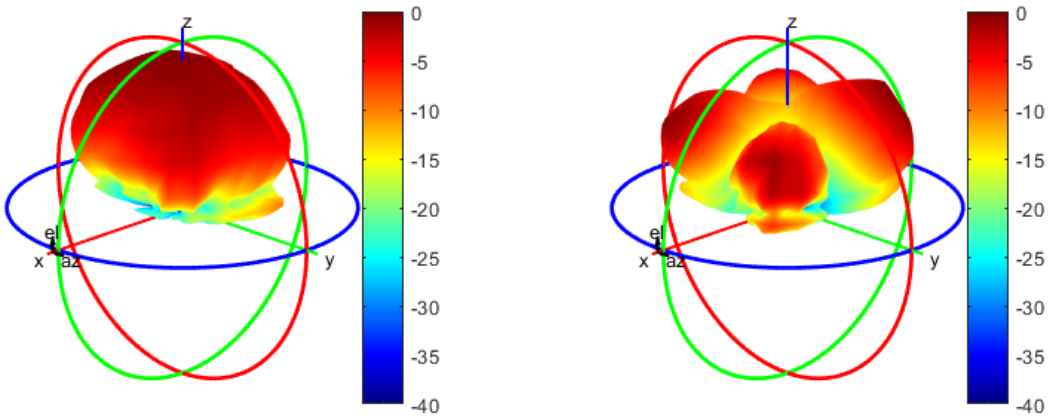


(a) Co-polarised (b) Cross-polarised

Figure 5.4.9: Predicted far-field patterns from practical phase extraction measurement of MFAA prototype element

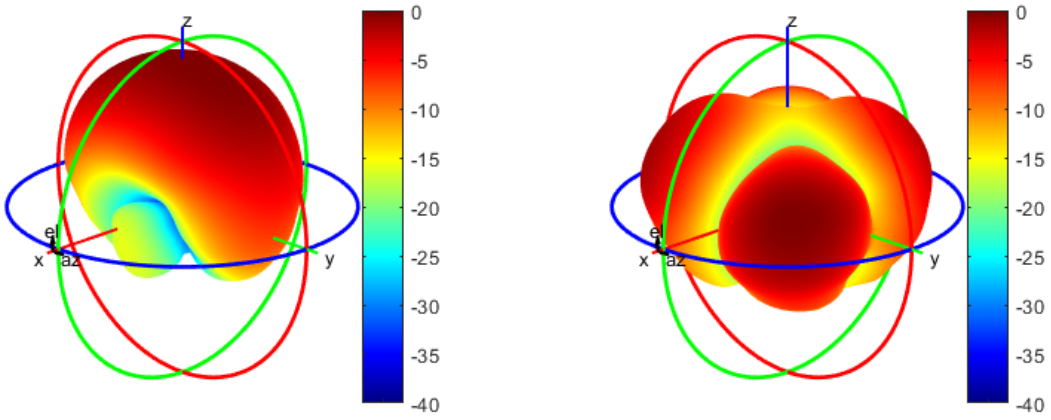


(a) Co-polarised (b) Cross-polarised

Figure 5.4.10: Reference far-field for MFAA antenna, computed from spherical near-field measurement in the anechoic chamber

# Chapter 6

# Conclusion

This dissertation presented a study into the viability of near-field antenna pattern measurements, performed utilising a UAV equipped with DGPS/RTK. With specific context to the MFAA, we sought to investigate two key concerns posed when considering measurements of this nature. Namely, the effect positional errors associated with DGPS/RTK will have on the prediction of far-field patterns and the issue of including phase in the near-field measurement.

To this end, we considered two near- to far-field transformation algorithms, the planar plane wave expansion (PPWE) and the fast irregular antenna field transformation algorithm (FIAFTA). The sensitivity of each algorithm to random probe positioning errors was analysed and compared in Chapter 4, where we found that the results produced by FIAFTA were far superior to those of the PPWE. Considering a 5 cm positional error, typically associated with DGPS/RTK, FIAFTA is seen to produce reasonable results up to around 200 MHz, whereas the PPWE is heavily corrupted as low as 50 MHz. For the band of interest 450–1450MHz, however, we find that both algorithms produce largely unsatisfactory results, bringing the viability of performing such measurements on the MFAA into question. Proceeding to analyse the effect of this 5 cm error on the MFAA prototype element, we found that FIAFTA was, in fact, able to produce reasonable results up to 1 GHz, although this required heavily oversampling the measurement plane. Other methods which may improve these results involve extending FIAFTA to include a priori knowledge of the AUT in order to restrict the solution space. Alternatively, the representation of equivalent sources in terms of spherical harmonics or mesh segments describing the actual AUT structure may present a more robust formulation of FIAFTA.

We then proceeded to investigate the process of extracting phase from the AUT response, when considering a randomly varying, unknown source phase. Here we utilised a reference antenna which was included in the measurement configuration and simultaneously recorded the response seen at both the AUT and reference. With the receiving characteristics of this reference antenna known, we were able to reconstruct the phase response of the near-field measurement. However, it was observed that mutual coupling between the AUT and reference antenna had a considerable effect on the predicted far-field patterns and one should consider the placement of these antennas very carefully. Moreover, we find that the separation distance between the antennas required to negate these effects is large enough to serve as a hindrance when attempting measurements within a confined space. This fact is demonstrated at the end of Chapter 5, where we attempt

the phase extracted near-field measurement in the anechoic chamber.

# Bibliography

[1] E. Colin-Beltran, A. J. Faulkner, and E. de Lera-Acedo, "Log-periodic sparse aperture array antennas dedicated to the MFAA instrument of the SKA telescope," in *2014 International Conference on Electromagnetics in Advanced Applications (ICEAA)*, Aug 2014, pp. 746–749.

[2] K. G. Jansky, "Electrical disturbances apparently of extraterrestrial origin," *Proceedings of the Institute of Radio Engineers*, vol. 21, no. 10, pp. 1387–1398, Oct 1933.

[3] P. Dewdney, P. Hall, R. Schillizzi, and J. Lazio, "The Square Kilometre Array," *Proceedings of the Institute of Electrical and Electronics Engineers IEEE*, vol. 97, no. 8, pp. 1482–1496, 2009.

[4] A. R. Taylor, "The Square Kilometre Array," in *Neutron Stars and Pulsars: Challenges and Opportunities after 80 years*, ser. IAU Symposium, J. van Leeuwen, Ed., vol. 291, Mar 2013, pp. 337–341.

[5] F. Aharonian, T. Arshakian, B. Allen, R. Banerjee, R. Beck, W. Becker, D. Bomans, B. Dieter, M. Brüggen, A. Brunthaler, B. Catinella, D. Champion, B. Ciardi, R. Crocker, M. A. de Avillez, R. Dettmar, D. Engels, T. Enßlin, H. Enke, and M. Zwaan, "Pathway to the Square Kilometre Array - The German White Paper," Jan 2013.

[6] South African Radio Observatory. [Online]. Available: https://www.ska.ac.za/

[7] Australia Telescope National Facility. [Online]. Available: https://www.atnf.csiro.au/projects/askap/

[8] Murchison Widefield Array. [Online]. Available: http://www.mwatelescope.org/

[9] ASTRON. [Online]. Available: http://www.lofar.org/

[10] M. A. Garrett, "Radio Astronomy Transformed: Aperture Arrays - Past, Present & Future," in *From Antikythera to the Square Kilometre Array: Lessons from the Ancients*, Jan 2012, p. 41.

[11] E. de Lera Acedo, A. J. Faulkner, and J. G. B. de Vaate, "SKA low frequency aperture array," in *2016 United States National Committee of URSI National Radio Science Meeting (USNC-URSI NRSM)*, Jan 2016, pp. 1–2.

[12] E. de Lera Acedo, B. Fiorelli, and M. Arts, "Polarization performance of log-periodic antennas on top of different types of ground plane; the SKA-low instrument case," in

*2015 9th European Conference on Antennas and Propagation (EuCAP)*, April 2015, pp. 1–4.

[13] Square Kilometre Array. [Online]. Available: https://www.skatelescope.org/

[14] W. A. van Cappellen, M. Santos, J. P. Macquart, F. Abdalla, E. Petroff, A. Siemion, R. Taylor, O. Smirnov, D. Davidson, J. Broderick, J. van Leeuwen, P. Woudt, M. A. Garrett, A. J. Faulkner, S. A. Torchinsky, I. M. van Bemmel, and J. Hessels, "MANTIS: The Mid-Frequency Aperture Array Transient and Intensity-Mapping System," *arXiv e-prints*, Dec 2016.

[15] Y. Zhang, A. El-Makadema, E. de Lera Acedo, P. Benthem, S. Barth, and A. Brown, "On the front-end design of mid-frequency aperture array for Square Kilometre Array," *Experimental Astronomy*, vol. 46, no. 2, pp. 357–380, 2018.

[16] J. Abraham, E. Colin-Beltran, E. de Lera Acedo, and A. J. Faulkner, "A 16-element LPDA random sparse prototype array for the SKA AA-mid instrument," in *2016 10th European Conference on Antennas and Propagation (EuCAP)*, April 2016, pp. 1–4.

[17] P. Benthem and G. W. Kant, "Embrace: Results from an aperture array for radio astronomy," in *2012 6th European Conference on Antennas and Propagation (EUCAP)*, March 2012, pp. 629–633.

[18] NRAO. [Online]. Available: https://science.nrao.edu/facilities/vla/

[19] T. Cornwell and E. B. Fomalont, "Self-Calibration," in *Synthesis Imaging in Radio Astronomy II*, ser. Astronomical Society of the Pacific Conference Series, G. B. Taylor, C. L. Carilli, and R. A. Perley, Eds., vol. 180, Jan 1999, p. 187.

[20] S. Van Der Tol, B. D. Jeffs, and A.-J. van der Veen, "Self-calibration for the LOFAR radio astronomical array," *IEEE Transactions on Signal Processing*, vol. 55, no. 9, pp. 4497–4510, 2007.

[21] S. J. Wijnholds, "Calibration of mid-frequency aperture array stations using self-holography," in *2017 International Conference on Electromagnetics in Advanced Applications (ICEAA)*, Sep. 2017, pp. 967–970.

[22] A. T. Sutinjo, T. M. Colegate, R. B. Wayth, P. J. Hall, E. de Lera Acedo, T. Booler, A. J. Faulkner, L. Feng, N. Hurley-Walker, B. Juswardy, S. K. Padhi, N. Razavi-Ghods, M. Sokolowski, S. J. Tingay, and J. G. Bij de Vaate, "Characterization of a low-frequency radio astronomy prototype array in Western Australia," *IEEE Transactions on Antennas and Propagation*, vol. 63, no. 12, pp. 5433–5442, Dec 2015.

[23] C. A. Balanis, *Advanced engineering electromagnetics*. John Wiley & Sons, 1999.

[24] "IEEE Standard for Definitions of Terms for Antennas," *IEEE Std 145-2013 (Revision of IEEE Std 145-1993)*, pp. 1–50, March 2014.

[25] C. A. Balanis, *Antenna theory: analysis and design*. John wiley & sons, 2016.

[26] T. Fritzel, H. Steiner, and R. Strauß, "Laser tracker metrology for uav-based antenna measurements," in *2018 IEEE Conference on Antenna Measurements Applications (CAMA)*, Sep. 2018, pp. 1–3.

[27] G. Virone, A. M. Lingua, M. Piras, A. Cina, F. Perini, J. Monari, F. Paonessa, O. A. Peverini, G. Addamo, and R. Tascone, "Antenna pattern verification system based on a micro unmanned aerial vehicle (UAV)," *IEEE Antennas Wireless Propag. Lett.*, vol. 13, pp. 169–172, 2014.

[28] P. Bolli, S. J. Wijnholds, E. de Lera Acedo, A. Lingua, J. Monari, F. Paonessa, G. Pupillo, and G. Virone, "In-situ characterization of international low-frequency aperture arrays by means of an UAV-based system," in *2017 XXXIInd General Assembly and Scientific Symposium of the International Union of Radio Science (URSI GASS)*, Aug 2017, pp. 1–4.

[29] C. Raucy, E. de Lera Acedo, N. Razavi-Ghods, D. González-Ovejero, and C. Craeye, "Low-cost near field pattern measurement technique for aperture array characterization," in *2013 7th European Conference on Antennas and Propagation (EuCAP)*, April 2013, pp. 661–665.

[30] T. Fritzel, R. Strauß, H. Steiner, C. Eisner, and T. Eibert, "Introduction into an UAV-based near-field system for in-situ and large-scale antenna measurements (Invited paper)," in *2016 IEEE Conference on Antenna Measurements Applications (CAMA)*, Oct 2016, pp. 1–3.

[31] P.-S. Kildal, *Foundations of antenna engineering: a unified approach for line-of-sight and multipath*. Artech House, 2015.

[32] A. Ludwig, "The definition of cross polarization," *IEEE Transactions on Antennas and Propagation*, vol. 21, no. 1, pp. 116–119, January 1973.

[33] H. T. Friis, "A note on a simple transmission formula," *Proceedings of the IRE*, vol. 34, no. 5, pp. 254–256, May 1946.

[34] A. Yaghjian, "An overview of near-field antenna measurements," *IEEE Transactions on Antennas and Propagation*, vol. 34, no. 1, pp. 30–45, January 1986.

[35] D. M. Kerns, "Correction of near-field antenna measurements made with an arbitrary but known measuring antenna," *Electronics Letters*, vol. 6, no. 11, pp. 346–347, May 1970.

[36] D. M. Kerns, "Plane-wave scattering-matrix theory of antennas and antenna-antenna interactions," *NASA STI/Recon Technical Report N*, vol. 82, 1981.

[37] J. Hansen, I. of Electrical Engineers, J. Hald, and F. Jensen, *Spherical Near-field Antenna Measurements*, ser. Electromagnetics and Radar Series. P. Peregrinus, 1988.

[38] R. F. Harrington, *Field computation by moment methods*. Wiley-IEEE Press, 1993.

[39] T. K. Sarkar and A. Taaghol, "Near-field to near/far-field transformation for arbitrary near-field geometry utilizing an equivalent electric current and MoM," *IEEE Transactions on Antennas and Propagation*, vol. 47, no. 3, pp. 566–573, March 1999.

[40] Y. Alvarez, F. Las-Heras, and M. R. Pino, "Reconstruction of equivalent currents distribution over arbitrary three-dimensional surfaces based on integral equation algorithms," *IEEE Transactions on Antennas and Propagation*, vol. 55, no. 12, pp. 3460–3468, Dec 2007.

[41] T. F. Eibert, E. Kilic, C. Lopez, R. A. Mauermayer, O. Neitz, and G. Schnattinger, "Electromagnetic field transformations for measurements and simulations," *Progress In Electromagnetics Research*, vol. 151, pp. 127–150, 2015.

[42] D. Paris, W. Leach, and E. Joy, "Basic theory of probe-compensated near-field measurements," *IEEE Transactions on Antennas and Propagation*, vol. 26, no. 3, pp. 373–379, May 1978.

[43] D. M. Pozar, *Microwave engineering*. John Wiley & Sons, 2009.

[44] D. M. Kerns, "Plane-wave scattering-matrix theory of antennas and antenna-antenna interactions-formulation and applications," *Journal of Research Section B Mathematical Sciences B*, vol. 80, pp. 5–51, 1976.

[45] Feng-Cheng Chang, "Novel coordinate transformations for antenna applications," *IEEE Transactions on Antennas and Propagation*, vol. 32, no. 12, pp. 1292–1297, December 1984.

[46] S. Gregson, J. McCormick, and C. Parini, *Principles of planar near-field antenna measurements*. IET, 2007, vol. 53.

[47] C. H. Schmidt, M. M. Leibfritz, and T. F. Eibert, "Fully probe-corrected near-field far-field transformation employing plane wave expansion and diagonal translation operators," *IEEE Transactions on Antennas and Propagation*, vol. 56, no. 3, pp. 737–746, 2008.

[48] M. A. Qureshi, "Near-field error analysis and efficient sampling techniques for the fast irregular antenna field transformation algorithm," Ph.D. dissertation, Technische Universität München, 2013.

[49] R. Coifman, V. Rokhlin, and S. Wandzura, "The fast multipole method for the wave equation: A pedestrian prescription," *IEEE Antennas and Propagation Magazine*, vol. 35, no. 3, pp. 7–12, 1993.

[50] G. B. Arfken and H. J. Weber, "Mathematical methods for physicists," 1999.

[51] D. Francesco, F. Ferrara, C. Gennarelli, R. Guerriero, and M. Migliozzi, "An effective NF-FF transformation technique with planar spiral scanning tailored for quasi-planar antennas," *Antennas and Propagation, IEEE Transactions on*, vol. 56, pp. 2981 – 2987, Oct 2008.

[52] O. M. Bucci, C. Gennarelli, and C. Savarese, "Representation of electromagnetic fields over arbitrary surfaces by a finite and nonredundant number of samples," *IEEE Transactions on Antennas and Propagation*, vol. 46, no. 3, pp. 351–359, March 1998.

[53] H. Pienaar, Private Communication, Stellenbosch, South Africa, 2018.

[54] ——, "Karoo array telescope site shielding: Laboratory, computational and multi-copter studies," Ph.D. dissertation, Stellenbosch: Stellenbosch University, 2015.

[55] Hex Technology, "Pixhawk v2 feature overview." [Online]. Available: http://www.hex.aero/

[56] ArduPilot. [Online]. Available: http://ardupilot.org/

[57] Hex Technology, "Here v2 user manual." [Online]. Available: http://www.hex.aero/

[58] U-blox, "NEO-M8P." [Online]. Available: https://www.u-blox.com/

[59] A. D. Yaghjian, *Upper-bound errors in far-field antenna parameters determined from planar near-field measurements: part I: analysis*. US Dept. of Commerce, National Bureau of Standards, 1975, vol. 667.

[60] A. C. Newell, "Error analysis techniques for planar near-field measurements," *IEEE Transactions on Antennas and Propagation*, vol. 36, no. 6, pp. 754–768, 1988.

[61] H. Pienaar and D. Davidson, "Error sensitivity analysis for multi-copter planar positioning on low-gain nearfield measurements," in *2016 International Conference on Electromagnetics in Advanced Applications (ICEAA)*. IEEE, 2016, pp. 568–571.

[62] M. A. Qureshi, C. H. Schmidt, and T. F. Eibert, "Near-field error analysis for arbitrary scanning grids using fast irregular antenna field transformation algorithm," *Progress In Electromagnetics Research*, vol. 48, pp. 197–220, 2013.

[63] S. G. H. Kriel and D. I. L. de Villiers, "Probe positioning error sensitivity analysis for planar near-field antenna measurements," in *2019 URSI Asia-Pacific Radio Science Conference (AP-RASC)*, March 2019, pp. 1–4.

[64] Altair Engineering Inc., "Altair FEKO 2017.2," Stellenbosch, South Africa, 2017. [Online]. Available: https://altairhyperworks.com/product/FEKO

[65] G. Schnattinger, C. Lopez, E. Kılıç, and T. Eibert, "Fast near-field far-field transformation for phaseless and irregular antenna measurement data," *Advances in Radio Science*, vol. 12, pp. 171–177, Nov 2014.

[66] A. Paulus, J. Knapp, and T. F. Eibert, "Phaseless near-field far-field transformation utilizing combinations of probe signals," *IEEE Transactions on Antennas and Propagation*, vol. 65, no. 10, pp. 5492–5502, Oct 2017.

[67] J. Hallas, *Basic Antennas: Understanding Practical Antennas and Design*. The National Association for Amateur Radio, Newington USA, 2008.